The Dissertation Committee for Roque Julio Hernandez
certifies that this is the approved version of the following dissertation:

Hybrid Particle-Element Method for a General Hexahedral Mesh

Committee:

_____
Eric P. Fahrenthold, Supervisor

_____
Jeffrey K. Bennighof

_____
Michael D. Bryant

_____
Richard H. Crawford

_____
Raul G. Longoria

Hybrid Particle-Element Method for a General Hexahedral Mesh

by

Roque Julio Hernandez, B.S.;M.S.

DISSERTATION

Presented to the Faculty of the Graduate School of

The University of Texas at Austin

in Partial Fulfillment

of the Requirements

for the Degree of

DOCTOR OF PHILOSOPHY

THE UNIVERSITY OF TEXAS AT AUSTIN

August 2009

Dedicated to God

and to my Family

Acknowledgments

First of all, I thank God for given me the strength to walk in this journey. I express my most sincere gratitude to my advisor, Dr. Eric P. Fahrenthold, his guidance, patience, understanding and encouragement throughout this work have been tremendous. I also thank the members of my committee, Dr. Jeffrey K. Bennighof, Dr. Michael D. Bryant, Dr. Richard H. Crawford and Dr. Raul G. Longoria.

For their support I thank the Universidad del Norte and the Fulbright-DNP-COLCIENCIAS program. I thank the Texas Advanced Computing Center at the University of Texas at Austin for computer time support. This work was supported in part by NASA Johnson Space Center.

I have been fortunate to have such good friends who made this time better. My deepest thanks to Jacinto Lopez Toledo for all his help, patience, and friendship. Also I thank Leonardo and Patricia, they have been like a family to me here in Austin. I would like to express my gratitude to Bernardo Lopez, he has been a true friend. For his help I thank Kwon Joong Son.

I wish to thank all the people who supported me throughout these years.

Finally, I thank Maria Mei Amat for her incredible love, support and understanding. She is a real God's gift to me; I cannot find words to express

how important she is to my life.

Hybrid Particle-Element Method for a General Hexahedral Mesh

Publication No. _____

Roque Julio Hernandez, Ph.D.
The University of Texas at Austin, 2009

Supervisor: Eric P. Fahrenthold

The development of improved numerical methods for computer simulation of high velocity impact dynamics is of importance in a variety of science and engineering fields. The growth of computing capabilities has created a demand for improved parallel algorithms for high velocity impact modeling. In addition, there are selected impact applications where experimentation is very costly, or even impossible (e.g. when certain bioimpact or space debris problems are of interest). This dissertation extends significantly the class of problems where particle-element based impact simulation techniques may be effectively applied in engineering design.

This dissertation develops a hybrid particle-finite element method for a general hexahedral mesh. This work included the formulation of a numerical algorithm for the generation of an ellisoidal particle set for an unstructured

hex mesh, and a new interpolation kernel for the density. The discrete model is constructed using thermomechanical Lagrange equations. The formulation is validated via simulation of published impact experiments.

Table of Contents

List of Tables

List of Figures

xiv

Chapter 1

Introduction

1.1 Background and motivation

Simulation of high velocity impact dynamics calls for numerical methods capable of modeling a wide array of physical effects, including general contact-impact, strong shocks, adiabatic heating, large strain elastic-plastic deformation, fragmentation, and melting. Three numerical methods are currently in general use for this class of problems, they are Eulerian finite volume methods [45], Lagrangian finite element methods [28], and smooth particle hydrodynamics (SPH) methods [61]. Each method has advantages and disadvantages. Eulerian hydrocodes model general contact-impact, but difficulties with interface tracking algorithms can lead to numerical diffusion and inaccurate modeling of strength effects. As a result they are best suited to extremely high velocity impact applications where phase changes and multi-material thermodynamics are important. Lagrangian finite element codes offer very accurate models of material strength effects. However they are affected by mesh distortion problems and incorporate slideline based contact-impact algorithms, which require an explicit adaptive description of all contact-impact surfaces. SPH methods model general contact-impact, but they exhibit numerical fracture and suffer from tensile instabilities. As a result they are not well suited

to applications where material strength effects are important.

Recent efforts to combine the advantages of particle and finite element methods have led to the development of both coupled particle-element [35, 36] and hybrid particle-element [33, 50, 56] methods. The coupled particle-element methods employ particles to represent part of the interacting material and finite elements to represent the remaining material. An advantage of this technique, of particular relevance in the present context, is that material blocks represented by the finite elements can have a complex geometry. Disadvantages are that the aforementioned limitations of pure particle and pure finite element methods may not be entirely eliminated, and that additional particle-to-element contact-impact algorithms and/or particle-to-element mapping algorithms must be introduced. The result can be a numerical method very difficult to parallelize.

The hybrid particle-element technique described by Shivarama and Fahrenthold [56], Park and Fahrenthold [50], and Horban and Fahrenthold [33] employs particles and elements in tandem, to represent all interacting materials. It provides a true Lagrangian description of all material strength effects, including large strain elastic-plastic deformation and fracture. It incorporates a general description of all contact-impact effects, without the introduction of slidelines or interface tracking algorithms. However to date the method has been limited to simple projectile and target geometries.

1.2 Objectives and methodology

This dissertation generalizes the hybrid particle-finite element method described in previous work [33, 50, 56]. It develops a numerical method suitable for high velocity impact simulation in applications involving complex structural geometries. Specifically, the improved method models high velocity impact dynamics for projectiles and targets described by a general hexahedral mesh. This objective is accomplished for gradual transitions in hex element dimensions and for limited hex aspect ratios, restrictions which do allow the modeling of complex parts and structures. This chapter outlines the major subtasks accomplished in this research.

1.2.1 Translation and model generation

The first task is translation of a general hex input mesh, produced for example by commercial mesh generation software, into a particle-element model. Previous work employs a body centered cubic packing scheme. To reduce the overall particle count (in the interest of computational efficiency) and to avoid the possibility of poorly shaped tetrahedral subelements (previously employed in tension calculations) the improved method introduces particles only at the hex vertices. The translation algorithm specifies particle masses, particle aspect ratios, and particle Euler parameters based on the element geometry. Although the use of ellipsoidal particles complicates considerably the translation algorithm, accurate representation of a general hex mesh using a spherical particle set (used by all alternative particle-based impact simulation

3

methods) would appear to be quite difficult.

1.2.2 Density and rate of dilatation interpolations

The second task is the development of interpolation kernels for both the density and the rate of dilatation, suitable for application under the nonuniform particle mass, particle spacing, and particle orientation distributions which characterize a general hex mesh. Tests on one dimensional shock problems have indicated that good solutions can be obtained using inconsistent interpolations of the density and rate of dilatation. A long range interpolation of the density is desirable for smooth variations in the field properties, while a short range interpolation of the rate of dilatation is desirable to reflect the correct contact-impact physics, that is to allow for only near neighbor interaction. Normalization of the interaction distances specified in the kernel functions is required, to account for nonuniform particle spacing. The normalization is based on particle separation distances in the reference configuration for the hex mesh. In addition, an appropriate and particle-specific definition of what constitutes a full neighbor set is established. It is also computed in the reference configuration.

1.2.3 Thermomechanical Lagrange equations

The stored energy functions, constraint equations, and virtual work expressions for the system are combined with the canonical Lagrange equations, to obtain an ODE model for the particle-element system. The formulation in

the current work involves a synthesis of holonomic and nonholonomic formulations applied separately in previous work [33, 50, 56]. Degenerate Lagrange equations for the particle internal energies and the damage and plastic variables make it possible to determine in closed form the Lagrange multipliers associated with the nonholonomic constraints. This process defines the generalized nonconservative forces in the canonical Lagrange equations and thereby leads to an explicit state space model for the thermomechanical system. The developed formulation has been validated via simulations of published three dimensional impact experiments.

1.3   Summary

The development of improved numerical methods for computer simulation of high velocity impact dynamics is of importance in a variety of science and engineering fields. The growth of computing capabilities has created a demand for improved parallel algorithms for high velocity impact modeling. In addition, there are selected impact applications where experimentation is very costly, or even impossible (e.g. when certain bioimpact or space debris problems are of interest). This dissertation extends significantly the class of problems where particle-element based impact simulation techniques may be effectively applied in engineering design.

Chapter 2

Kinematics and Interpolation

2.1 Introduction

This chapter describes the kinematics of the particles and elements used to formulate the hybrid numerical model, and an algorithm which defines the ellipsoidal particle set used to represent a general hexahedral mesh.

2.2 Particle Kinematics

The position and orientation of the particles $i = 1, ..., n$ are defined by a center of mass position vector and an Euler parameter vector for each particle

$$\mathbf{c}^{(i)} = [\, c_1^{(i)} \; c_2^{(i)} \; c_3^{(i)} \,]^T, \qquad \mathbf{e}^{(i)} = [\, e_0^{(i)} \; e_1^{(i)} \; e_2^{(i)} \; e_3^{(i)} \,]^T \tag{2.1}$$

where a superscript T denotes the transpose, and n is the number of particles.

A general rotation of a body with one point fixed can be expressed as a single rotation about an axis through that point [2], and the Euler parameters could be used to describe this rotation as is shown in Figure 2.1. The Euler Parameters define a rotation matrix for the particle

$$\mathbf{R}^{(i)} = \mathbf{A}^{(i)} \, \mathbf{G}^{(i)T} \tag{2.2}$$

where

$$\mathbf{A}^{(i)} = \begin{bmatrix} -e_1^{(i)} & e_0^{(i)} & -e_3^{(i)} & e_2^{(i)} \\ -e_2^{(i)} & e_3^{(i)} & e_0^{(i)} & -e_1^{(i)} \\ -e_3^{(i)} & -e_2^{(i)} & e_1^{(i)} & e_0^{(i)} \end{bmatrix} \tag{2.3}$$

and

$$\mathbf{G}^{(i)} = \begin{bmatrix} -e_1^{(i)} & e_0^{(i)} & e_3^{(i)} & -e_2^{(i)} \\ -e_2^{(i)} & -e_3^{(i)} & e_0^{(i)} & e_1^{(i)} \\ -e_3^{(i)} & e_2^{(i)} & -e_1^{(i)} & e_0^{(i)} \end{bmatrix} \tag{2.4}$$

The rotation matrix relates Cartesian coordinates defined in fixed and corotating systems

$$\mathbf{v} = \mathbf{R}^{(i)}\,\hat{\mathbf{v}} \tag{2.5}$$

where $\mathbf{v}$ is a vector defined in a fixed system and $\hat{\mathbf{v}}$ is the same vector defined in a corotating system.

The time derivatives of the Euler parameters are related to the body-fixed angular velocity components by

$$\dot{\mathbf{e}}^{(i)} = \frac{1}{2}\,\mathbf{G}^{(i)T}\,\boldsymbol{\omega}^{(i)} \tag{2.6}$$

The Euler parameters and their time derivatives define the antisymmetric matrix $\boldsymbol{\Omega}^{(i)}$ whose axial vector is the particle angular velocity using

$$\boldsymbol{\Omega}^{(i)}\mathbf{v} = \boldsymbol{\omega}^{(i)} \times \mathbf{v} \tag{2.7}$$

This antisymmetric matrix $\boldsymbol{\Omega}^{(i)}$ is related to the Euler parameters and their time derivatives by the equations

$$\boldsymbol{\Omega}^{(i)} = 2\,\mathbf{G}^{(i)}\,\dot{\mathbf{G}}^{(i)T} = -2\,\dot{\mathbf{G}}^{(i)}\mathbf{G}^{(i)T} = \mathbf{R}^{(i)T}\,\dot{\mathbf{R}}^{(i)} \tag{2.8}$$

7

2.3 Density interpolation

The hybrid particle-element formulations described in previous work employ a density interpolation suitable for use on a structured hexahedral mesh. This work introduces a new density interpolation, suitable for use on a general hexahedral mesh. The density interpolation is expressed as a function of the ellipsoidal coordinate

$$\zeta^{(i,j)} = \left[\left(\mathbf{c}^{(i)} - \mathbf{c}^{(j)} \right)^T \hat{\mathbf{H}}^{(j)} \left(\mathbf{c}^{(i)} - \mathbf{c}^{(j)} \right) \right]^{\frac{1}{2}} \tag{2.9}$$

where $|\mathbf{c}^{(i)} - \mathbf{c}^{(j)}|$ is the separation distance of the mass centers of particles i and j, and

$$\hat{\mathbf{H}}^{(j)} = \mathbf{R}^{(j)} \mathbf{H}^{(j)} \mathbf{R}^{(j)T} \tag{2.10}$$

with

$$\mathbf{H}^{(j)} = \begin{bmatrix} 2\beta h_1^{(j)} & 0 & 0 \\ 0 & 2\beta h_2^{(j)} & 0 \\ 0 & 0 & 2\beta h_3^{(j)} \end{bmatrix}^{-2} \tag{2.11}$$

which is a function of the jth particle semi-major axes (indicated by $h_k{}^{(j)}$), and the positive parameter β allows for close packing of particles at the reference density. The exponent in equation 2.11 represents in a compact form the square of the corrected semi-major axes in the denominator of the ellipsoidal coordinate. Figure 2.2 shows the effect of β for a structured mesh (cubic elements with side length L = 2). Assuming spherical particles the radius is 1.241, which means that overlapping occurs among particles. To avoid this overlapping β is computed as 0.806 and the radius is scaled using β (it is now 1) so the particles just touch each other.

The density interpolation is

$$\frac{\rho^{(i)}}{\rho_o^{(i)}} = 1 \ + \ \frac{1}{N^{(i)}} \sum_{j=1}^{n} \left[\left(\frac{\zeta^{R(i,j)}}{\zeta^{(i,j)}} \right)^3 - 1 \right] W^{(i,j)} \tag{2.12}$$

where

$$W^{(i,j)} = \begin{cases} 0 & \text{if } i = j \\ 0 & \text{if } i \neq j \text{ and } \zeta^{(i,j)} \geq 1 \\ 1 & \text{if } i \neq j \text{ and } \zeta^{(i,j)} < 1 \end{cases}$$

$$W^{(i,j)} = (1 - \delta_{ij}) \, \hat{u} \left(1 - \zeta^{(i,j)} \right) \tag{2.13}$$

with δ_{ij} the Kronecker delta and $\hat{u}$ the unit step function.

The density in the current configuration is $\rho^{(i)}$, and the density in the reference configuration is $\rho_o^{(i)}$. The term $\zeta^{R(i,j)}$ in the numerator of equation 2.12 is an ellipsoidal coordinate for the neighbor particle in the reference configuration. This parameter, set to a maximum value of one, normalizes the interpolation and thereby allows for the density to be computed on a general hexahedral mesh. The neighbor set count is represented by $N^{(i)}$, and takes the value of 26 for a structured mesh. In general, this number is computed for each particle, in the reference configuration, at the start of a simulation.

To illustrate how this density interpolation works, suppose we have a cube that experiences a uniform compression in such a way that the length of each side in the current configuration is 1/2 of the length of each side in the reference configuration. The density has to increase, and is 8 times the reference density as we can see in Figure 2.3. Now, in the case of a uniform compression in a general hexahedral mesh the particles move in, as is shown in figure 2.4; under this uniform compression we can compute the density

in the current configuration, which is 8 times the density in the reference configuration as illustrated in Figure 2.5.

It is also important to note the orientation effect of the particles, as can be see it in Figures 2.6 and 2.7; the number of interacting particles changes with orientation.

In the case of a consistent interpolation of the density and rate of dilatation, differentiation of the density interpolation yields

$$\frac{\dot{\rho}^{(i)}}{\rho_o{}^{(i)}} = -\frac{3}{N^{(i)}} \sum_{j=1}^{n} \frac{\zeta^{R(i,j)3}}{\zeta^{(i,j)3}} \frac{\dot{\zeta}^{(i,j)}}{\zeta^{(i,j)}} W^{(i,j)} \tag{2.14}$$

where

$$\dot{\zeta}^{(i,j)} = \frac{1}{\zeta^{(i,j)}} \left[\left(\hat{\mathbf{H}}^{(j)} \mathbf{r}^{(i,j)} \right)^T \dot{\mathbf{r}}^{(i,j)} + 2 \left(\mathbf{H}^{(j)} \hat{\mathbf{r}}^{(i,j)} \times \hat{\mathbf{r}}^{(i,j)} \right)^T \mathbf{G}^{(j)} \dot{\mathbf{e}}^{(j)} \right] \tag{2.15}$$

and

$$\mathbf{r}^{(i,j)} = \mathbf{c}^{(i)} - \mathbf{c}^{(j)}, \qquad \hat{\mathbf{r}}^{(i,j)} = \mathbf{R}^{(j)T} \mathbf{r}^{(i,j)} \tag{2.16}$$

Combining these results

$$\dot{\rho}^{(i)} = -\frac{3}{N^{(i)}} \sum_{j=1}^{n} \rho_o{}^{(i)} \frac{\zeta^{R(i,j)3} W^{(i,j)}}{\zeta^{(i,j)5}} \left[\left(\hat{\mathbf{H}}^{(j)} \mathbf{r}^{(i,j)} \right)^T \dot{\mathbf{r}}^{(i,j)} \right.$$
$$\left. + \left(\mathbf{H}^{(j)} \hat{\mathbf{r}}^{(i,j)} \times \hat{\mathbf{r}}^{(i,j)} \right)^T \mathbf{G}^{(j)} \dot{\mathbf{e}}^{(j)} \right] \tag{2.17}$$

which form will be used in the next chapter to define generalized nonconservative forces in the discrete Langrange equations for the particle-element system.

10

2.4 Finite Element Kinematics

The element kinematics take a large strain Lagrangian form. The strain tensor is

$$\mathbf{E}^{(j)} = \frac{1}{2}\left(\mathbf{C}^{(j)} - \mathbf{I}\right) \tag{2.18}$$

where the right Cauchy-Green strain tensor and deformation gradient are

$$\mathbf{C}^{(j)} = \mathbf{F}^{(j)T}\mathbf{F}^{(j)}, \qquad \mathbf{F}^{(j)} = \frac{\partial \mathbf{x}^{(j)}}{\partial \mathbf{X}^{(j)}} \tag{2.19}$$

and $\mathbf{x}^{(j)}$ and $\mathbf{X}^{(j)}$ are the position vectors of particle j in the current and reference configuration respectively.

The elastic strain tensor is defined as

$$\mathbf{E}^{e(j)} = \mathbf{E}^{(j)} - \mathbf{E}^{p(j)} \tag{2.20}$$

where $\mathbf{E}^{p(j)}$ is the plastic strain tensor. For imcompressible plastic flow the evolution equations for the plastic strain satisfy

$$tr\left(\mathbf{C}^{p(j)-T}\dot{\mathbf{C}}^{p(j)}\right) = 0, \qquad \mathbf{E}^{p(j)} = \frac{1}{2}\left(\mathbf{C}^{p(j)} - \mathbf{I}\right) \tag{2.21}$$

where $\mathbf{C}^{p(j)}$ is the right Cauchy-Green plastic deformation tensor, and the superscript $-T$ denotes the transpose of the inverse.

2.5 Generation of the particle model

This section describes an algorithm for the generation of an ellipsoidal particle model on a general hexahedral mesh. The particles are located at the

11

hex nodes; hence this algorithm determines their mass, volume, and orientation. Note that mass and volume are determined independently, to ensure proper compressive stiffness of the element array, even in the case of a highly unstructured mesh.

The algorithm proceeds as follows (in this algorithm the index i is for nodes and index j is for elements):

1. Compute a deformation gradient $\mathbf{F}^{(j)}$ for each element, mapping each element in the reference configuration to a single master element.

2. Compute a normalized deformation gradient $\overline{\mathbf{F}}^{(j)}$ for each element

$$\overline{\mathbf{F}}^{(j)} = \left(\mathbf{J}^{(j)}\right)^{-\frac{1}{3}} \mathbf{F}^{(j)}, \qquad \mathbf{J}^{(j)} = \det \mathbf{F}^{(j)} \tag{2.22}$$

3. Compute a left Cauchy-Green strain tensor $\overline{\mathbf{B}}^{(j)}$ for each element

$$\overline{\mathbf{B}}^{(j)} = \overline{\mathbf{F}}^{(j)} \, \overline{\mathbf{F}}^{(j)T} \tag{2.23}$$

4. Compute the mass $m^{(j)}$ for each element

$$m^{(j)} = V^{(j)} \rho_0, \qquad V^{(j)} = |\det \mathbf{F}^{(j)}| V_0 \tag{2.24}$$

where $V^{(j)}$ and V_o are the element volume in the reference configuration and the master element volume respectively.

5. Compute the mass $m^{n(i)}$ for each particle

$$m^{n(i)} = \frac{1}{8} \sum_{j=1}^{n_e} m^{(j)} f_{ij} \qquad (2.25)$$

where f_{ij} is 1 if node i is in element j, and 0 otherwise.

6. Compute a left Cauchy-Green strain tensor $\mathbf{B}^{(i)}$ for each particle

$$\mathbf{B}^{(i)} = \frac{0.125}{m^{n(i)}} \sum_{j=1}^{n_e} m^{(j)} \overline{\mathbf{B}}^{(j)} f_{ij} \qquad (2.26)$$

where i and j are indices for nodes and elements respectively.

7. Compute a normalized left Cauchy-Green strain tensor $\overline{\mathbf{B}}^{(i)}$ for each particle

$$\overline{\mathbf{B}}^{(i)} = \left(\mathbf{J}^{(i)}\right)^{-\frac{1}{3}} \mathbf{B}^{(i)}, \qquad \mathbf{J}^{(i)} = \det \mathbf{B}^{(i)} \qquad (2.27)$$

8. Compute the eigenvalues $\lambda_k^{(i)}$ and eigenvectors of $\overline{\mathbf{B}}^{(i)}$

9. Compute the semimajor axes for each particle, as follows. First compute the radius of the mass equivalent sphere

$$r^{(i)} = \left(\frac{3}{4\pi} \frac{m^{n(i)}}{\rho}\right)^{\frac{1}{3}} \qquad (2.28)$$

Next compute a scaling factor $\alpha^{(i)}$

$$\alpha^{(i)} = max\left[1, \quad \left(\frac{m_r^{(i)}}{m^{n(i)}}\right)^{\frac{1}{3}}\right] \qquad (2.29)$$

where $m_r^{(i)}$ is the mass of the largest volume element associated with node i, this is important in general hex meshes, as shown in Figure 2.8. The semimajor axes of the ellipsoid are then

$$h_k{}^{(i)} = \alpha^{(i)} \left(\lambda_k^{(i)}\right)^{\frac{1}{2}} r^{(i)}, \quad k = 1, 2, 3 \tag{2.30}$$

10. Assemble the direction cosine matrix, with components $c_{ij}^{(i)}$. The direction cosine matrix is composed of the eigenvectors of $\overline{\mathbf{B}}^{(i)}$.

11. Compute Euler parameters $\mathbf{e}^{(i)}$ for the particles [2].

The Euler parameters are computed in two steps. First the Euler parameter of largest magnitude is determined, using the following equations

$$4(e_0{}^{(i)})^2 = c_{11}^{(i)} + c_{22}^{(i)} + c_{33}^{(i)} + 1 \tag{2.31a}$$

$$4(e_1{}^{(i)})^2 = c_{11}^{(i)} - c_{22}^{(i)} - c_{33}^{(i)} + 1 \tag{2.31b}$$

$$4(e_2{}^{(i)})^2 = -c_{11}^{(i)} + c_{22}^{(i)} - c_{33}^{(i)} + 1 \tag{2.31c}$$

$$4(e_3{}^{(i)})^2 = -c_{11}^{(i)} - c_{22}^{(i)} + c_{33}^{(i)} + 1 \tag{2.31d}$$

where c_{ij} are the elements of the direction cosine matrix.

Once the Euler parameter of largest magnitude is determined, compute the Euler parameters using the equations

$$c_{21} = 2(e_1^{(i)} e_2^{(i)} + e_0^{(i)} e_3^{(i)}) \tag{2.32a}$$

$$c_{12} = 2(e_1^{(i)} e_2^{(i)} - e_0^{(i)} e_3^{(i)}) \tag{2.32b}$$

14

$$c_{31} = 2(e_1^{(i)}e_3^{(i)} - e_0^{(i)}e_2^{(i)}) \tag{2.32c}$$

$$c_{13} = 2(e_1^{(i)}e_3^{(i)} + e_0^{(i)}e_2^{(i)}) \tag{2.32d}$$

$$c_{32} = 2(e_2^{(i)}e_3^{(i)} + e_0^{(i)}e_1^{(i)}) \tag{2.32e}$$

$$c_{23} = 2(e_2^{(i)}e_3^{(i)} - e_0^{(i)}e_1^{(i)}) \tag{2.32f}$$

For example, if e_0 is the largest in magnitude, compute the Euler parameters from

$$e_0 = \frac{1}{2}(c_{11} + c_{22} + c_{33} + 1)^{\frac{1}{2}} \tag{2.33a}$$

$$e_1 = \frac{c_{32} - c_{23}}{4e_0} \tag{2.33b}$$

$$e_2 = \frac{c_{13} - c_{31}}{4e_0} \tag{2.33c}$$

$$e_3 = \frac{c_{21} - c_{12}}{4e_0} \tag{2.33d}$$

2.6 Examples

This section describes six examples used to illustrate how a general hexahedral mesh is translated into a particle model. The first example is a cylinder with a mesh generated using commercial software. The top face of the cylinder is shown in Figure 2.9. The particle model for this example is shown in Figure 2.10.

The second example is a cylindrical projectile for one of the simulations used to validate the formulation presented in this work. The projectile diameter is 4.36 cm and its length is 5.16 cm. Figure 2.11 shows a four way

15

symmetric mesh for the cylinder; this mesh has 1,152 elements and 1,469 nodes. The minimum edge ratio is 1.0, the maximum edge ratio (the edge ratio is the ratio of the longest edge length to the shortest edge length) is 1.70 and the ratio of maximum to minimum element volumes is 2.3. Figure 2.12 illustrates the particle model for the projectile.

The third example is a plate with a non-uniform mesh; Figure 2.13 shows how the aspect ratio and size of the elements vary throughout the plate. Figure 2.14 illustrates the particle model for this example; note that ellipsoidal particles can represent this type of mesh very effectively.

The fourth example is a plate with a gradual transition of the size and aspect ratio of the elements. In the radial direction the element length is increasing, with the ratio of outer element to inner element length being 2. Figure 2.15 shows a two dimensional view of the mesh and Figure 2.16 shows the corresponding particle model. Figures 2.17 and 2.18 show a three dimensional view of the mesh and the particle model respectively.

The fifth example is a spherical projectile used in one of the validation simulations. The sphere diameter is 1.0 cm, and the finite element model consists of 1,600 elements and 1,933 nodes. The minimum edge ratio is 1.0, the maximum edge ratio is 1.5, and the maximum volume ratio is 14.5. Figure 2.19 and Figure 2.20 illustrate the mesh and the particle model respectively.

The last example is the representation of a rod formed by a cylinder and hemispherical cap. This model is similar to the projectile used in one

16

of the validation simulations. Figure 2.21 shows the mesh, which has 2,368 elements and 2,938 nodes. The minimum edge ratio is 1.0, the maximum edge ratio is 1.7 and the maximum volume ratio is 11.5. Figure 2.22 depicts the particle model.
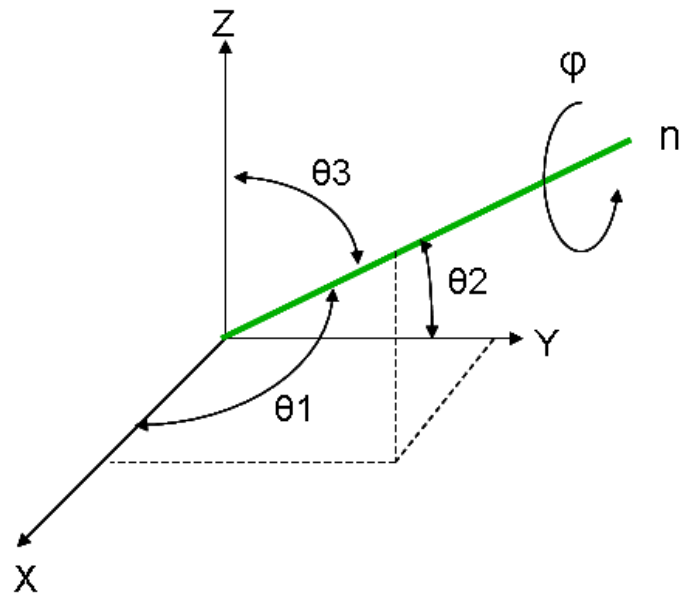
$$c1 = \cos\theta1 \; ; \; c2 = \cos\theta2 \; ; \; c3 = \cos\theta3$$

$$e0 = \cos(\varphi/2) \; ; \; e1 = c1*\sin(\varphi/2) \; ; \; e2 = c2*\sin(\varphi/2) \; ; \; e3 = c3*\sin(\varphi/2)$$

Figure 2.1: Euler parameters related to a general rotation about a point.
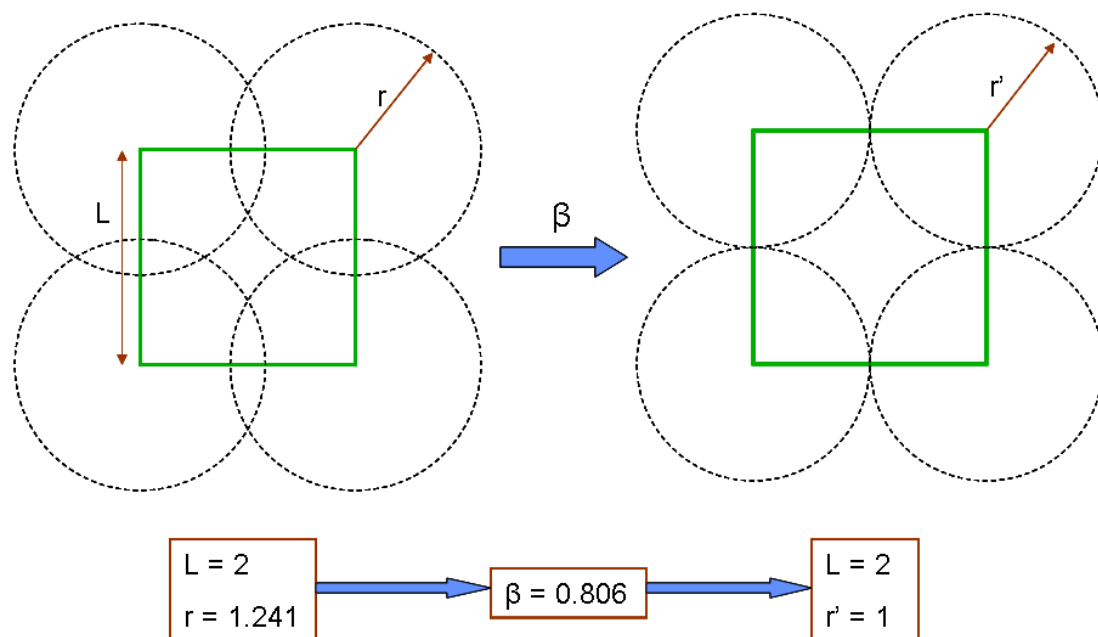
Figure 2.2: Effect of parameter β in packing of particles.
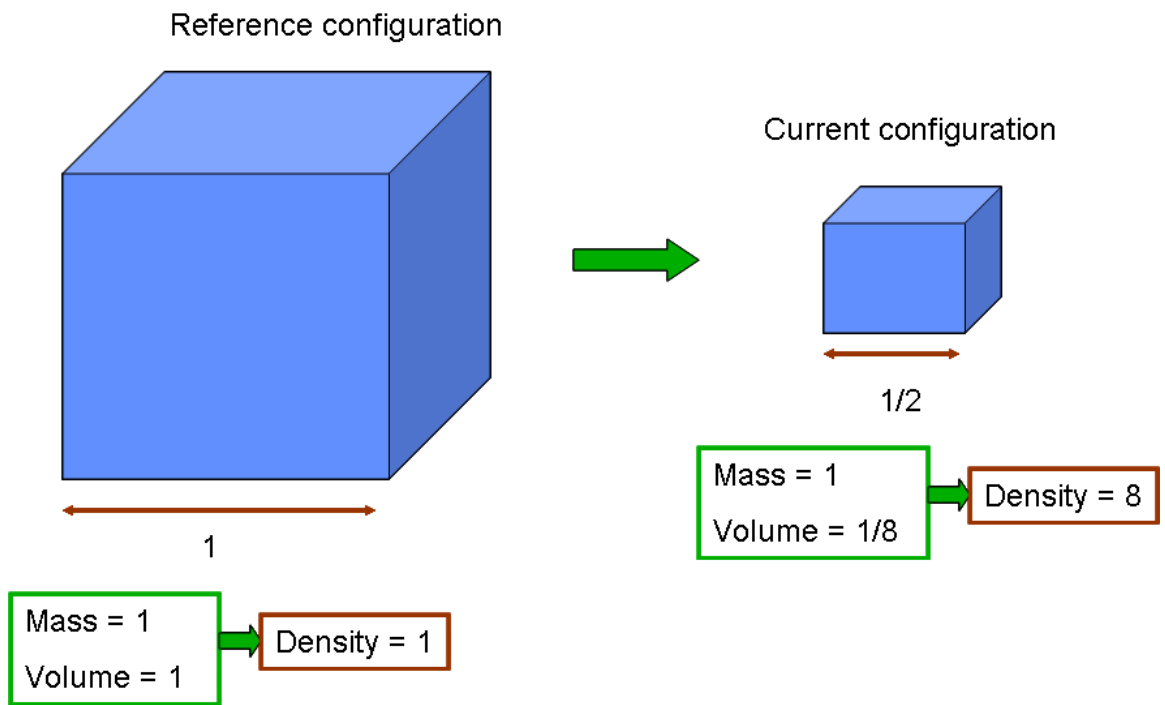
Figure 2.3: Uniform compression in a cube.
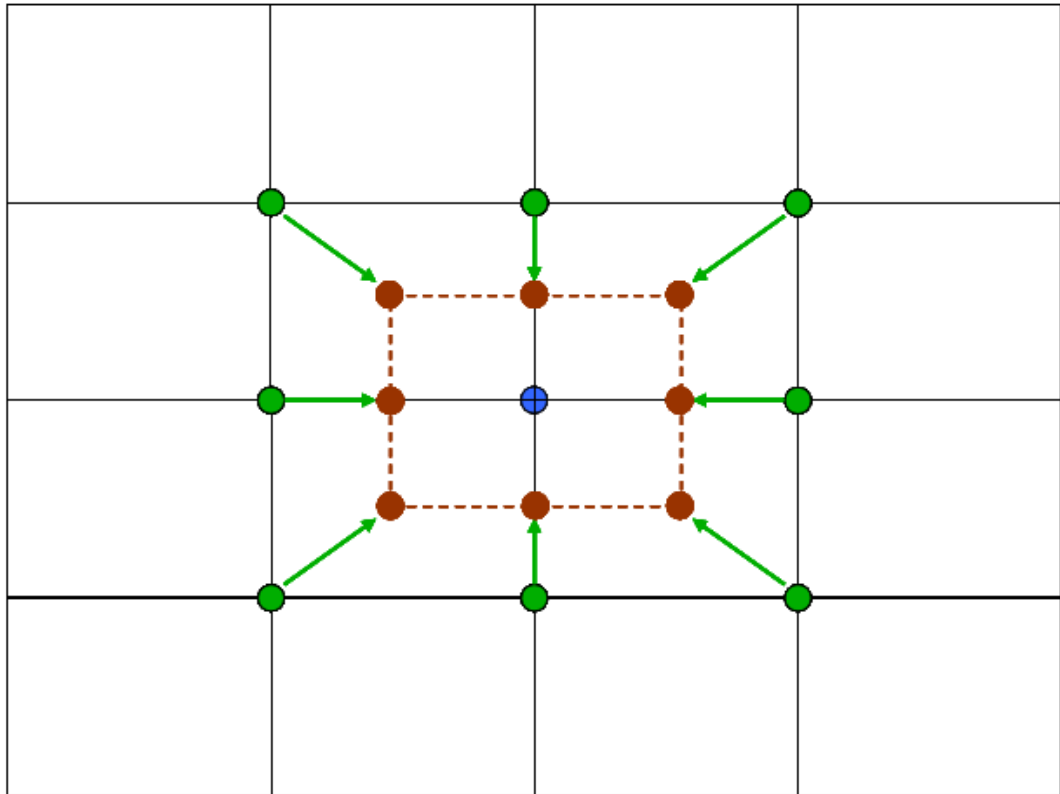
Figure 2.4: Uniform compression in a mesh.

$$\frac{\rho^{(i)}}{\rho_o^{(i)}} = 1 + \frac{1}{N^{(i)}} \sum_{j=1}^{n} \left[\left(\frac{\zeta^{R(i,j)}}{\zeta^{(i,j)}} \right)^3 - 1 \right] W^{(i,j)}$$

$$\zeta^{(i,j)} = 1/2$$

$$\left(\frac{\zeta^{R(i,j)}}{\zeta^{(i,j)}} \right)^3 = 8$$

$$\frac{\rho^{(i)}}{\rho_o^{(i)}} = 8$$
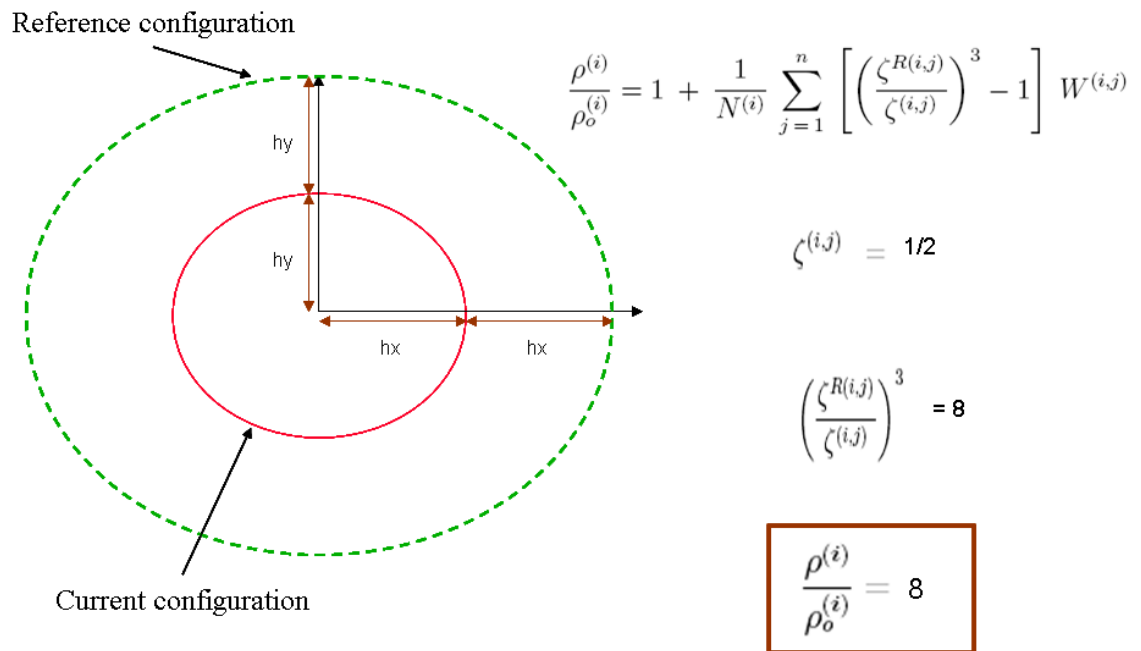
Figure 2.5: Density increase due to uniform compression in a general mesh
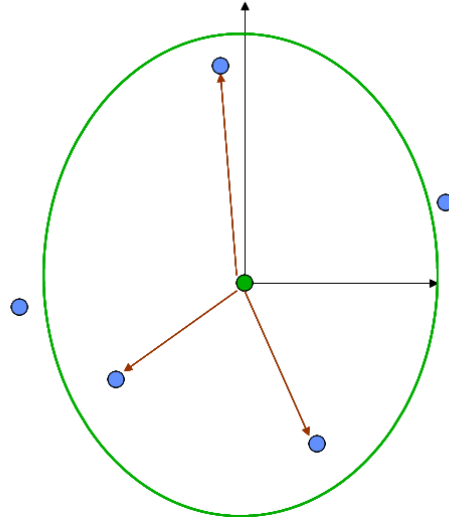
Figure 2.6: Orientation effect, particle in a reference configuration
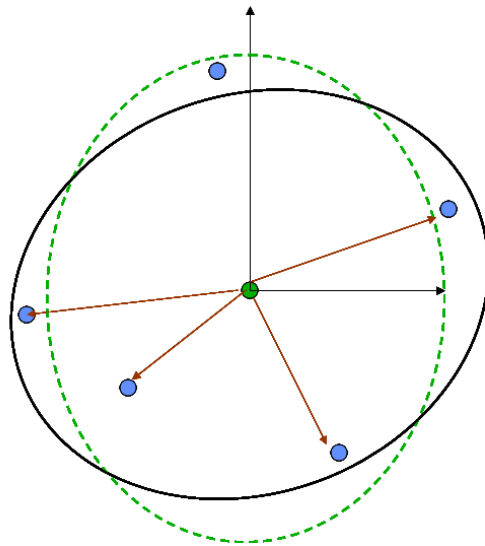
Figure 2.7: Orientation effect, particle in a current configuration

Largest element associated with the particle
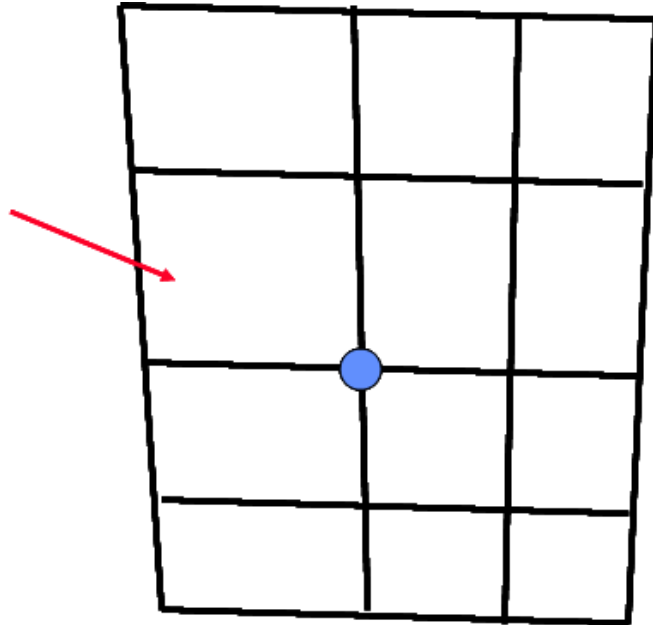
The contribution of each element associated with a particle is different

Figure 2.8: Effect of different element sizes associated with a particle
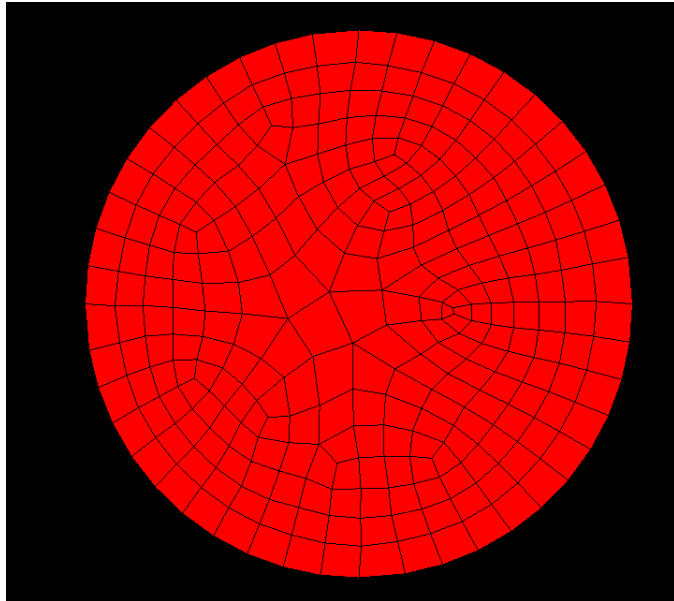
Figure 2.9: Example 1, cylinder mesh.
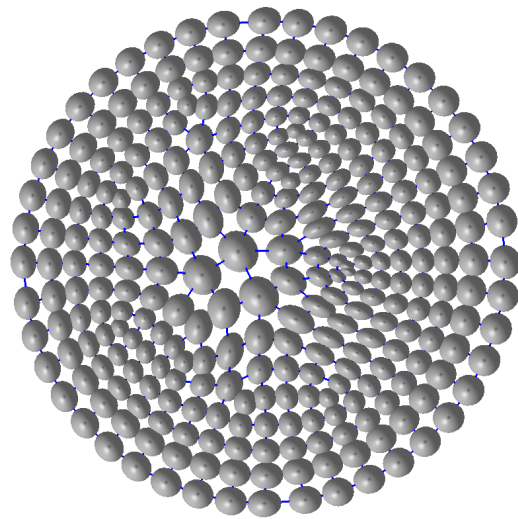
Figure 2.10: Example 1, particle model.
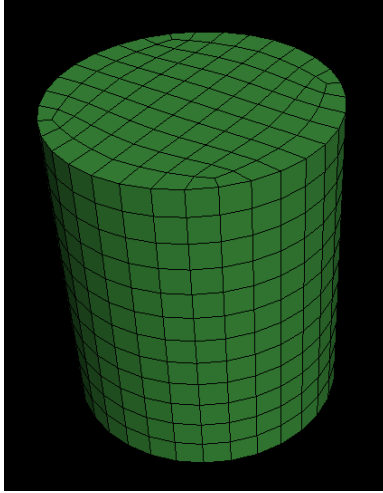
Figure 2.11: Example 2, cylindrical projectile mesh.
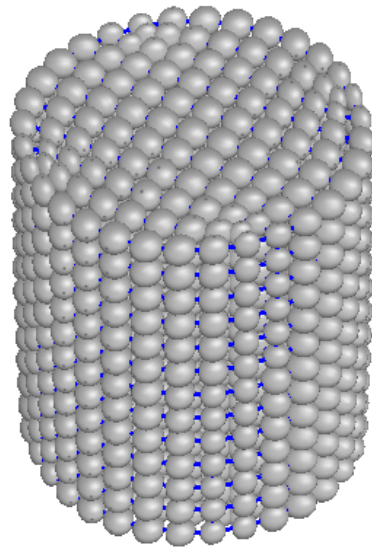
Figure 2.12: Example 2, cylindrical projectile particle model.
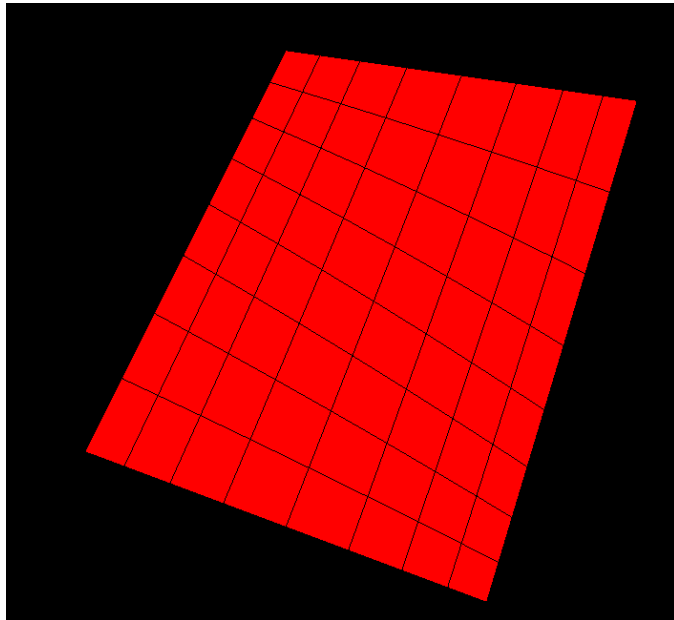
Figure 2.13: Example 3, plate mesh.
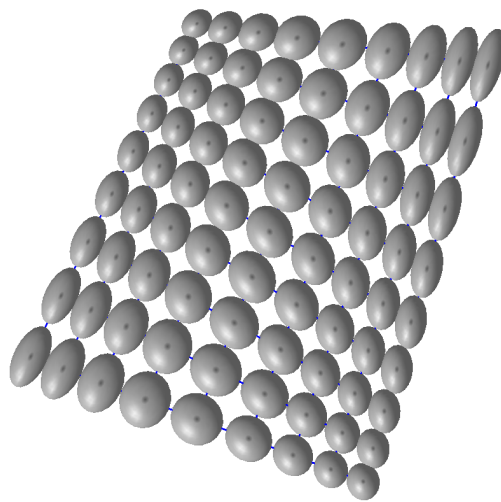
Figure 2.14: Example 3, particle model.
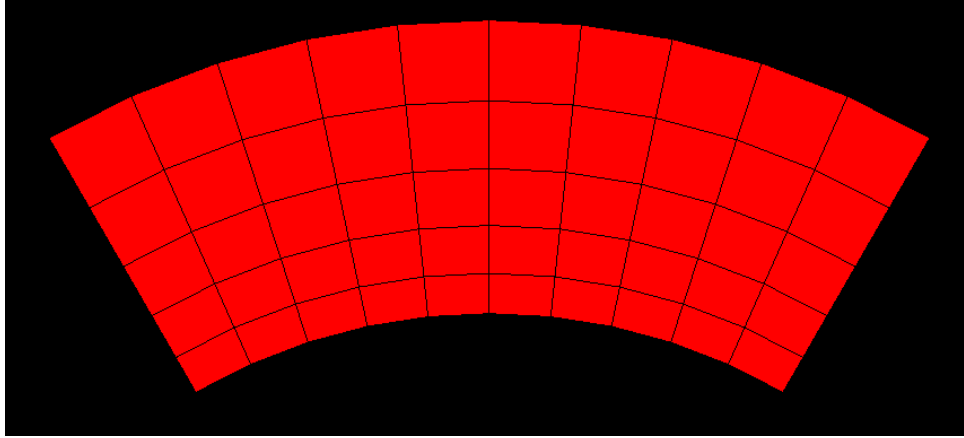
Figure 2.15: Example 4, plate mesh.
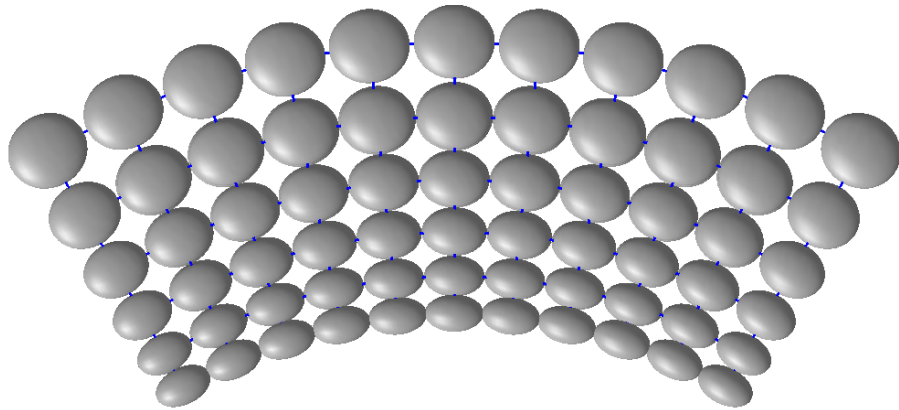
Figure 2.16: Example 4, particle model.
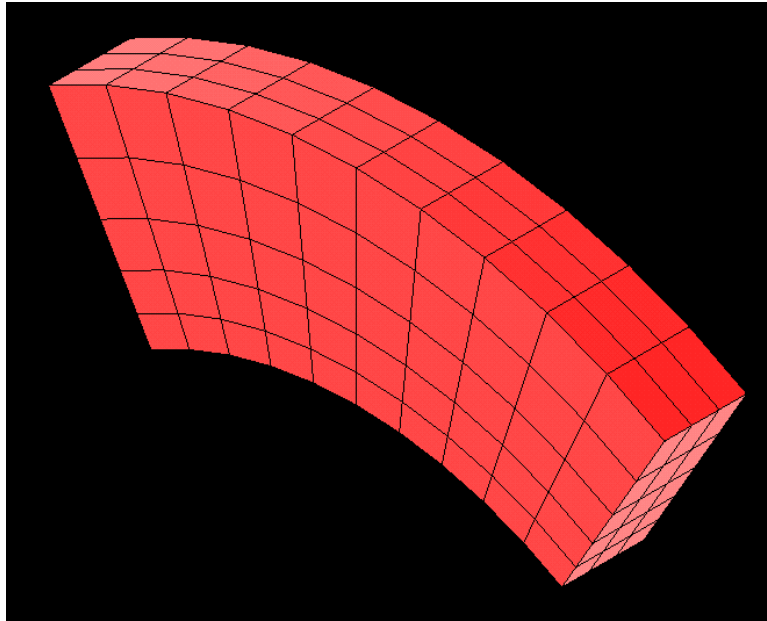
Figure 2.17: Example 4, plate mesh three dimensional view.
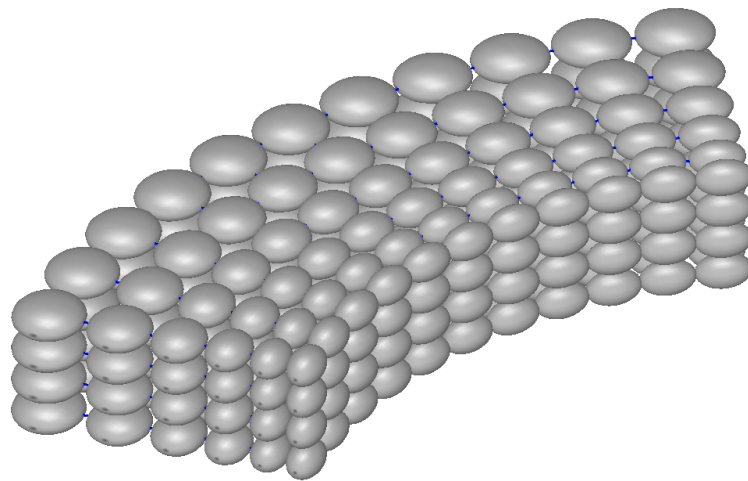
Figure 2.18: Example 4, particle model three dimensional view.
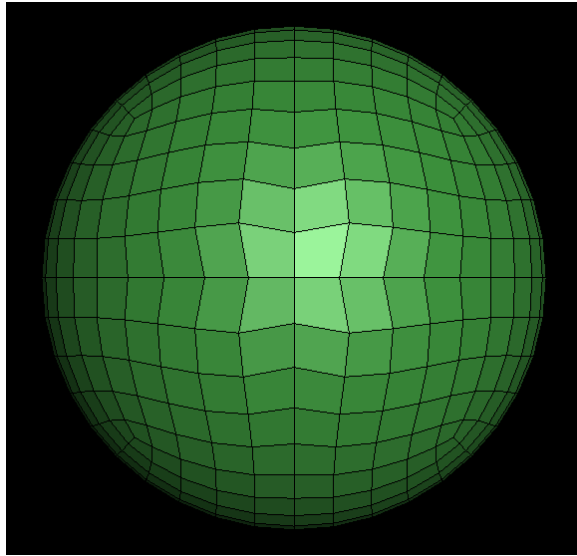
Figure 2.19: Example 5, spherical projectile mesh.
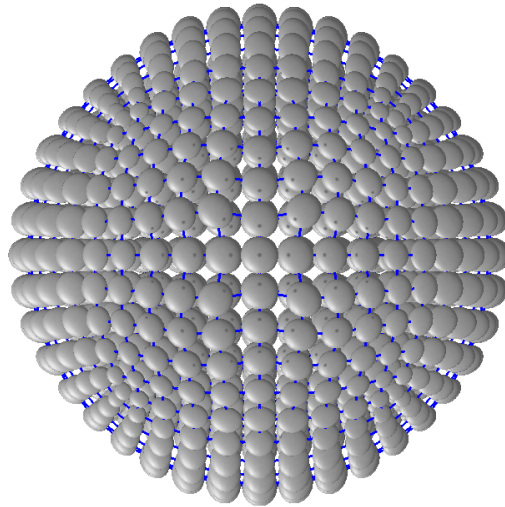
Figure 2.20: Example 5, spherical projectile particle model.
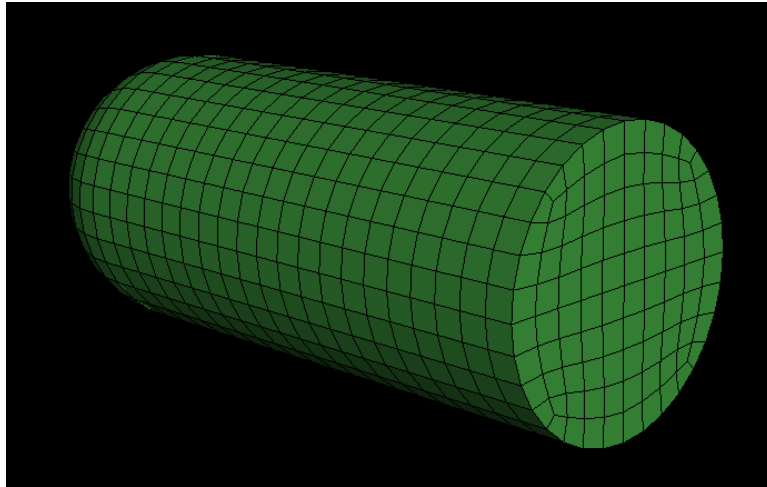
Figure 2.21: Example 6, rod mesh.
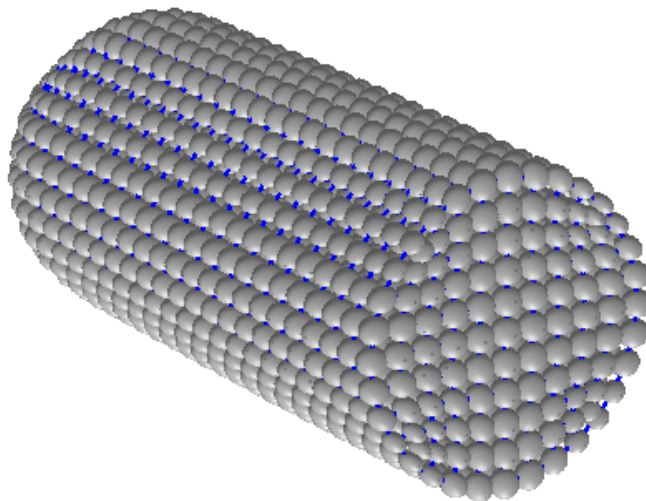
Figure 2.22: Example 6, rod particle model.

Chapter 3

Discrete Lagrange Equations

3.1   Introduction

This chapter develops discrete Lagrange equations for the particle-element system. It incorporates stored energy functions and dissipative constitutive relations for very general thermomechanical materials. The nonholonomic model developed here is well suited for extension to additional energy domains. The formulation is validated by comparing simulation results to data from several published three dimensional impact experiments.

3.2   Kinetic Co-Energy

The system kinetic co-energy is

$$T^* \; = \; \sum_{i\,=\,1}^{n} T^{*(i)} \tag{3.1}$$

where the total kinetic co-energy (translational and rotational) for particle i is

$$T^{*(i)} = \frac{1}{2}\, m^{(i)}\, \dot{\mathbf{c}}^{(i)\,T} \dot{\mathbf{c}}^{(i)} \; + \; \frac{1}{2}\, \boldsymbol{\omega}^{(i)\,T}\, \mathbf{J}^{(i)}\, \boldsymbol{\omega}^{(i)} \tag{3.2}$$

and all inertial effects are modeled with the particles. The system generalized momenta are

$$\mathbf{p}^{(i)} = \frac{\partial T^*}{\partial \dot{\mathbf{c}}^{(i)}} = m^{(i)} \, \dot{\mathbf{c}}^{(i)} \,, \qquad \mathbf{h}^{(i)} = \frac{\partial T^*}{\partial \boldsymbol{\omega}^{(i)}} = \mathbf{J}^{(i)} \, \boldsymbol{\omega}^{(i)} \qquad (3.3)$$

where the center of mass velocities are described in a fixed Cartesian frame and the angular velocities are described in a body-fixed co-rotating frame aligned with the principal axes of inertia of the particles.

3.3 Potential Energy

The system potential energy depends on both the particles and the elements. The particle total internal energies $U^{(i)}$ are taken as generalized coordinates (not the total set of generalized coordinates), while strength effects are modeled using a strain energy density function for the elements:

$$V = \sum_{i=1}^{n} U^{(i)} + \sum_{j=1}^{n_e} V_o^{e(j)} \, \psi^{(j)} \qquad (3.4)$$

where n is the number of particles, n_e is the number of elements, $V_o^{e(j)}$ is the reference volume of element j, and $\psi^{(j)}$ a strain energy density function. Assuming a linear elasticity model for the elements,

$$\psi^{(j)} = \left(1 - d^{(j)}\right) \mu^{(j)} \, tr \left(\mathbf{E}^{e(j)^T} \mathbf{E}^{e(j)} \right) \qquad (3.5)$$

where $\mu^{(j)}$ is a shear modulus, $d^{(j)}$ is a shear damage variable, and $\mathbf{E}^{e(j)}$ is the elastic strain tensor for element j. As noted in the chapter on kinematics, the elastic strain tensor depends on the nodal coordinates and the plastic strain

$$\mathbf{E}^{e(j)} = \mathbf{E}^{e(j)} \left(\mathbf{c}^{(i)}, \mathbf{E}^{p(j)} \right) \qquad (3.6)$$

33

so that the final functional form for the stored energy is

$$V = V\left(U^{(i)}, \mathbf{c}^{(i)}, d^{(j)}, \mathbf{E}^{p(j)}\right) \tag{3.7}$$

where the particle internal energies $U^{(i)}$, particle center of mass position vectors $c^{(i)}$, the element shear damage variables $d^{(j)}$, and element plastic strain tensors $\mathbf{E}^{p(j)}$ are the entire set of generalized coordinates.

The generalized conservative forces for particle i are therefore

$$1 = \frac{\partial V}{\partial U^{(i)}}, \qquad \mathbf{f}^{(i)} = \frac{\partial V}{\partial \mathbf{c}^{(i)}} \tag{3.8}$$

Note that the derivative with respect to internal energy is one.

The elastic stress tensor and the damage strain energy release rate are

$$\mathbf{S}^{(j)} = -\frac{1}{V_o^{e(j)}} \frac{\partial V}{\partial \mathbf{E}^{p(j)}}, \qquad \Gamma^{d(j)} = -\frac{\partial V}{\partial d^{(j)}} \tag{3.9}$$

This formulation admits equations of state in general thermomechanical form, and may be generalized, for example to anisotropic materials.

3.4 Plasticity and Damage Models

The dissipative material models used here incorporate large strain kinematics and a general thermomechancial dependence. The models are adapted from references [21, 49], and the plastic flow rule is

$$\dot{\mathbf{E}}^{p(j)} = \frac{\dot{\lambda}^{(j)}}{||S^{p(j)}||} \underline{\underline{\mathbf{N}}}^{p(j)} \underline{\underline{\mathbf{N}}} \, \mathbf{S}^{p(j)} \tag{3.10}$$

where $\dot{\lambda}^{(j)}$ is a positive coefficient, $\mathbf{S}^{p(j)}$ is an effective deviatoric stress, the stress tensor used in the yield function.

$$\mathbf{S}^{p(j)} = \underline{\underline{\mathbf{N}}}^T \, \underline{\underline{\mathbf{N}}}^{p(j)T} \, \mathbf{S}^{(j)} \tag{3.11}$$

with $\mathbf{S}^{(j)}$ a deviatoric stress tensor. The moduli in the flow rule are

$$\underline{\underline{\mathbf{N}}}^{p(j)} \, \mathbf{T} = \frac{1}{2 \, ||C^{p(j)}||} (\mathbf{C}^{p(j)} \, \mathbf{T} + \mathbf{T} \, \mathbf{C}^{p(j)}) \tag{3.12}$$

where $\mathbf{T}$ is any second order tensor, $\mathbf{C}^{p(j)}$ is the right Cauchy-Green plastic deformation tensor, and

$$\underline{\underline{\mathbf{N}}} \, \mathbf{T} = \mathbf{T} - \frac{1}{3} tr(\mathbf{T}) \, \mathbf{I} \tag{3.13}$$

with $\mathbf{I}$ the identity tensor and

$$||\mathbf{T}|| = \left[\frac{1}{2} \, tr \left(\mathbf{T}^T \mathbf{T} \right) \right]^{1/2} \tag{3.14}$$

Note that $\underline{\underline{\mathbf{N}}}^{p(j)}$ is used to enforce the plastic incompressibility constraint. The yield function is

$$f^{(j)} = ||S^{p(j)}|| - Y^{(j)} \tag{3.15}$$

where $Y^{(j)}$ is the yield stress

$$Y^{(j)} = Y_o^{(j)} \left(1 - d^{(j)}\right) \left(1 + \kappa^{(j)} \epsilon^{p(j)}\right)^{\alpha^{(j)}} \left(1 - \eta^{(j)} \theta^{H(j)}\right) \tag{3.16}$$

In the last equation $Y_o^{(j)}$ is the reference yield stress, $\kappa^{(j)}$ is a strain hardening coefficient, $\epsilon^{p(j)}$ is the effective plastic strain, $\alpha^{(j)}$ is a strain hardening exponent, $\eta^{(j)}$ is a thermal softening coefficient, and $\theta^{H(j)}$ is the homologous temperature, defined by

$$\theta^{H(j)} = \frac{\theta - \theta_o}{\theta_m - \theta_o} \tag{3.17}$$

with θ the temperature, θ_o the reference temperature, and θ_m the melting temperature. The accumulated plastic strain is obtained by integrating the rate equation

$$\dot{\epsilon}^{p(j)} = ||\dot{\mathbf{E}}^{p(j)}|| \tag{3.18}$$

This rate independent plasticity model is implemented in incremental form, with

$$\Delta\lambda^{(j)} = \frac{< ||S^{p(j)}|| - Y^{(j)} >}{(1 - d^{(j)})\, 2\, \mu^{(j)}} \tag{3.19}$$

determining the scalar multiplier for the plastic strain increment. Here $<>$ are the Mcauley brackets (i.e. $< x >= x$ if $x > 0$ and $x = 0$ otherwise).

A simple damage evolution relation

$$\dot{d}^{(j)} = \frac{\Lambda^{(j)}}{\Delta t}\, \hat{u}(1 - d^{(j)}) \tag{3.20}$$

is used here for the sole purpose of modeling the transition from an intact to a comminuted medium. The parameter $\Lambda^{(j)}$ is the damage increment in one time step, taken in the example simulations to be one half.

3.5 Artificial Viscosity

The artificial viscosity formulation used here is typical of shock physics codes, except that the use here of ellipsoidal particles requires the introduction of a damping torque. The damping force acting at the particle centers of mass is

$$\mathbf{f}^{v(i)} = \sum_{j=1}^{n} \nu^{(i,j)}\, max\left(0, v^{(i,j)}\right) \frac{\left(\mathbf{c}^{(i)} - \mathbf{c}^{(j)}\right)}{|\,\mathbf{c}^{(i)} - \mathbf{c}^{(j)}\,|}\, \hat{u}(1 - \zeta^{(i,j)}) \tag{3.21}$$

36

where $v^{(i,j)}$ is the relative normal velocity

$$v^{(i,j)} = -\left(\dot{\mathbf{c}}^{(i)} - \dot{\mathbf{c}}^{(j)} \right) \cdot \frac{\left(\mathbf{c}^{(i)} - \mathbf{c}^{(j)} \right)}{|\, \mathbf{c}^{(i)} - \mathbf{c}^{(j)} \,|} \tag{3.22}$$

and $\nu^{(i,j)}$ the numerical viscosity

$$\nu^{(i,j)} = \frac{c_o}{2} \left(\rho_o^{(i)} \, c_s^{(i)} V_o^{(i)\frac{2}{3}} + \rho_o^{(j)} \, c_s^{(j)} V_o^{(j)\frac{2}{3}} \right) \left[1 + \frac{2\, c_1 |v^{(i,j)}|}{(c_s^{(i)} + c_s^{(j)})} \right] \tag{3.23}$$

and contains both linear and quadratic terms, where c_o and c_1 are nondimen-sional numerical viscosity coefficients, c_s is the soundspeed for particle i, and $V_o^{(i)}$ is the reference volume for the particle. The damping torque is

$$\mathbf{M}^{v(i)} = \sum_{j=1}^{n} \sigma^{(i,j)} \, \mathbf{R}^{(i)T} \left(\mathbf{R}^{(i)} \boldsymbol{\omega}^{(i)} - \mathbf{R}^{(j)} \boldsymbol{\omega}^{(j)} \right) \hat{u}(1 - \zeta^{(i,j)}) \tag{3.24}$$

where the torsional damping coefficient define between particles i and j is

$$\sigma^{(i,j)} = \frac{c_o}{2} \left(\rho_o^{(i)} \, c_s^{(i)} V_o^{(i)\frac{4}{3}} + \rho_o^{(j)} \, c_s^{(j)} V_o^{(j)\frac{4}{3}} \right) \tag{3.25}$$

3.6   Internal Energy Evolution Equations

In the thermomechanical Lagrange equation formulation used here, the particle internal energies are generalized coordinates. Their evolution relations are

$$\dot{U}^{(i)} = \dot{U}^{com(i)} + \dot{U}^{irr(i)} - \dot{U}^{con(i)} \tag{3.26}$$

where the three terms represent work done in particle compression $\dot{U}^{com(i)}$, irreversiblle entropy production $\dot{U}^{irr(i)}$, and numerical heat diffusion $\dot{U}^{con(i)}$. The compression term is simply

$$\dot{U}^{com(i)} = -\frac{m^{(i)} \, P^{(i)}}{\rho^{(i)2}} \, \dot{\rho}^{(i)} \tag{3.27}$$

37

where $P^{(i)}$ is the pressure. The irreversible entropy production is associated with viscous forces and torques, as well as conduction (to the particles) of energy dissipated in the elements

$$\dot{U}^{irr(i)} = \mathbf{f}^{v(i)^T} \dot{\mathbf{c}}^{(i)} + \mathbf{M}^{v(i)^T} \boldsymbol{\omega}^{(i)} + \sum_{j=1}^{n} \phi^{(i,j)} \, \dot{Q}^{irr(j)} \tag{3.28}$$

with $\mathbf{f}^{v(i)}$ a viscous force, $\mathbf{M}^{v(i)}$ a viscous torque, $\phi^{(i,j)}$ the fraction of the dissipation in element j transmitted to particle i, and $\dot{Q}^{irr(j)}$ the power flow due to shear damage evolution and plastic deformation in element j

$$\dot{Q}^{irr(j)} = \Gamma^{d(j)} \dot{d}^{(j)} + V_o^{e(j)} \, tr\left(\mathbf{S}^{(j)T} \dot{\mathbf{E}}^{p(j)} \right) \tag{3.29}$$

Finally the numerical heat diffusion is

$$\dot{U}^{con(i)} = R^{(i,j)} \left(\theta^{(i)} - \theta^{(j)} \right) \tag{3.30}$$

where the numerical heat transfer coefficient is

$$R^{(i,j)} = \frac{k_o}{2} \left(\rho_o^{(i)} c_s^{(i)} c_v^{(i)} V_o^{(i)\frac{2}{3}} + \rho_o^{(j)} c_s^{(j)} c_v^{(j)} V_o^{(j)\frac{2}{3}} \right) \tag{3.31}$$

with k_o a numerical heat diffusion coefficient and $c_v^{(i)}$ the specific heat at constant volume.

3.7 Lagrange's Equations

The canonical Lagrange equations for the particle element system are

$$\dot{\mathbf{p}}^{(i)} = -\mathbf{f}^{(i)} + \mathbf{q}^{c(i)}, \qquad \dot{\mathbf{c}}^{(i)} = m^{(i)-1} \, \mathbf{p}^{(i)} \tag{3.32}$$

$$\dot{\mathbf{h}}^{(i)} = -\mathbf{\Omega}^{(i)}\mathbf{h}^{(i)} + \mathbf{Q}^{c(i)}, \qquad \dot{\mathbf{e}}^{(i)} = \frac{1}{2}\mathbf{G}^{(i)T}\mathbf{J}^{(i)-1}\mathbf{h}^{(i)} \qquad (3.33)$$

where

$$\frac{\partial V}{\partial d^{(j)}} = Q^{d(j)}, \qquad \frac{\partial V}{\partial U^{(j)}} = Q^{U(j)}, \qquad \frac{\partial V}{\partial \mathbf{E}^{p(j)}} = \mathbf{Q}^{p(j)} \qquad (3.34)$$

with $\mathbf{q}^{c(i)}$, $\mathbf{Q}^{c(i)}$, $Q^{U(i)}$, $Q^{d(i)}$, and $\mathbf{Q}^{p(j)}$ the generalized forces determined by the nonholonomic constraints. Introducing Lagrange multipliers $\gamma^{U(i)}$, $\gamma^{d(j)}$, and $\mathbf{X}^{p(j)}$ for the constraints, which are the evolution equations for internal energy, damage, and plastic strain, yields

$$
\begin{aligned}
\mathbf{q}^{c(i)} &= -\gamma^{U(i)}\,\mathbf{f}^{v(i)} + \frac{3}{N^{(i)}}\sum_{j=1}^{n}\left[\gamma^{U(i)}\,\zeta^{R(i,j)3}\,\rho_o^{(i)}\frac{W^{(i,j)}}{\zeta^{(i,j)5}}\hat{\mathbf{H}}^{(j)}\mathbf{r}^{(i,j)}\right. \\
&\qquad\qquad \left. -\gamma^{U(j)}\,\zeta^{R(j,i)3}\,\rho_o^{(j)}\frac{W^{(j,i)}}{\zeta^{(j,i)5}}\hat{\mathbf{H}}^{(i)}\mathbf{r}^{(j,i)}\right] \qquad (3.35) \\
\mathbf{Q}^{c(i)} &= -\gamma^{U(i)}\,\mathbf{M}^{v(i)} \\
&\quad +\frac{3}{N^{(i)}}\sum_{j=1}^{n}\gamma^{U(j)}\,\zeta^{R(j,i)3}\,\rho_o^{(j)}\frac{W^{(j,i)}}{\zeta^{(j,i)5}}\left(\mathbf{H}^{(i)}\hat{\mathbf{r}}^{(j,i)}\times\hat{\mathbf{r}}^{(j,i)}\right) \qquad (3.36) \\
Q^{U(i)} &= \gamma^{U(i)} \qquad (3.37) \\
Q^{d(j)} &= \gamma^{d(j)} - \sum_{i=1}^{n}\gamma^{U(i)}\,\phi^{(i,j)}\,\Gamma^{d(j)} \qquad (3.38) \\
\mathbf{Q}^{p(j)} &= \mathbf{X}^{p(j)} - \sum_{i=1}^{n}\gamma^{U(i)}\,\phi^{(i,j)}\,V_o^{(j)}\,\mathbf{S}^{(j)} \qquad (3.39)
\end{aligned}
$$

The unknown Lagrange multipliers may be determined in closed form, using the degenerate Lagrange equations for internal energy, damage, and plastic strain. The last terms in equations 3.35 and 3.36 arise from the work

done in particle compression. The final Lagrange equations are

$$\dot{\mathbf{p}}^{(i)} = -\mathbf{f}^{(i)} - \mathbf{f}^{v(i)} + \mathbf{q}^{(i)} \tag{3.40}$$

$$\dot{\mathbf{h}}^{(i)} = -\boldsymbol{\Omega}^{(i)}\mathbf{h}^{(i)} - \mathbf{M}^{v(i)} + \mathbf{Q}^{(i)} \tag{3.41}$$

$$\dot{\mathbf{c}}^{(i)} = m^{(i)-1}\mathbf{p}^{(i)} \tag{3.42}$$

$$\dot{\mathbf{e}}^{(i)} = \frac{1}{2}\mathbf{G}^{(i)T}\mathbf{J}^{(i)-1}\mathbf{h}^{(i)} \tag{3.43}$$

where the generalized forces and torques due to particle interactions are

$$
\begin{aligned}
\mathbf{q}^{(i)} &= \frac{3}{N^{(i)}} \sum_{j=1}^{n} \left(V_o^{(i)} \, \zeta^{R(i,j)3} \, \frac{P^{(i)}}{\rho^{(i)2}} \, \frac{W^{(i,j)}}{\zeta^{(i,j)5}} \, \hat{\mathbf{H}}^{(j)} \right.\\
&\qquad\qquad \left. + V_o^{(j)} \, \zeta^{R(j,i)3} \, \frac{P^{(j)}}{\rho^{(j)2}} \, \frac{W^{(j,i)}}{\zeta^{(j,i)5}} \, \hat{\mathbf{H}}^{(i)} \right) \mathbf{r}^{(i,j)} \tag{3.44}\\
\mathbf{Q}^{(i)} &= \frac{3}{N^{(i)}} \sum_{j=1}^{n} V_o^{(j)} \, \zeta^{R(j,i)3} \, \frac{P^{(j)}}{\rho^{(j)2}} \, \frac{W^{(j,i)}}{\zeta^{(j,i)5}} \left(\mathbf{H}^{(i)}\hat{\mathbf{r}}^{(j,i)} \times \hat{\mathbf{r}}^{(j,i)} \right) \tag{3.45}
\end{aligned}
$$

3.8 Example Simulations

This section describes three example problems used to validate the model developed in this work. In these simulations chemical reactions were not modeled. The first example involves the impact of an aluminum sphere on an aluminum plate. The experiment is described in references [52] and [53]. The thickness of the plate is 0.25 cm and the diameter of the projectile is 1.0 cm. This is a normal impact problem. The velocity of the projectile is 6.7 km/s and the target is fixed. The model employed 162,380 particles.

The material properties used for the simulation are listed in Table 3.1 and the simulation parameters are listed in Table 3.2.

The meshes for both the target and the projectile are shown in Figure 3.1. The spherical projectile mesh has a mimimum edge ratio of 1.0 and a maximum edge ratio of 1.57; the volume ratio is 14.5. The target has a graded mesh with aspect ratios of 1.5:1.5:1.0 for the elements at the center and 3.0:3.0:1.0 for the elements at the corners; the volume ratio is 4.0. Figures 3.2 and 3.3 plot the maximum aspect ratio for the plate and projectile respectively.

The initial configuration for this impact problem is shown in Figure 3.4. The physical time for the simulation was 25 microseconds. Figures 3.5 (front view) and 3.7 (back view) show the results at 25 microseconds after impact. Figures 3.6 (front view) and 3.8 (back view) show the element plots. The comparison of the hole diameter with experiment shows good agreement; the simulation result is 2.157 cm and the experimental value 2.125 cm [52], an error of 1.5%.

The second example problem is the oblique impact of a depleted uranium, 0.75% titanium rod on a steel plate, an experiment described by Hertel [30]. The target thickness is 0.64 cm, and the projectile has a diameter of 0.767 cm and a length to diameter ratio of 10. The obliquity is 73.5 degrees; the projectile velocity is 1.21 km/s. The velocity of the plate is 0.217 km/s. The model employed 240,958 particles. The material properties for this example are in Table 3.3 and the simulation parameters are in Table 3.4.

The meshes for the projectile and the target are shown in Figure 3.9. The rod projectile mesh has a minimum edge ratio of 1.0 and a maximum edge ratio of 1.53; the volume ratio is 6.1. The target plate has a graded mesh with aspect ratios of 1.5:1.5:1.0 for the elements at the center and 3.0:3.0:1.0 for the elements at the corners; the volume ratio is 4.0. The mesh quality (measured using the maximum aspect ratio) for the target is shown in Figure 3.10 and for the projectile in Figure 3.11.

Figure 3.12 shows the initial configuration for this example problem. The physical time for this simulation is 150 microseconds; the simulation results at this time are shown in Figures 3.13 (front view) and 3.15 (back view). The intact element plots at 150 microseconds are shown in Figures 3.14 (front view) and 3.16 (back view). The simulation results show good agreement for residual projectile length and residual projectile velocity. The simulation result for the residual length is 4.78 cm and the experimental value is 5.55 cm [30], an error of 13.8%. For the residual velocity the simulation result is 0.98 km/s and the experimental value is 1.07 km/s [30], an error of 8.0 %.

The third example models the impact of an aluminum cylinder projectile on an aluminum target plate, an experiment described in reference [59]. The projectile has a diameter of 4.36 cm, a length of 5.16 cm and a yaw of 1.44 degrees. The target thickness is 5.04 cm. The velocity of the projectile is 2.137 km/s while the target is free. The model has 254,544 particles. The material properties for this case are listed in Table 3.5 and the simulation parameters are in Table 3.6.

Figure 3.17 shows the target and projectile meshes. The cylindrical projectile mesh has a minimum edge ratio of 1.0 and a maximum edge ratio of 1.70, the volume ratio is 2.3. The target plate has a graded mesh with aspect ratios of 1.5:1.5:1.0 for the elements at the center and 3.0:3.0:1.0 for the elements at the corners; the volume ratio is 4.0. Figures 3.18 and 3.19 show the mesh quality (measured using the maximum aspect ratio) for the target and the projectile respectively.

The initial configuration for this example problem is illustrated in Figure 3.20. The physical time for this simulation was 500 microseconds. Figures 3.21 (front view) and 3.23 (back view) show particle plots for this time. Intact element plots are illustrated in Figures 3.22 (front view) and 3.24 (back view). Comparison of the results of this simulation with the experimental results [59] are mixed. The hole diameter for the simulation is 10.4 cm; the experimental value is 9.80 cm, an error of 6.1%. The mass removed in the simulation is 1.47 kg; the experimental value is 1.81 kg, an error of 18.6%. Note that spall effects were not considered in the simulation.

Table 3.1: Material properties for aluminum sphere impact problem

Reference density (g/cc)	2.70
Reference speed of sound (cm/μsec)	0.524
Reference shear modulus (Mbar)	0.276
Reference yield stress (Mbar)	0.00276
Plastic failure strain	0.25
Plastic hardening exponent	0.10
Plastic hardening modulus	125
Maximum tensile strain	1.0
Specific heat (Mbar cm^3/ g K)	0.885e-5
Melt temperature (K)	1,220
Thermal softening modulus	1.0

Table 3.2: Simulation parameters for aluminum sphere impact problem

Projectile diameter (cm)	1.00
Projectile velocity (km/s)	6.7
Plate thickness (cm)	0.25
Number of particles	162,380
Simulation time (μsec)	25
Wall clock time (hrs)	7.77
Number of proccesors	64

Table 3.3: Material properties for uranium alloy rod impact problem

Property	Projectile	Target
Reference density (g/cc)	18.62	7.81
Reference speed of sound (cm/μsec)	0.2567	0.4578
Reference shear modulus (Mbar)	0.740	0.801
Reference yield stress (Mbar)	0.0095	0.0120
Plastic failure strain	0.25	0.10
Plastic hardening exponent	0.095	0.50
Plastic hardening modulus	1000	2
Maximum tensile strain	1.0	1.0
Specific heat (Mbar cm^3/ g K)	0.111e-5	0.448e-5
Melt temperature (K)	1,710	2,310
Thermal softening modulus	1.0	1.0

Table 3.4: Simulation parameters for uranium alloy rod impact problem

Projectile material	Uranium alloy
Projectile diameter (cm)	0.767
Projectile length (cm)	7.67
Projectile velocity (km/s)	1.21
Obliquity (deg)	73.5
Plate material	Steel
Plate thickness (cm)	0.64
Plate velocity (km/s)	0.217
Number of particles	240,958
Simulation time (μs)	150
Wall clock time (hrs)	13.58
Number of proccesors	64

Table 3.5: Material properties for cylinder impact problem

Reference density (g/cc)	2.70
Reference speed of sound (cm/μsec)	0.524
Reference shear modulus (Mbar)	0.276
Reference yield stress (Mbar)	0.00276
Plastic failure strain	0.25
Plastic hardening exponent	0.10
Plastic hardening modulus	125
Maximum tensile strain	1.0
Specific heat (Mbar cm^3/ g K)	0.885e-5
Melt temperature (K)	1,220
Thermal softening modulus	1.0

Table 3.6: Simulation parameters for cylinder impact problem

Projectile diameter (cm)	4.36
Projectile length (cm)	5.16
Projectile velocity (km/s)	2.137
Total yaw (deg)	1.44
Plate thickness (cm)	5.04
Number of particles	254,544
Simulation time (μs)	500
Wall clock time (hrs)	19.62
Number of proccesors	64
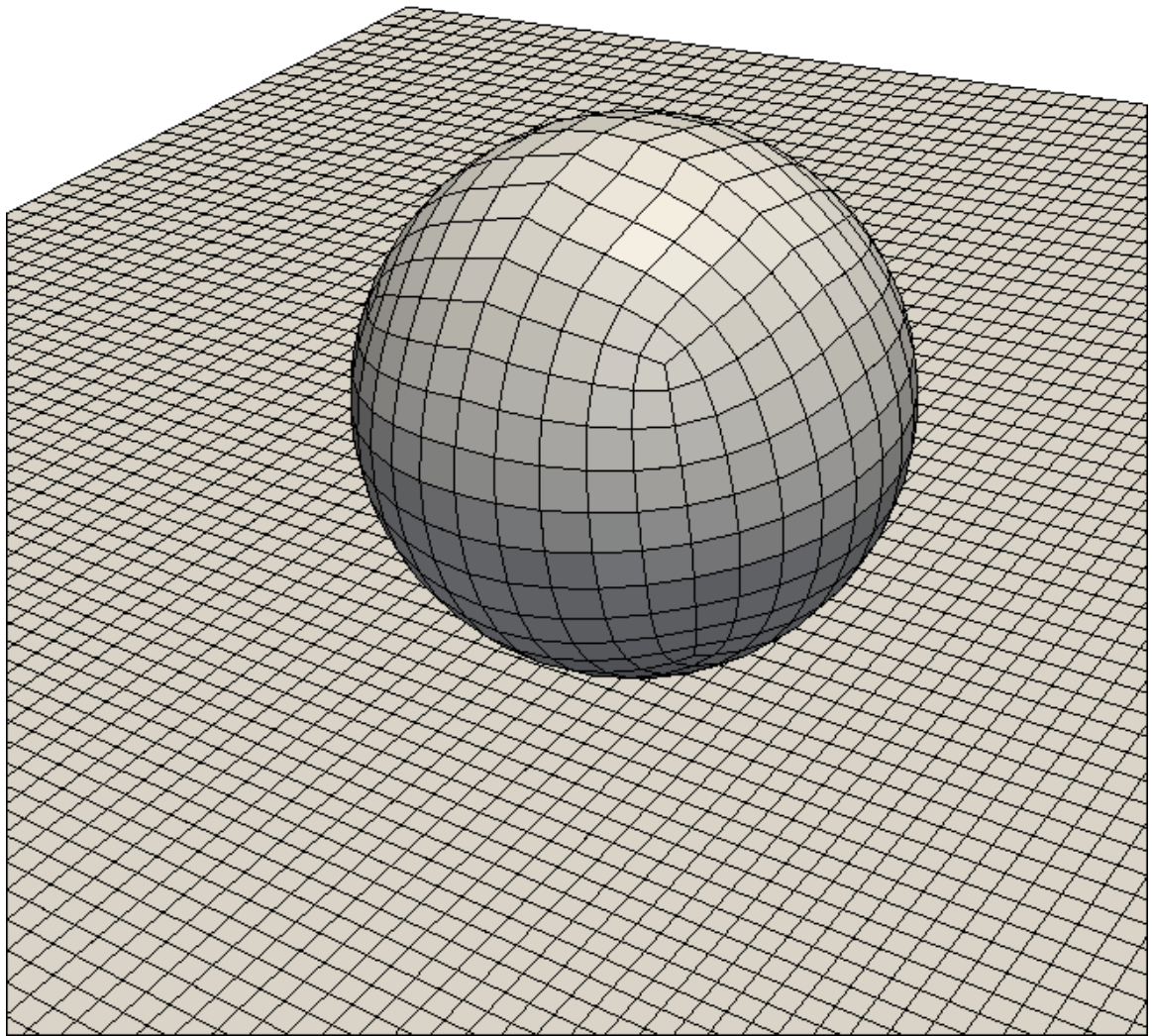
Figure 3.1: Aluminum sphere impact problem mesh.

Figure 3.2: Aluminum sphere impact problem, maximum aspect ratio for the target mesh.Blue and red colors indicate the zones with the lowest and highest aspect ratio respectively.

Figure 3.3: Aluminum sphere impact problem, maximum aspect ratio for the projectile mesh.Blue color indicates the zone with the lowest aspect ratio.

Figure 3.4: Aluminum sphere impact problem, element plot of the initial configuration.

Figure 3.5: Aluminum sphere impact problem, particle plot of the simulation results at 25 microseconds (front view).

Figure 3.6: Aluminum sphere impact problem, element plot of the simulation results at 25 microseconds (front view).

Figure 3.7: Aluminum sphere impact problem, particle plot of the simulation results at 25 microseconds (back view).

Figure 3.8: Aluminum sphere impact problem, element plot of the simulation results at 25 microseconds (back view).
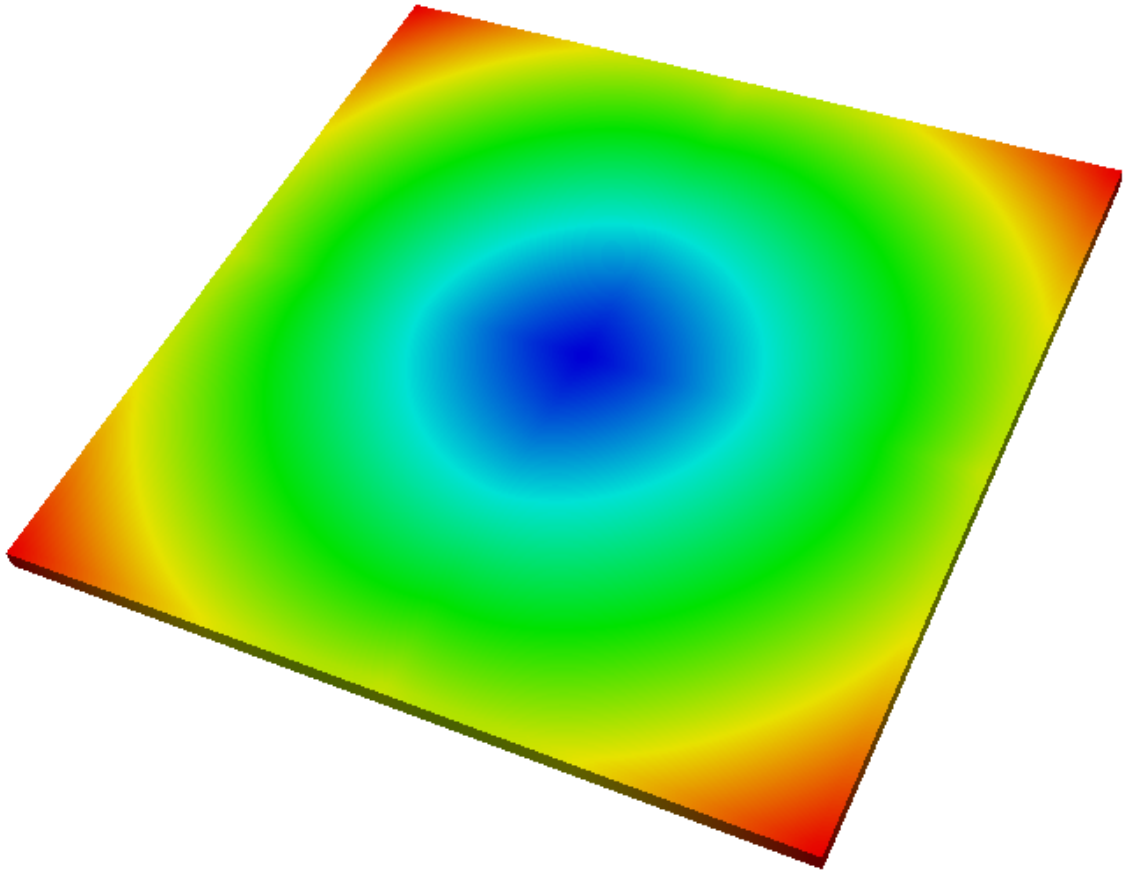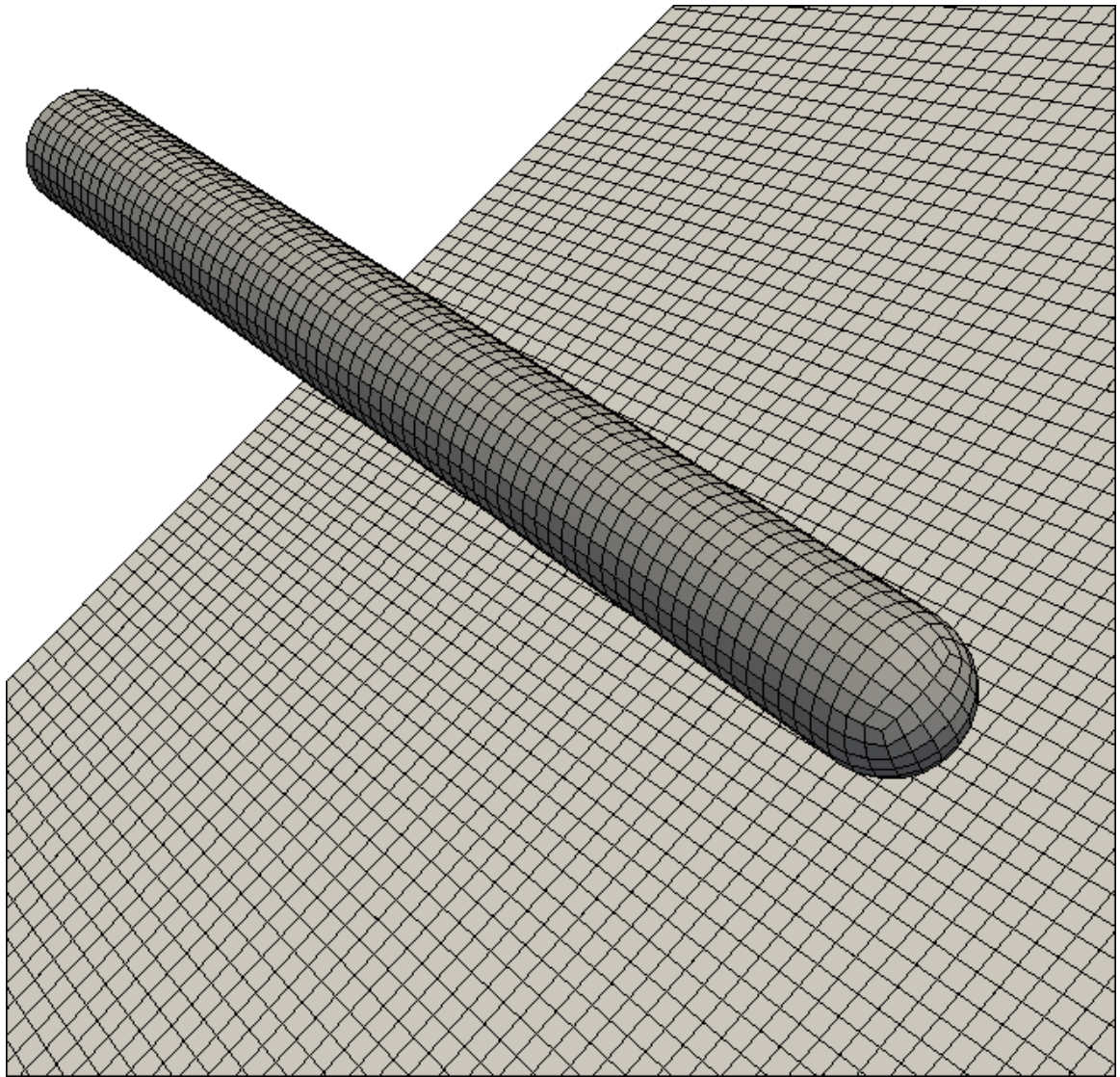
Figure 3.9: Uranium alloy rod impact problem mesh.
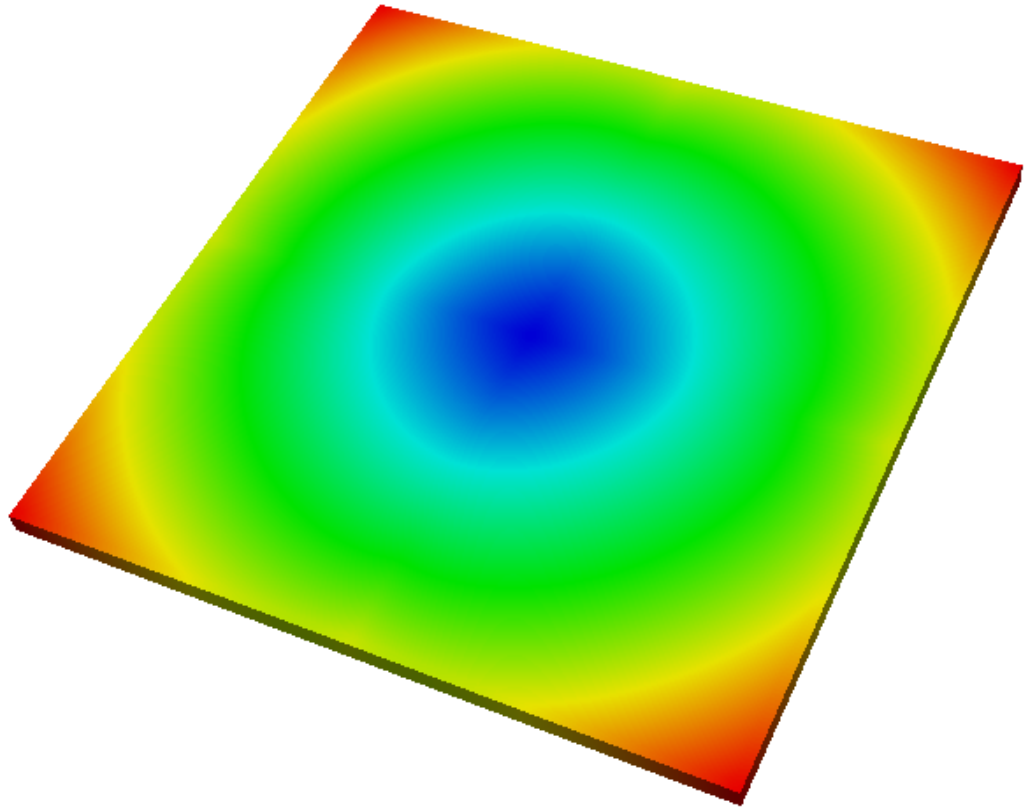
Figure 3.10: Uranium alloy rod impact problem, maximum aspect ratio for the target mesh.Blue and red colors indicate the zones with the lowest and highest aspect ratio respectively.
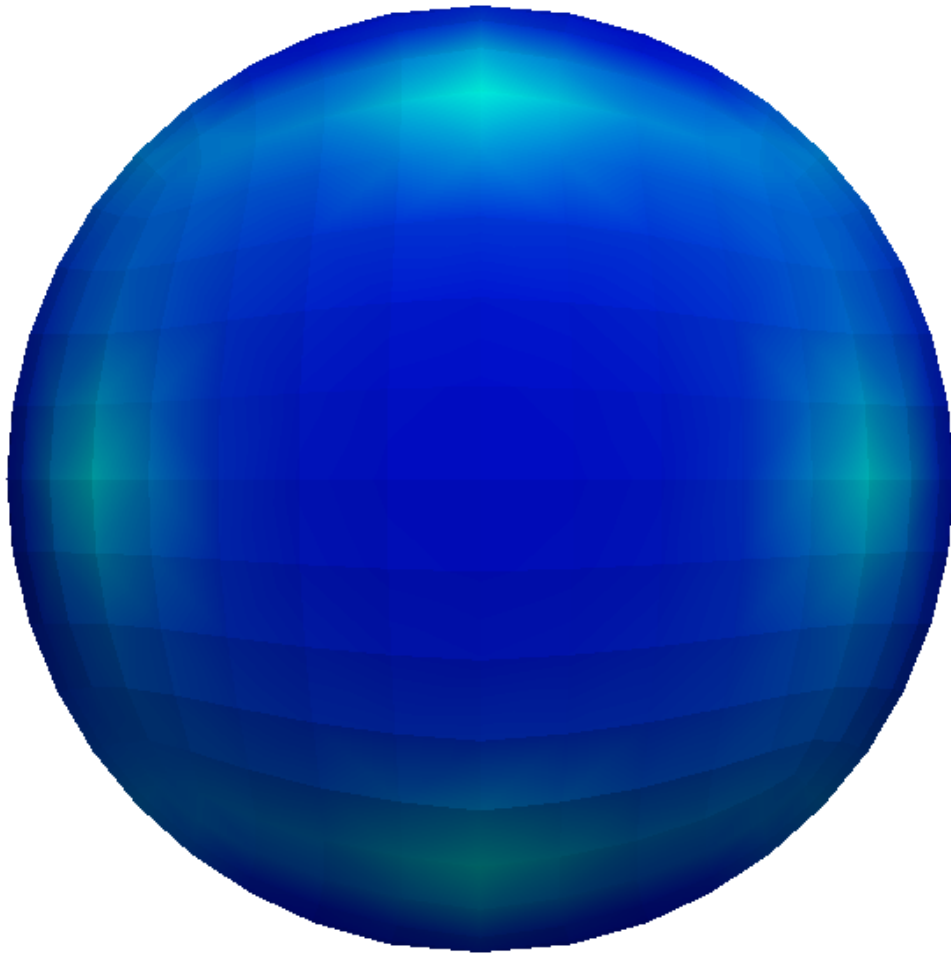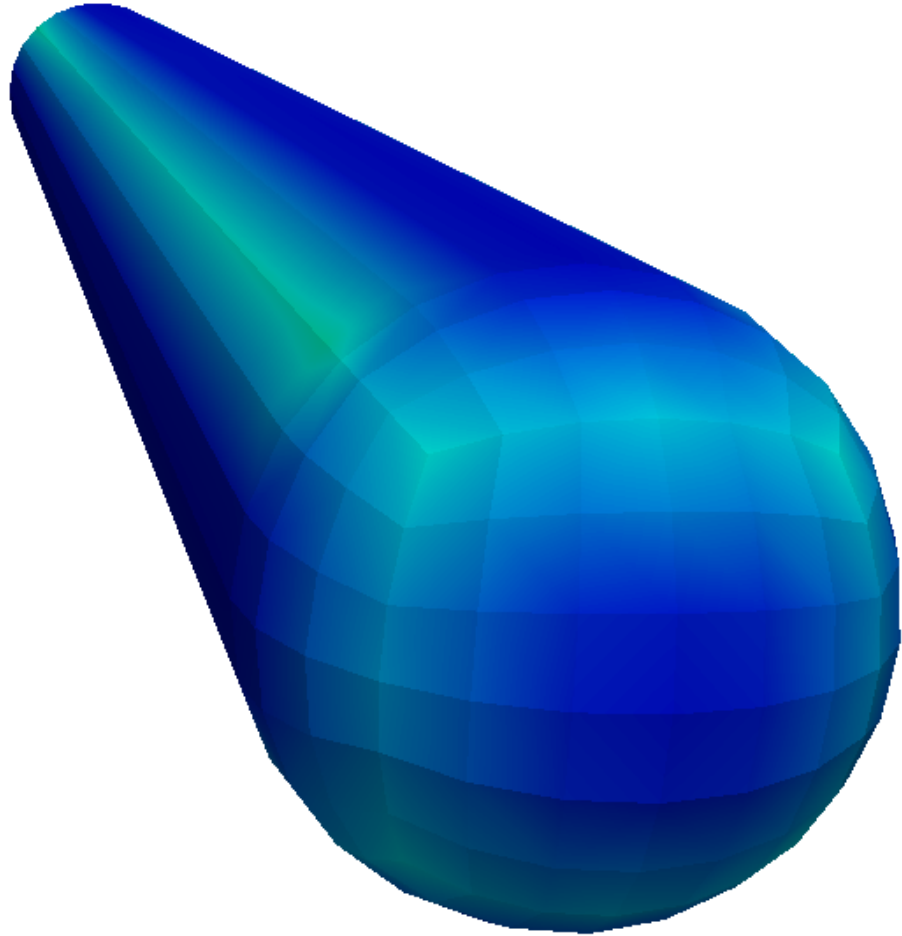
Figure 3.11: Uranium alloy rod impact problem, maximum aspect ratio for the projectile mesh.Blue color indicates the zones with the lowest aspect ratio.
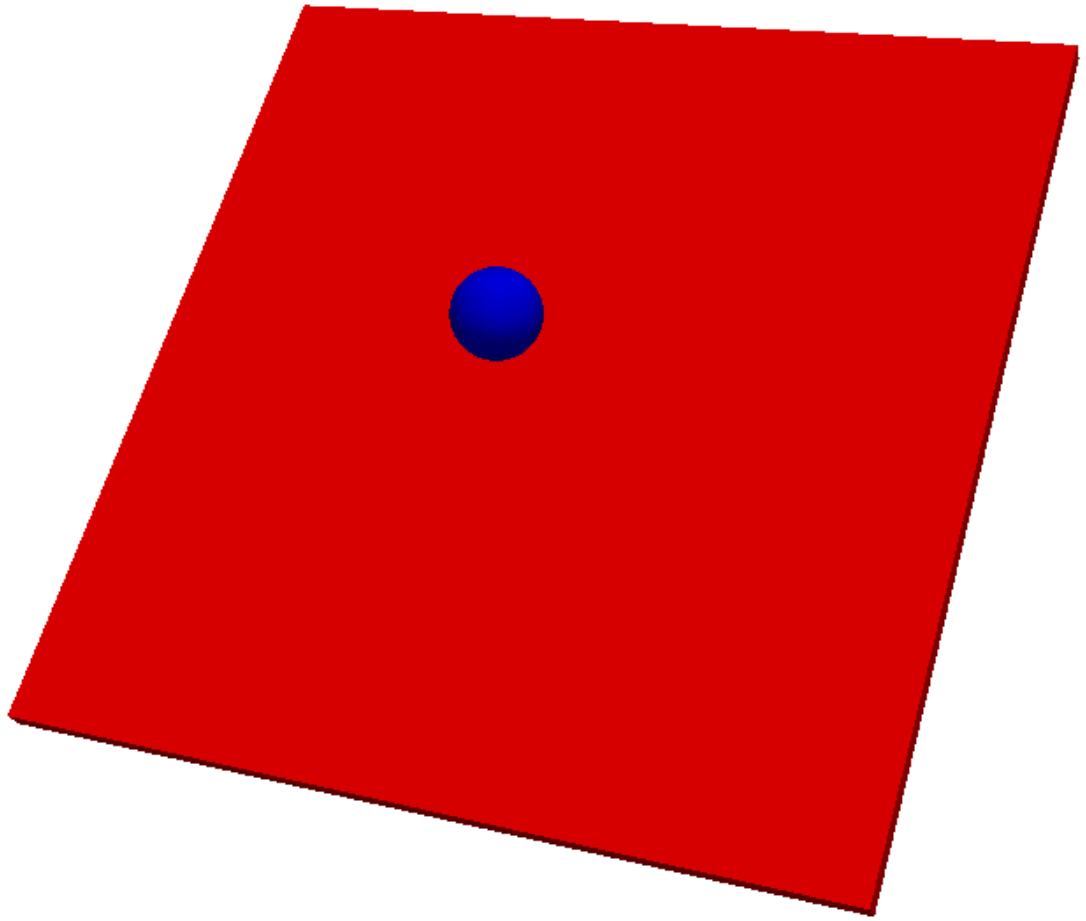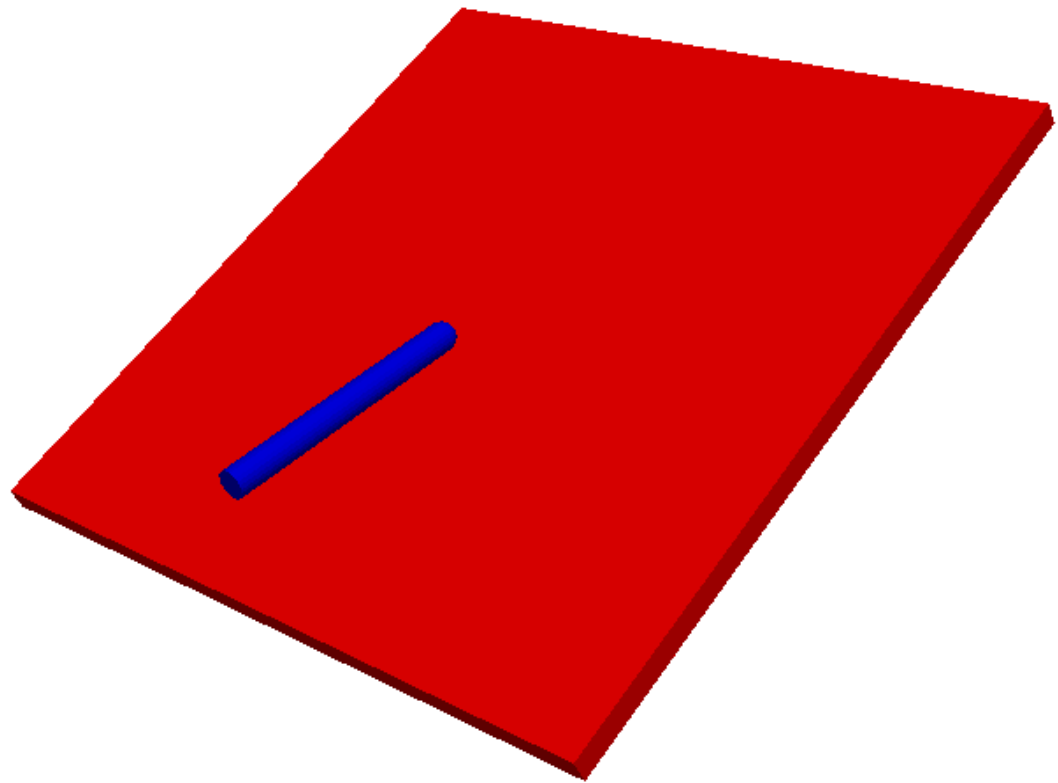
Figure 3.12: Uranium alloy rod impact problem, element plot of the initial configuration.
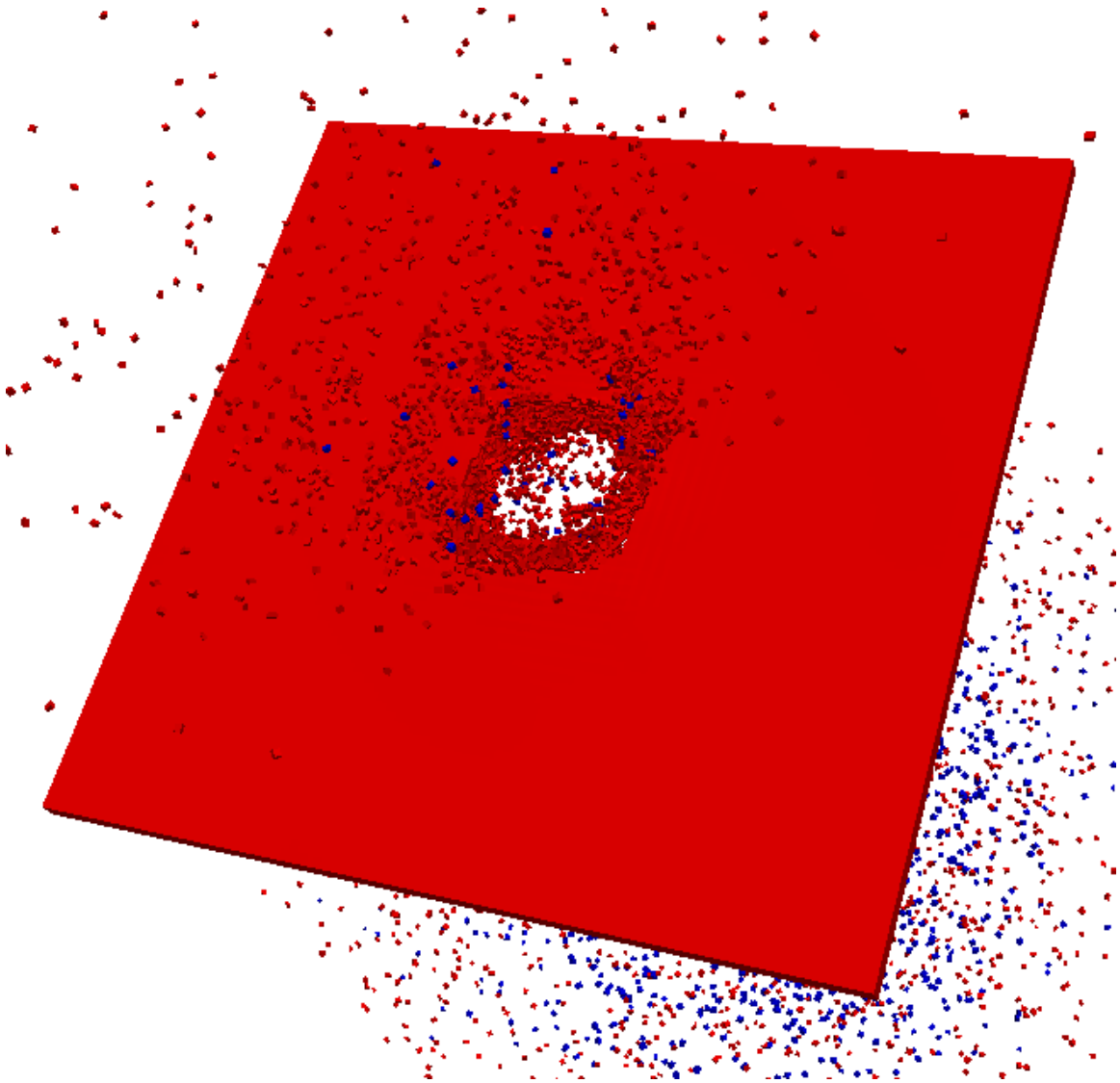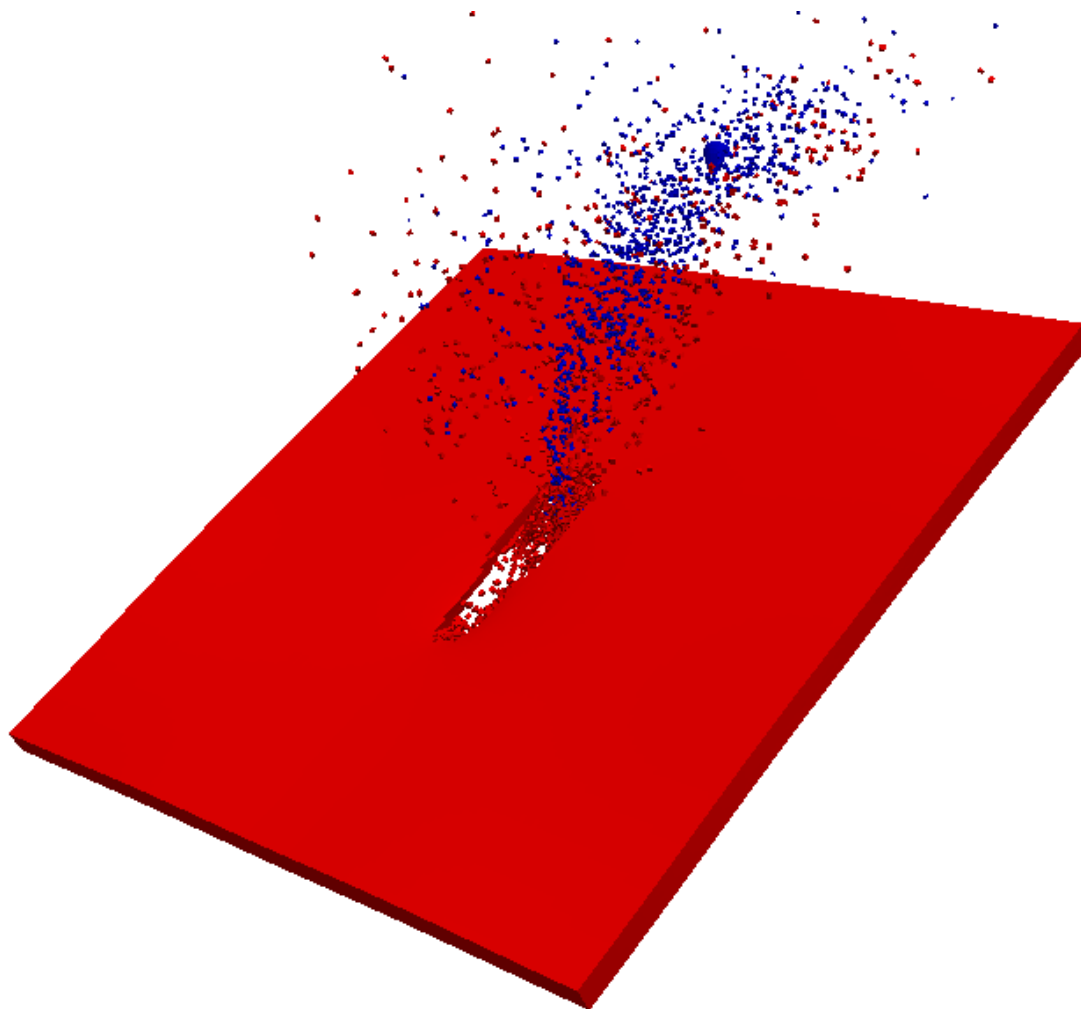
Figure 3.13: Uranium alloy rod impact problem, particle plot of the simulation results at 150 microseconds (front view).
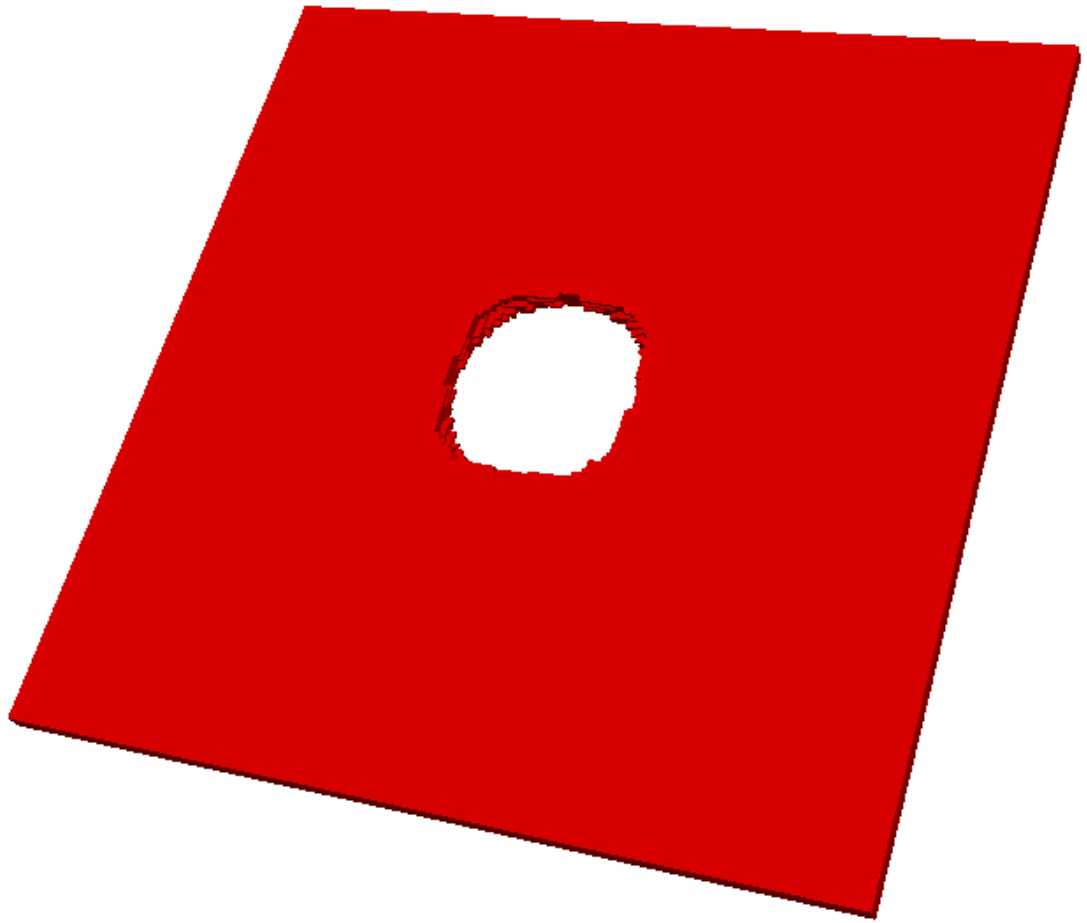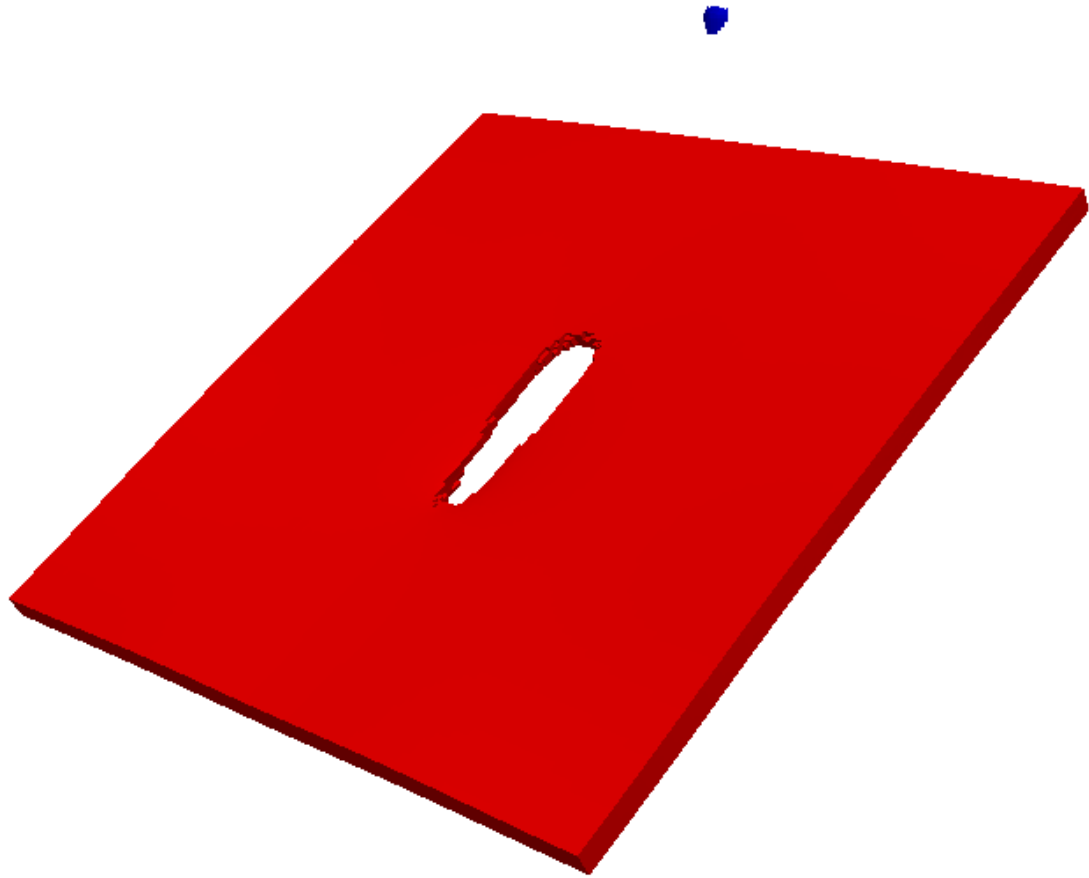
Figure 3.14: Uranium alloy rod impact problem, element plot of the simulation results at 150 microseconds (front view).
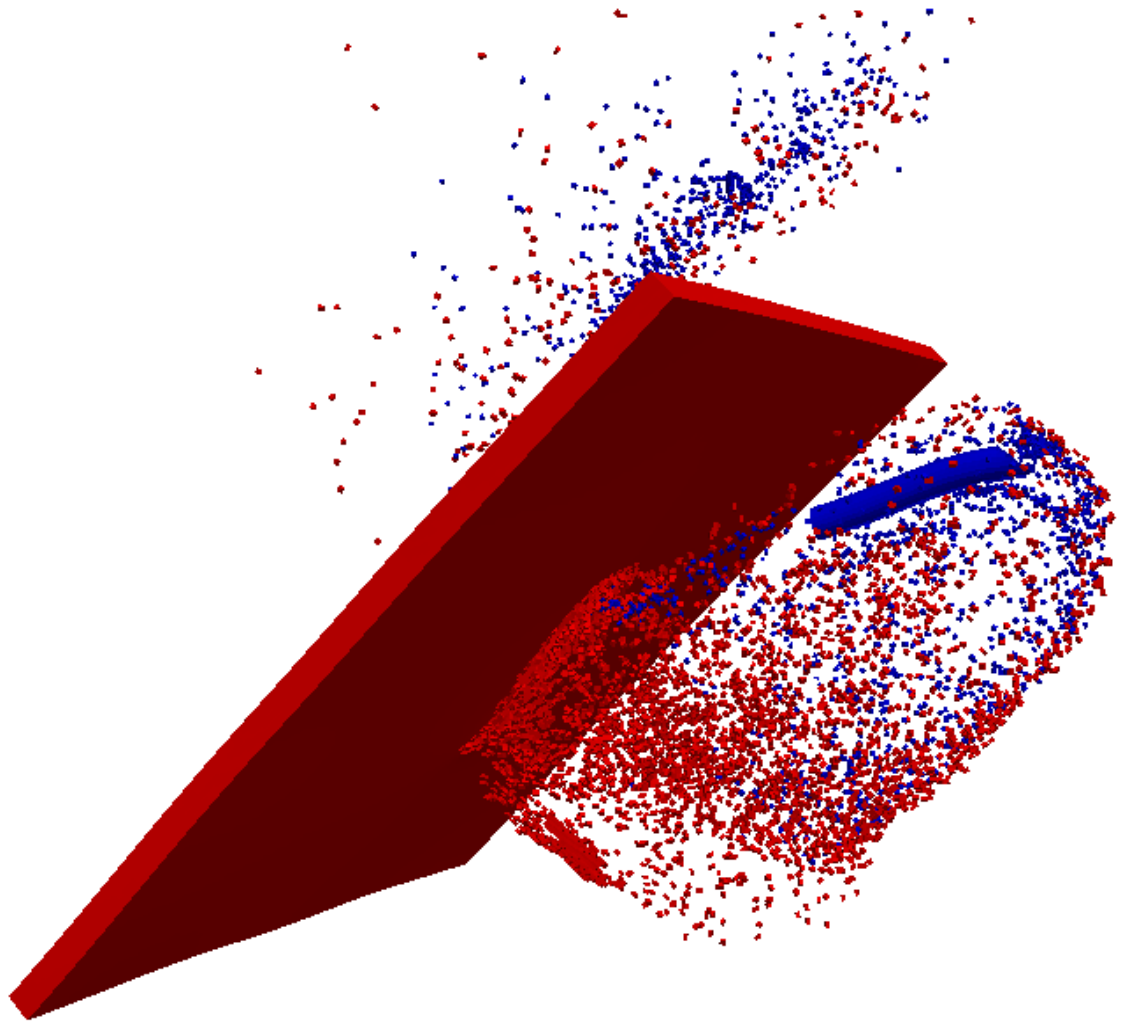
Figure 3.15: Uranium alloy rod impact problem, particle plot of the simulation results at 150 microseconds (back view).
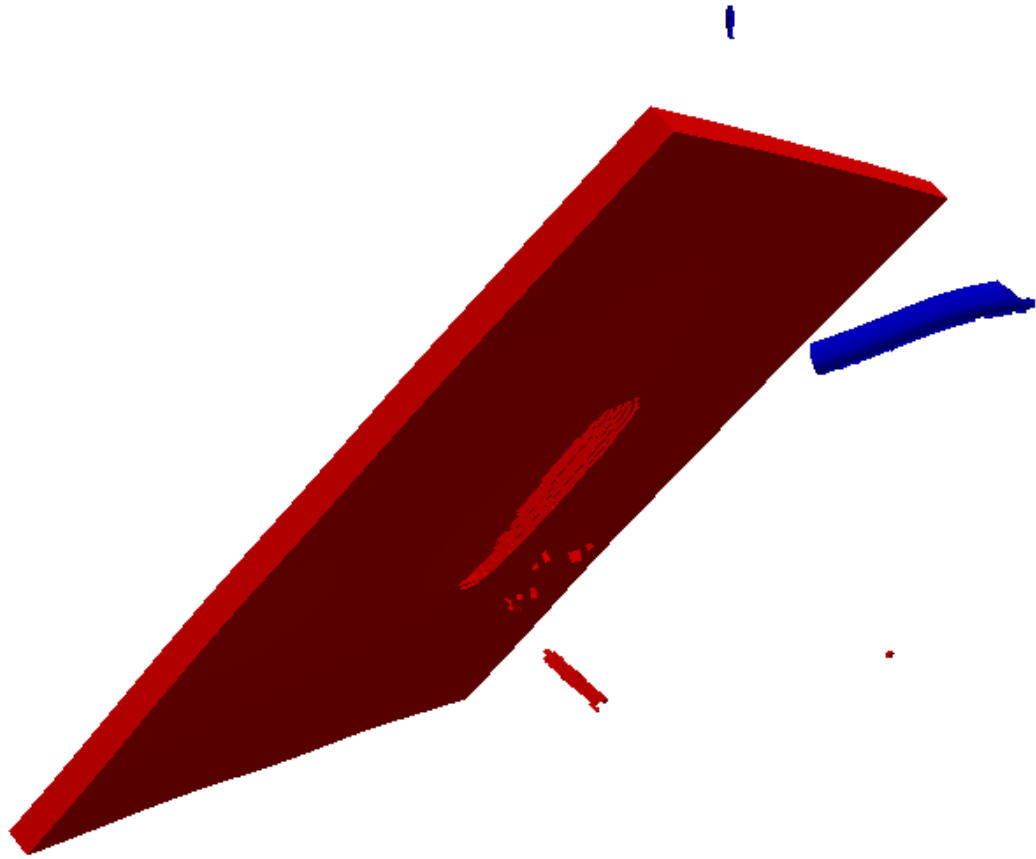
Figure 3.16: Uranium alloy rod impact problem, element plot of the simulation results at 150 microseconds (back view).
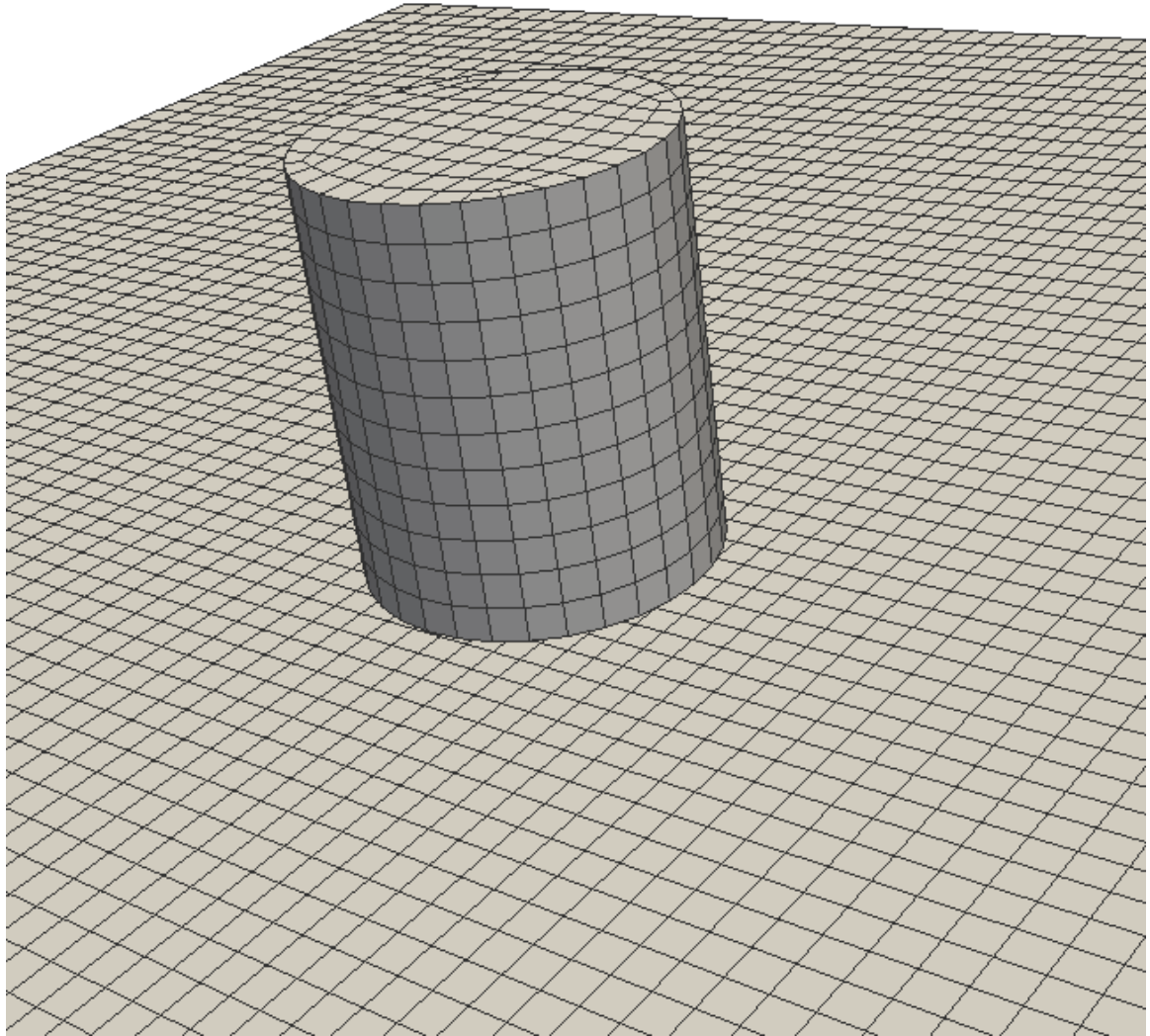
Figure 3.17: Cylinder impact problem mesh.
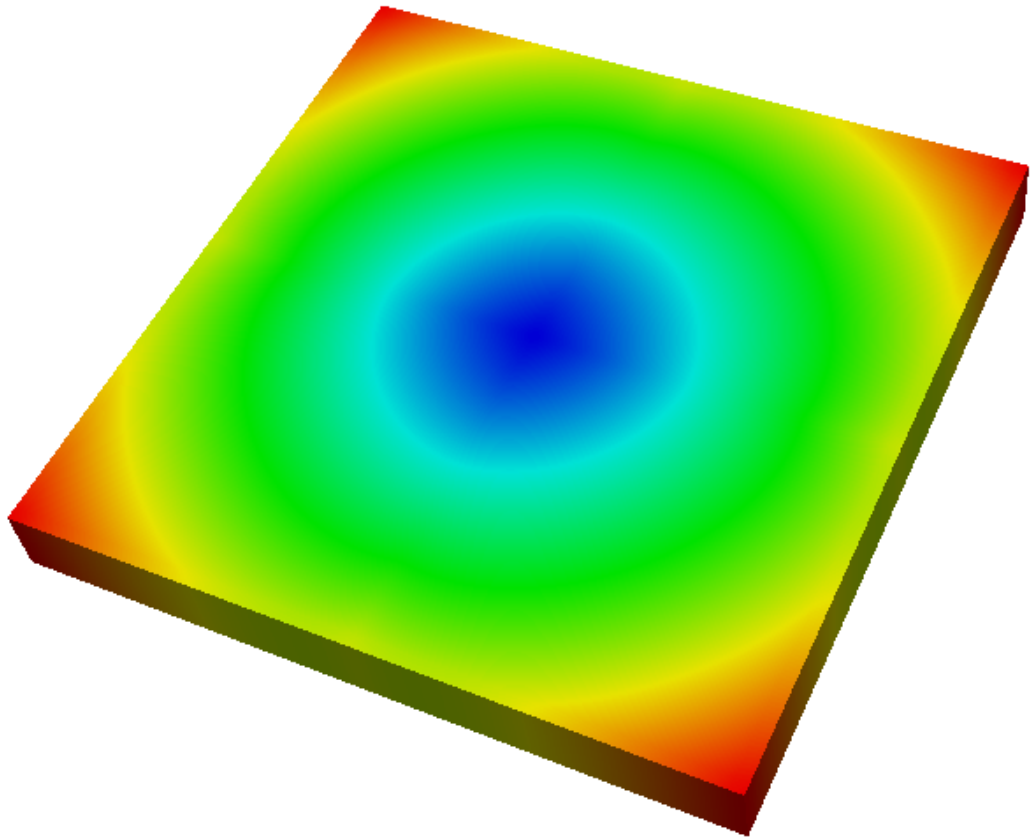
Figure 3.18: Cylinder impact problem, maximum aspect ratio for the target mesh.Blue and red colors indicate the zones with the lowest and highest aspect ratio respectively.
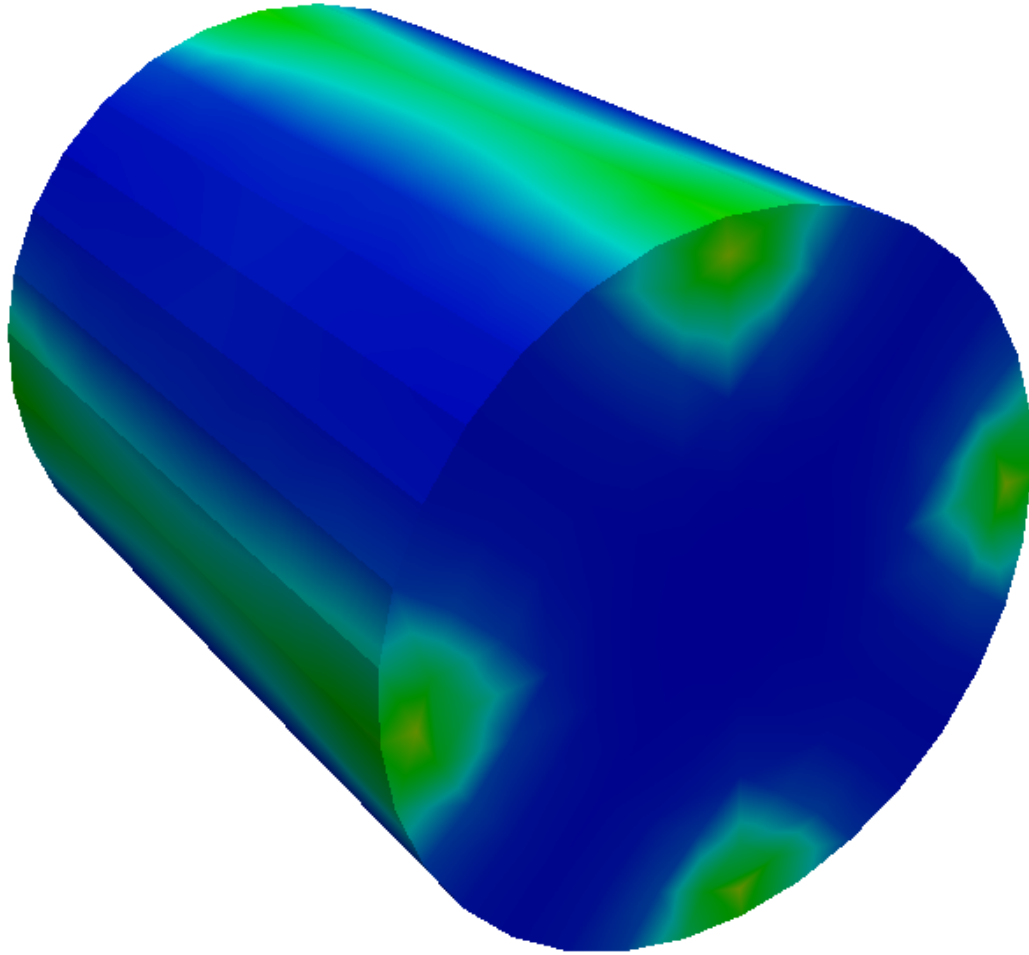
Figure 3.19: Cylinder impact problem, maximum aspect ratio for the projectile mesh.Blue color indicates the zones with the lowest aspect ratio.
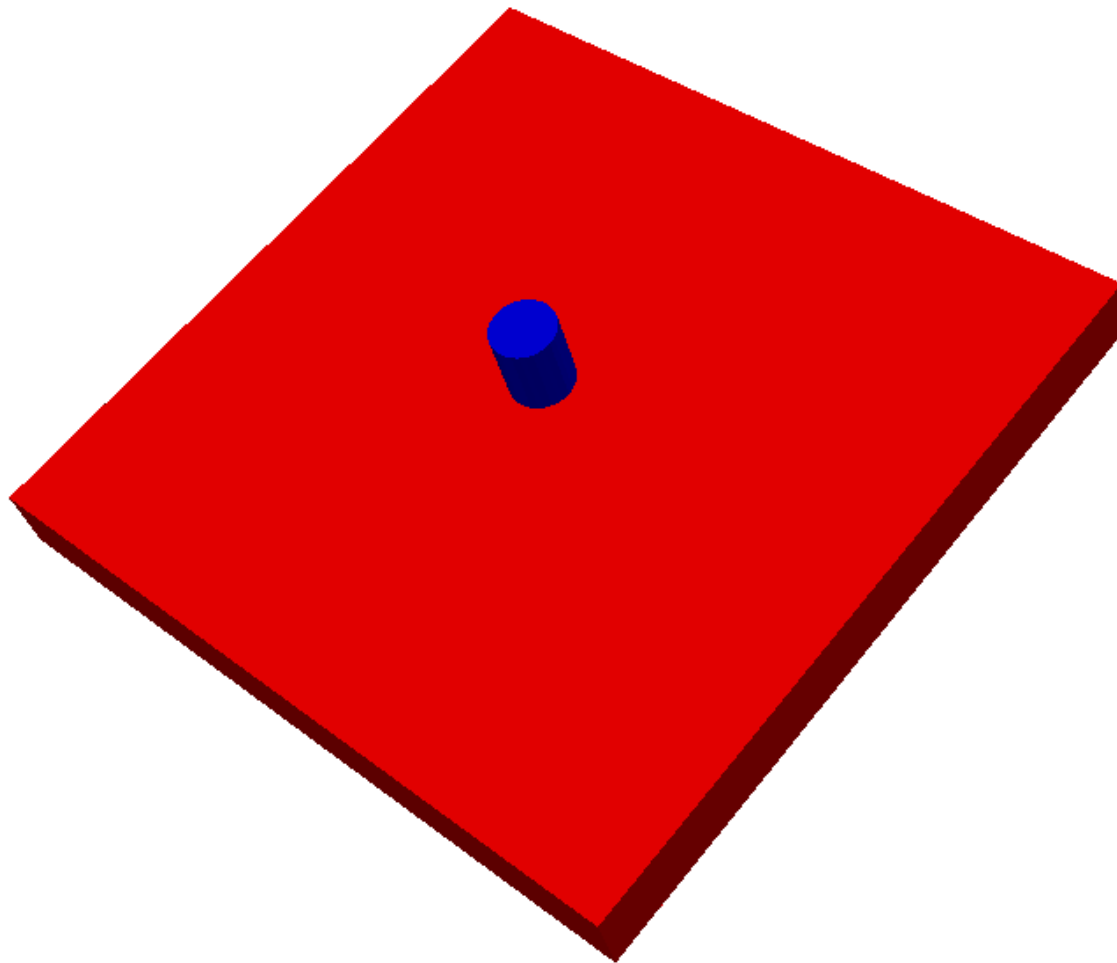
Figure 3.20: Cylinder impact problem, element plot of the initial configuration.
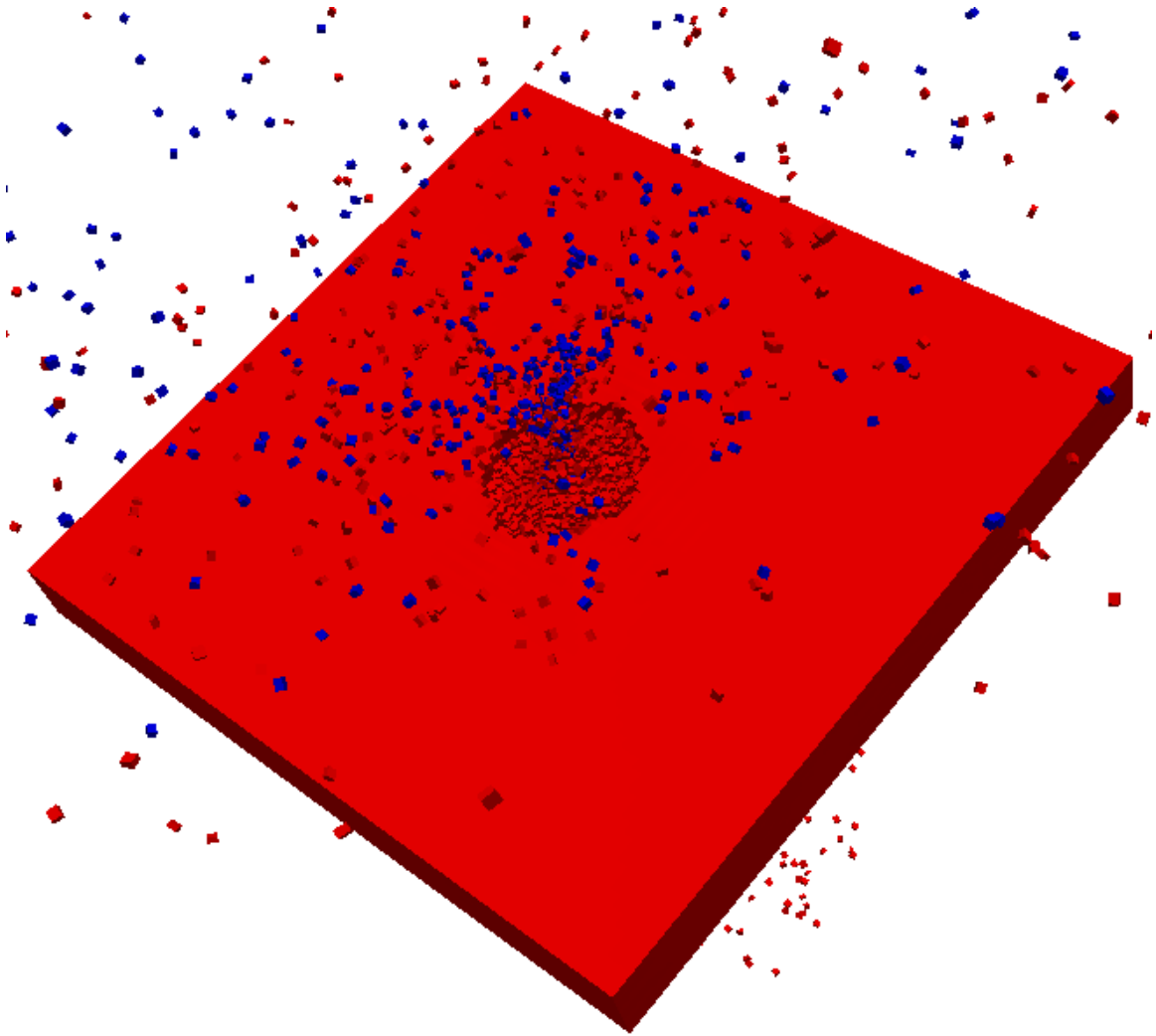
Figure 3.21: Cylinder impact problem, particle plot of the simulation results at 500 microseconds (front view).
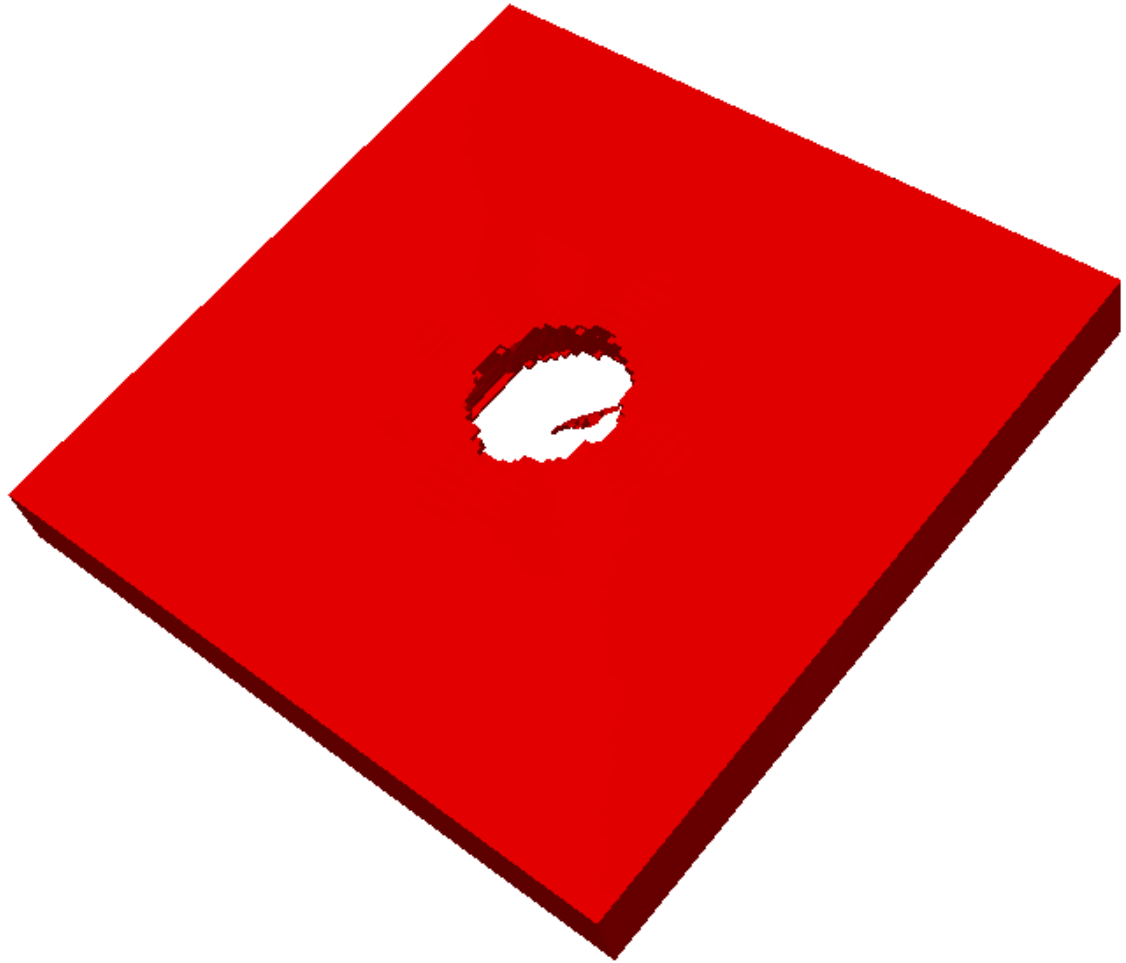
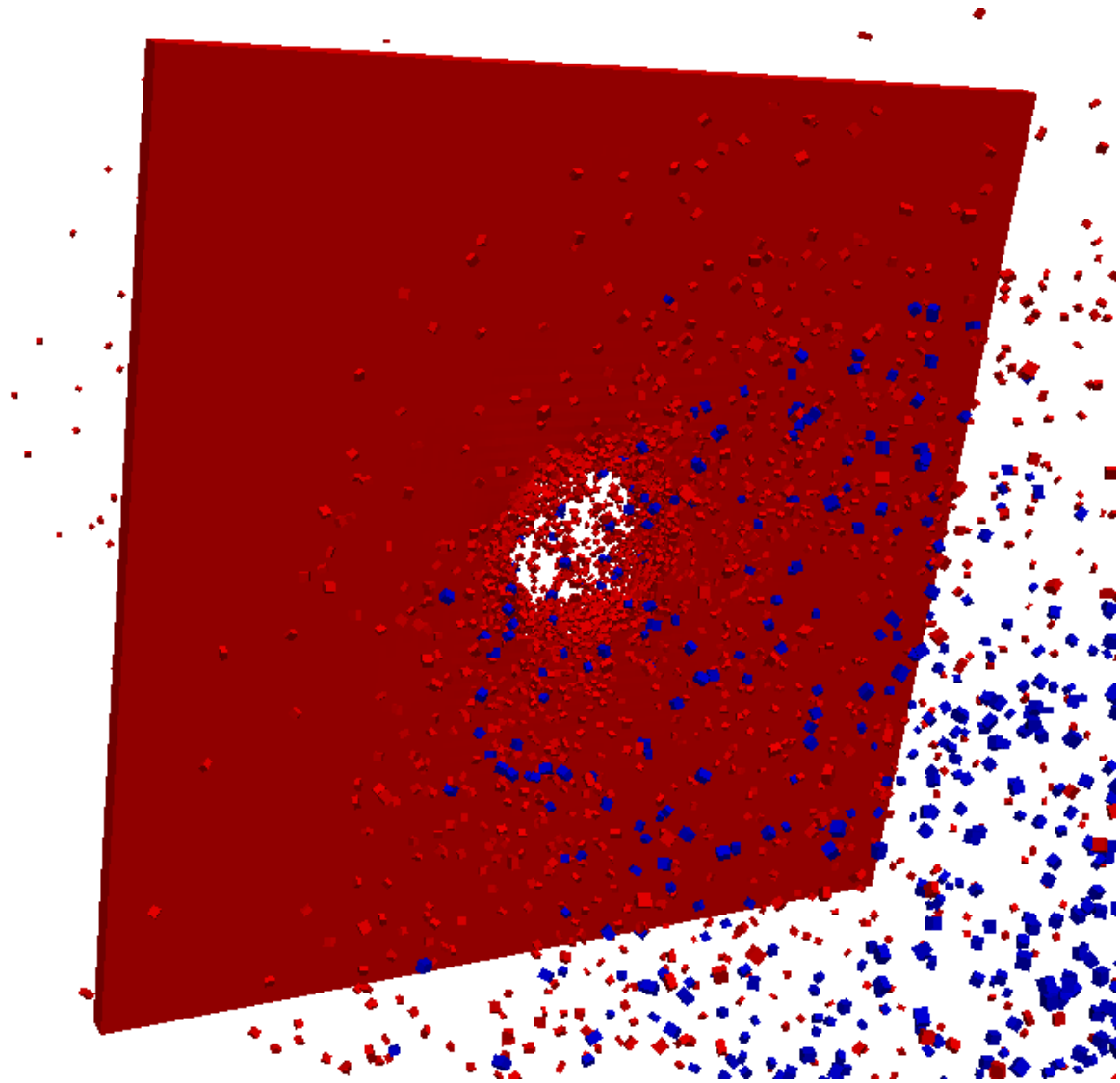Figure 3.22: Cylinder impact problem, element plot of the simulation results at 500 microseconds (front view).
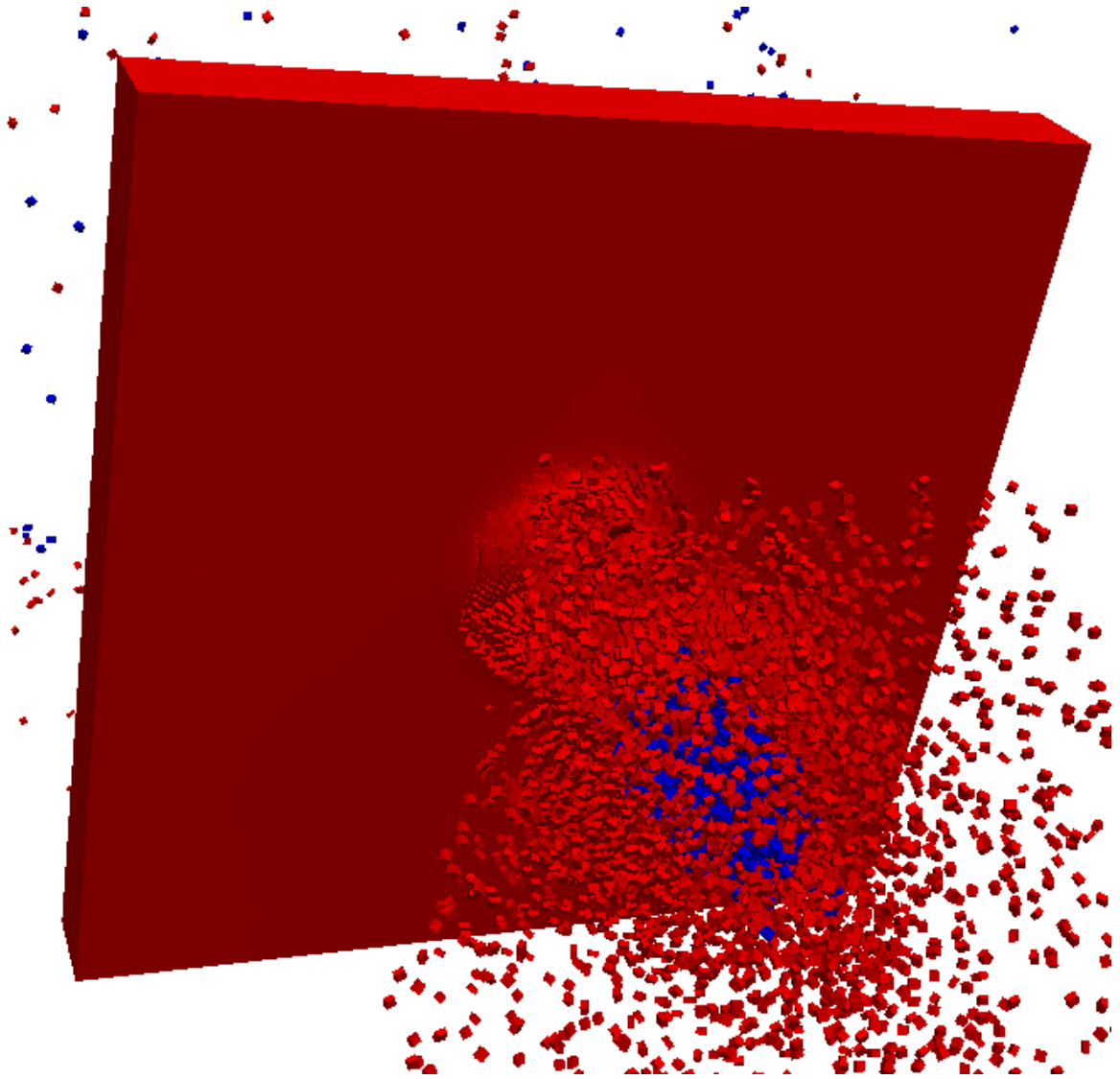
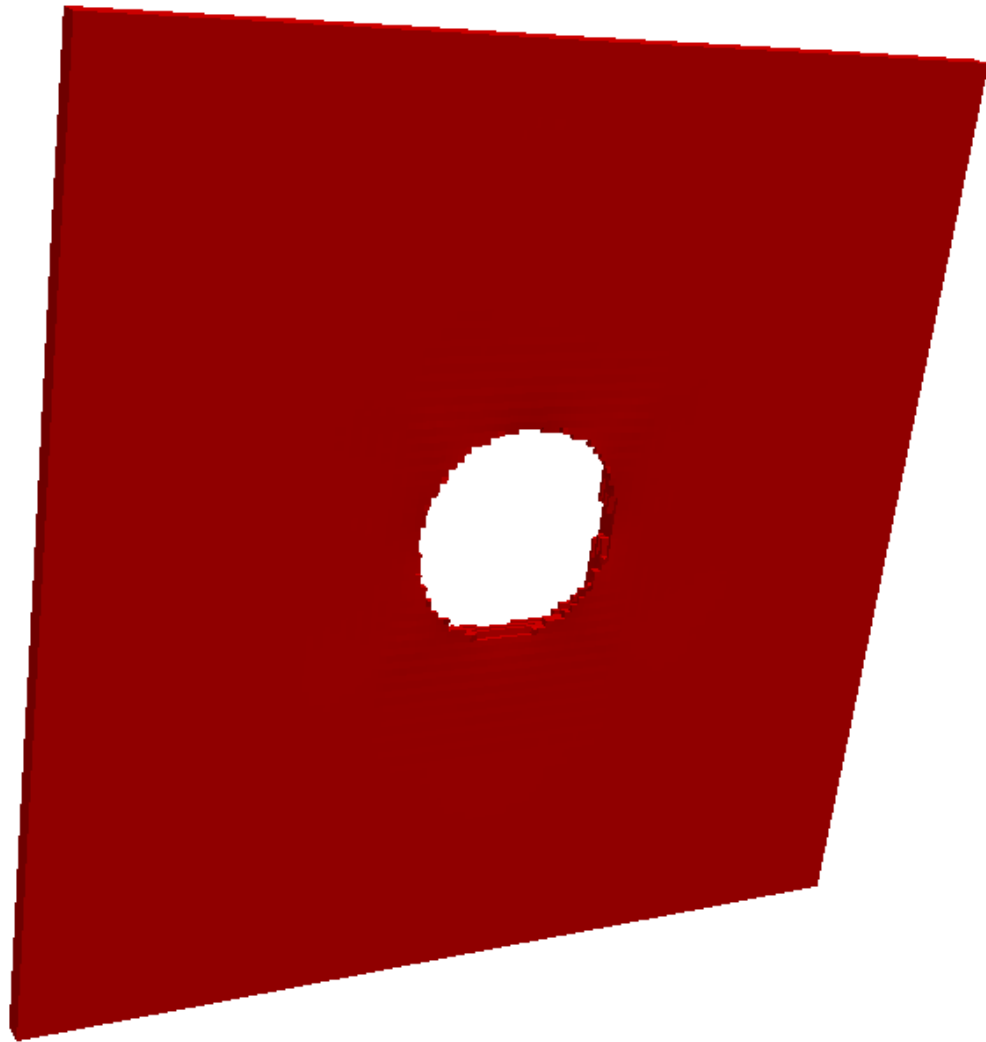Figure 3.23: Cylinder impact problem, particle plot of the simulation results at 500 microseconds (back view).
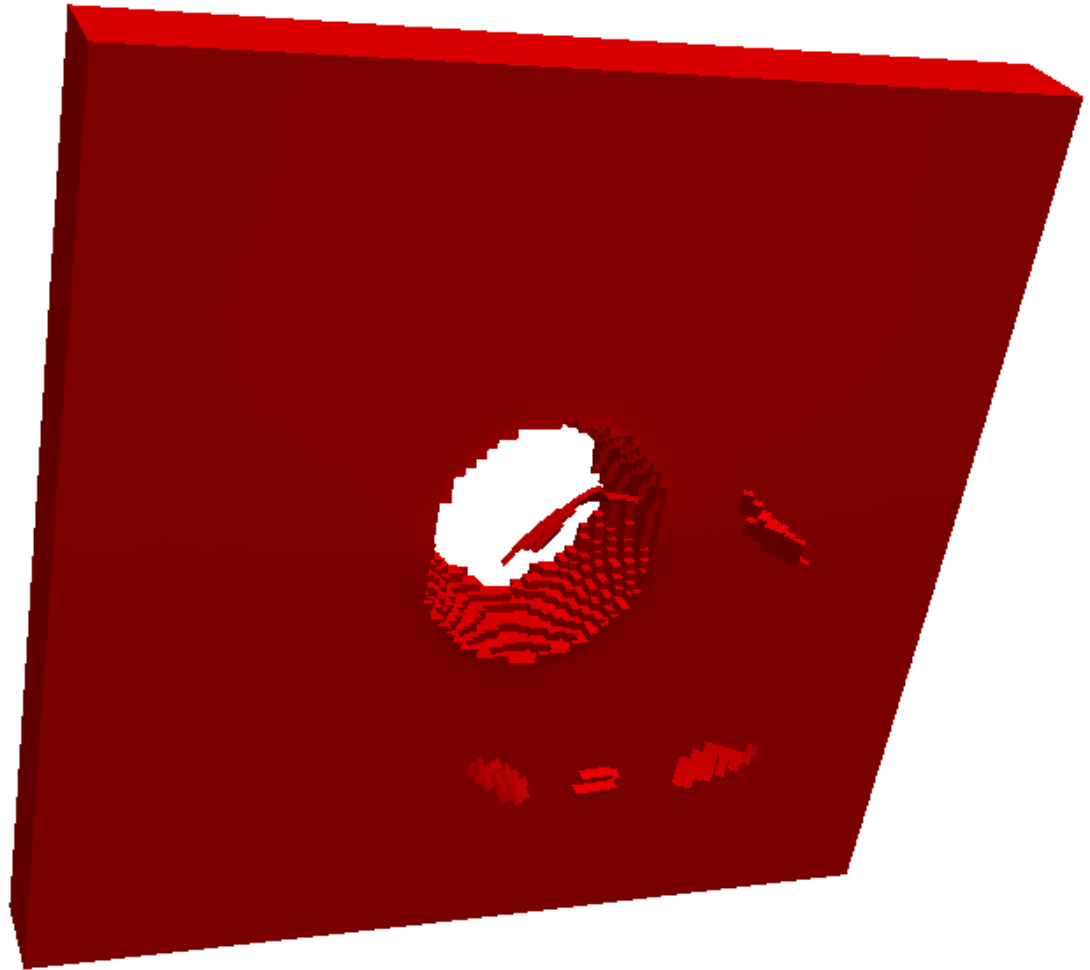
Figure 3.24: Cylinder impact problem, element plot of the simulation results at 500 microseconds (back view).

Chapter 4

Simulation of Orbital Debris Impact on the Space Shuttle Wing Leading Edge

4.1 Introduction

The debris environment in low earth orbit represents a significant hazard for manned spacecraft. The International Space Station (ISS) was designed with this environment in mind, and its habitable modules incorporate shielding for centimeter-size aluminum particles impacting at relative velocities of 5-15 km/s. The Space Shuttle, developed in the 1970's and subject to the severe design constraints of a reusable launch vehicle, is less well protected from debris impact effects. Fortunately the limited duration of shuttle flights and the orbiter's small cross section (as compared to ISS) mean that the probability of significant orbital debris impact damage is low. In addition, shuttle operating practices take careful account of the debris hazard. Vehicle orbit can be adjusted to give wide berth to objects detected on radar, and vehicle orientation is selected to minimize the exposure of vulnerable structural components to a high debris flux.

NASA closely monitors orbital debris impact effects on the shuttle fleet, since the vehicles are routinely damaged by very small particle impacts. In

addition NASA has performed hypervelocity impact tests [10] on critical components of the orbiter, to asses their vulnerability. However the current imitations of light gas gun technology and other hypervelocity testing techniques mean that experiments cannot be performed over the entire debris mass and velocity range of interest. Hence considerable attention has focused on the use of numerical simulation, as an adjunct to experiment, to estimate the effects of orbital debris impacts at velocities and kinetic energies outside the experimental range.

The recent loss of the shuttle Columbia [55], the result of launch debris impact, has highlighted long standing concerns over possible orbital debris impact damage to the spacecraft thermal protection system (TPS). Although both ceramic tile and reinforced carbon-carbon components of the TPS have been tested [13, 39] to quantify the effects of hypervelocity impact, the aforementioned limitations of current experimental methods motivate complementary numerical simulation work, to extrapolate the available experimental results into a higher velocity regime. The present chapter describes a series of simulations performed to study the effects of impact obliquity, projectile shape, and projectile orientation on hypervelocity impact damage to a critical component of the shuttle TPS. The simulations model impact effects on reinforced carbon-carbon, used to fabricate the orbiter wing leading edge, and include velocities and projectile shapes representative of the on-orbit debris environment but difficult or impossible to test in the laboratory. The results of the simulations are compared to the available experimental data base, and

scaling of the experimental and simulation data to describe other impact conditions is suggested. The analytical methodology applied here has application in other hypervelocity impact research where a purely experimental approach is impractical or where high material costs and long test article fabrication times suggest that a coordinated experimental and computational study is appropriate.

The present research extends the work of Park and Fahrenthold [51], who developed a new orthotropic elastic-plastic constitutive model for reinforced carbon-carbon (RCC), validated the model in simulations of published hypervelocity impact experiments, and applied the model to study RCC perforation at velocities as high as 13 km/s. In particular they quantified the dependence of RCC perforation diameter on projectile mass, for spherical projectiles at an impact obliquity of 45 degrees, and scaled the simulation results with normal impact momentum. The simulation work described here assumes a fixed projectile mass, but varies the impact obliquity, projectile shape, and projectile orientation in order to study impact conditions representative of on-orbit debris but not realized in published experiments.

As previously noted, the present work takes as a starting point the validated RCC material model of Park and Fahrenthold [51]. To provide appropriate context, the next section briefly outlines the latter work, and provides basic references on RCC properties, material testing, and composite material constitutive modeling employed in the development of the orthotropic elastic-plastic formulation. In addition, the next section briefly outlines the numerical

method applied in the present chapter, including recent improvements intro-
duced by Park and Fahrenthold [50]. Details on the RCC material model and
the improved numerical method not included here are provided in the last two
cited references as well as the dissertation of Park [49].

4.2 Numerical Method and Material Model

The simulations described in the present work employed the hybrid
particle-finite element method of Shivarama and Fahrenthold [56], along with
recent improvements in the method introduced by Park and Fahrenthold [50].
The improved formulation introduces density and internal energy as state vari-
ables, whose evolution is described by explicit first order rate equations, which
are nonholonomic constraints on the general thermomechanical Lagrange equa-
tion formulation. These changes improve the numerical method in three re-
spects: its algebraic form is simplified, its computational cost is reduced, and
it now directly admits equations of state in standard density-internal energy
form. The revised formulation avoids the introduction of any kernel functions,
for either the density or rate of dilatation. A penalty repulsion potential may
be used, to insure that no two particle centers of mass ever overlap; however,
numerical tests show that the stored energy associated with this repulsion po-
tential is negligible. As compared to the kernel based formulation of Shivarama
and Fahrenthold [56], computational costs are reduced by approximately one
third.

The simulations discussed in the sections which follow apply an or-

74

thotropic elastic-plastic constitutive model for reinforced carbon-carbon, developed and validated by Park and Fahrenthold [51]. The formulation is based on a general Lagrangian measure of the deviatoric strain and its additive decomposition into elastic and plastic parts. The finite strain kinematics account for all large deformation effects, including material reference frame dependence of the mechanical response. The elasticity model incorporates differences in elastic moduli in tension and compression. The non-associated plastic flow rule includes strain hardening, strain rate hardening, and thermal softening effects and an effective stress description of strength anisotropy. The general elastic-plastic formulation satisfies all first and second law thermodynamic constraints. This constitutive model is an extension of the formulation of Fahrenthold and Horban [21] to an orthotropic case commonly of interest for hypervelocity impact simulation in composite materials [1, 29]. Material properties used here were obtained from published experimental data [9], including recent experiments performed by Lu et al. [40] on RCC in support of the Columbia accident investigation. Some reference properties for the materials of interest in the present paper are provided in Table 4.1. References [51] and [49] include a complete listing of all material properties and a detailed description of the rate dependent anisotropic RCC model used in the simulations reported in this paper.

In addition to the aforementioned work directed at improving the hybrid particle-element method and the associated material modeling framework, its parallel implementation has been recently improved. In previous work

Fahrenthold and Shivarama [23] described an OpenMP [11] implementation and presented speedup data on its parallel performance. This parallel implementation has recently been extended, by introducing message passing routines which allow for execution on distributed memory systems. The current parallel implementation is hybrid OpenMP-MPI [48], which allows for shared memory parallelism on large nodes, with message passing between nodes. Alternately the implementation may be run in pure OpenMP mode on a single node or in pure MPI mode on clusters. Tables 4.2 and 4.3 provide speedup data for fixed size problems run on 1 to 16 processors in pure OpenMP mode and on 16 to 64 processors in hybrid OpenMP-MPI mode (in the latter case using 8-processor nodes). Experience to date indicates that the best performance is obtained by maximizing the use of shared memory. This result is not surprising, since particle methods must track a time varying neighbor set for each particle, and the computational cost of the associated message passing can be substantial.

4.3 Space Shuttle Wing Leading Edge

The Space Shuttle wing leading edge is constructed of silicon carbide coated carbon-carbon composite panels, nominally 0.63 cm in thickness, including coating layers 0.08 cm in thickness located on both exterior and interior panel surfaces. These panels are a critical component of the spacecraft thermal protection system, protecting the aluminum wing structure from the very high temperatures which develop at the wing leading edge during reentry. Although carbon-carbon maintains its strength at high temperatures,

76

it is subject to oxidation during re-entry. To prevent oxidation a silicon carbide coating is applied, and the resulting RCC composite offers a solution to a difficult thermal protection problem for reusable space vehicles.

Possible perforation of the RCC panels under orbital debris impact is clearly a concern, and has been studied by NASA in previous experiments. Christiansen and Friesen [13] and Lyons et al. [39] performed light gas experiments to investigate the hypervelocity impact response of RCC, and measured perforation diameters and the extent of coating spall for a number of different projectile masses and impact obliquities, for spherical projectiles at velocities below 8 km/s. The extent of coating spall is of interest, since carbon-carbon material exposed by coating spallation is subject to oxidation under re-entry conditions, as demonstrated in experiments performed by Curry et al. [15]. The simulation work discussed here is focused on the potential vehicle failure mode just outlined, in particular predicting the size of RCC perforations and the extent of coating spall for orbital debris impact problems which cannot be studied experimentally. Hence all of the impact simulations described here involved combinations of projectile mass, velocity, and obliquity expected to perforate an RCC panel with the aforementioned nominal dimensions. Lesser impact-induced damage, such as spall or delamination without perforation, is also of interest but is not considered in the present paper. In all of the simulations discussed in the present paper, eccentricity of the modeled perforations and spalled regions and differences between the front and back surface target damage were modest; hence the sections which follow describe impact damage

77

in terms of average diameters. In the case of near-ballistic-limit impacts, delamination without perforation, or other complex impact problems, accurately quantifying the simulation results will likely be much more difficult.

4.4 Disc Impact Simulations

The first set of simulations assumed a disc shaped aluminum projectile with a diameter of 0.628 cm, a mass of 0.35 g, and a length-to-diameter ratio of 2/3. The modest deviation from a spherical geometry allows for an approximate comparison of the simulation results with light gas gun data for spherical projectiles at 7 km/s. Simulations were performed for three different impact velocities (7, 10, and 13 km/s) and four different impact obliquities (15, 45, 60, and 75 degrees, with zero degrees a normal impact). Figures 4.1 through 4.4 show simulation results at an obliquity of 45 degrees and an impact velocity of 7 km/s, depicting perforation and coating spall similar to that observed in light gas gun experiments. Parameters of all the simulations are listed in Tables 4.4 and 4.5, including wall clock (WC) time required for execution on shared memory systems (IBM p655 and p690) and an Intel (Cray-Dell) cluster. In Table 4.4, the parameters W and Ne represent the width of the square target plate and the number of elements used to span the target plate thickness.

An initial set of simulations was performed at an impact obliquity of 45 degrees, for various mesh densities, in order to evaluate numerical convergence of the results. Figures 4.5 and 4.6 plot numerical convergence of the simulation results for average perforation diameter and average coating spall diameter

at three different impact velocities. The latter diameters were obtained by averaging results for the width of the perforation and width of the spalled region, measured parallel to and perpendicular to the shot line on projection plots of the simulation results. The data in Figure 4.5 show that the results for average perforation diameter are converged at Ne = 8, for which six elements span the carbon-carbon while only one element spans the coating. The data in Figure 4.6 indicate that converged results for the average coating spall diameter require a much finer mesh, with Ne = 24, for which three elements span the coating. Only the 7 km/s case was run at the highest mesh density (Ne = 32), since such simulations are quite expensive, requiring (see Table 4.5) approximately 53 wall clock days on 32 processors. In the case of the production calculations, a mesh density corresponding to Ne = 16 was selected, since computer resource requirements precluded extensive simulations at a mesh density sufficient to fully converge the results for coating spall. At Ne = 16 the simulation results provide a fully converged estimate of perforation diameters, however there is some convergence error for coating spall.

Figures 4.7 and 4.8 plot the results of the production calculations for perforation diameter and coating spall diameter, as a function of impact obliquity and impact velocity. At a given obliquity, the perforation and spall diameters increase with impact velocity, in an approximately linear fashion. Given the rate dependence and high temperature strength of carbon-carbon materials, this result is not unexpected. By contrast the dependence of perforation and spall diameter on impact obliquity is highly nonlinear, with the results

at 15 and 45 degree obliquities very close. This suggests a dependence of the damage on the normal component of impact velocity. In an attempt to scale the simulation results, and to provide an approximate comparison with experimental data for spherical projectiles, Figures 4.9 and 4.10 plot the variation of perforation diameter and spall diameter with normal impact momentum. Note that Christiansen and Friesen [13] have previously scaled experimental RCC impact data with normal impact momentum. In the case of the perforation data, Figure 4.9 shows that the simulations (disc projectile, L/D = 2/3) and the experiments (spherical projectile, references [13] and [39]) scale with normal impact momentum, overlapping in a significant portion of the momentum regime considered. In the case of the spall data, Figure 4.10 suggests that at impact velocities well above the ballistic limit, the simulations and experiments [13] again scale with normal impact momentum. In this case however the momentum overlap with the experimental data is limited. In summary, the preceding analysis offers a partial validation of the simulations and suggests that momentum scaling may be used to extrapolate experimental data outside the velocity regime currently accessible using light gas gun technology.

4.5 Plate Impact Simulations

It appears that all of the published experimental data on hypervelocity impact in RCC involves spherical projectiles. However much of the debris in low earth orbit is believed to have a flat plate geometry. A second series of simulations was therefore performed for flat plate projectiles, to investigate

projectile shape and orientation effects on impact damage to RCC. The simulations assumed a square plate projectile with a width to thickness ratio of 10.6 and a projectile mass (0.35 g) the same as the disc projectiles discussed in the last section. Velocities of 7, 10 and 13 km/s were again modeled, and all of the simulations assumed an impact obliquity of 45 degrees. Three different (orthogonal) projectile orientations were considered, here referred to as flat surface, long edge, and short edge impacts. In each case the velocity vector was aligned with a principal axis of the projectile. Figures 4.11 through 4.14 show a representative short edge impact at 13 km/s, depicting perforation and coating spall similar to that shown in the disc impact case. Table 4.6 lists the simulation parameters for all nine cases, run on 32 processors of an IBM p690 at the resolution level Ne = 16.

The simulation results are plotted in Figures 4.15 and 4.16, and show a near linear variation of perforation diameter and coating spall diameter with impact velocity, for a given projectile orientation. The short edge impacts are the most damaging, while the results for the flat surface and long edge impacts are similar. Table 4.7 compares the results of the short edge impact cases with those for a disc projectile of the same mass and impact obliquity, at all three velocities modeled in the present paper. The tabulated data is the ratio by which the perforation diameter and coating spall diameter increase due to a change in projectile shape from disc to flat plate, for the most damaging plate impact orientation. The projectile shape effect ranges from 8 to 17 percent, and is most pronounced at the lowest impact velocity. The modest increase in

damage is likely due to the fact that the simulations consider impact conditions well above the ballistic limit.

4.6   Conclusion

The present work has described a series of three dimensional hypervelocity impact simulations performed to investigate the effects of orbital debris impact on the Space Shuttle wing leading edge, including velocities outside the experimental range. It extends the work of Park and Fahrenthold [51], who developed and validated an orthotropic elastic-plastic model for reinforced carbon-carbon and applied it to study the effect of projectile mass on RCC impact damage. The simulations described here quantify the effects of impact obliquity, projectile shape, and projectile orientation on perforation diameter and spalled region diameter under impact conditions representative of the on-orbit environment. The computational cost of these simulations was found to be considerable. Consistent with previous experimental work [13], the simulation results suggest the use of momentum scaling to extrapolate the available experimental data base. They also indicate that projectile shape and orientation effects are modest in the case of flat plate impacts above the ballistic limit.

Several areas are suggested for future work. The simulations presented here employed the best material property data available to the author; however, the complex nature of the RCC material suggests that additional material property testing is needed, perhaps to provide tabulated equations of state for

use in the high velocity impact regime. Higher resolution models are needed for further study of coating spall effects, in particular for near ballistic limit impacts. Finally additional impact experiments are needed, at higher impact velocities, to validate proposed extrapolations outside the existing experimental data base. Inhibited shaped charge launchers [62] or multi-stage gas guns [12] may provide a means for validation of proposed extrapolations.

Table 4.1: Material properties

Material property	Aluminum	Silicon Carbide	Carbon-Carbon
Reference density (g/cc)	2.70	3.21	1.58
Reference speed of sound (cm/μsec)	0.539	0.829	0.191
Mie-Gruneisen gamma	1.97	0.95	0.24
Mie-Gruneisen slope	1.34	1.21	1.33
Reference shear modulus (Mbar)	0.271	0.240	0.0718
Reference yield stress (kbar)	2.90	0.771	0.771
Plastic failure strain	1.00	0.10	0.50

Table 4.2: OpenMP speedup for a 1.22 million particle test problem

Number of processors	Particles per processor (thousands)	Wall clock time (hours)	Speedup
1	1220	4.657	1.00
4	305	1.168	3.99
16	76	0.308	15.12

Table 4.3: Hybrid OpenMP-MPI speedup for a 0.85 million particle test case

Number of processors	Particles per processor (thousands)	Wall clock time (hours)	Relative efficiency
16	53.1	0.598	1.000
32	26.6	0.360	0.831
64	13.3	0.264	0.566

Table 4.4: Simulation parameters for the disc impact problems

Velocity (km/s)	Obliquity (deg)	W (cm)	N_e	Particles (millions)
7	45	10	8	0.078
7	45	10	16	0.573
7	45	10	24	1.861
7	45	10	32	4.359
10	45	12	8	0.113
10	45	12	16	0.821
10	45	12	24	2.679
13	45	14	8	0.152
13	45	14	16	1.114
13	45	14	24	3.646
7	15	12	16	0.821
10	15	14	16	1.114
13	15	16	16	1.465
7	60	12	16	0.821
10	60	12	16	0.821
13	60	12	16	0.821
7	75	12	16	0.821
10	75	12	16	0.821
13	75	12	16	0.821

Table 4.5: Computational cost for the disc impact problems

Velocity (km/s)	Obliquity (deg)	System	Processors	WC Time (hours)
7	45	Cray-Dell cluster	8	46
7	45	IBM p690	32	189
7	45	IBM p690	32	371
7	45	IBM p690	32	1279
10	45	IBM p655	8	54
10	45	IBM p690	32	145
10	45	IBM p690	32	619
13	45	IBM p655	16	53
13	45	IBM p690	32	219
13	45	IBM p690	32	965
7	15	Cray-Dell cluster	32	305
10	15	IBM p690	32	159
13	15	IBM p690	32	230
7	60	IBM p690	32	99
10	60	IBM p690	32	151
13	60	IBM p690	32	172
7	75	Cray-Dell cluster	32	310
10	75	Cray-Dell cluster	32	365
13	75	Cray-Dell cluster	32	386

Table 4.6: Simulation parameters for the plate impact problems

Velocity (km/s)	Orientation of projectile	W (cm)	Particles (millions)	WC Time (hours)
7	flat surface	12	0.820	93
7	long edge	12	0.820	112
7	short edge	12	0.820	91
10	flat surface	14	1.113	146
10	long edge	14	1.113	172
10	short edge	14	1.113	150
13	flat surface	16	1.464	216
13	long edge	16	1.464	263
13	Short edge	16	1.464	236

Table 4.7: Comparison of impact damage due to disc and flat plate projectiles

Velocity (km/s)	Ratio of perforation diameters(plate to disc)	Ratio of spalled region diameters(plate to disc)
7	1.14	1.17
10	1.12	1.11
13	1.08	1.11
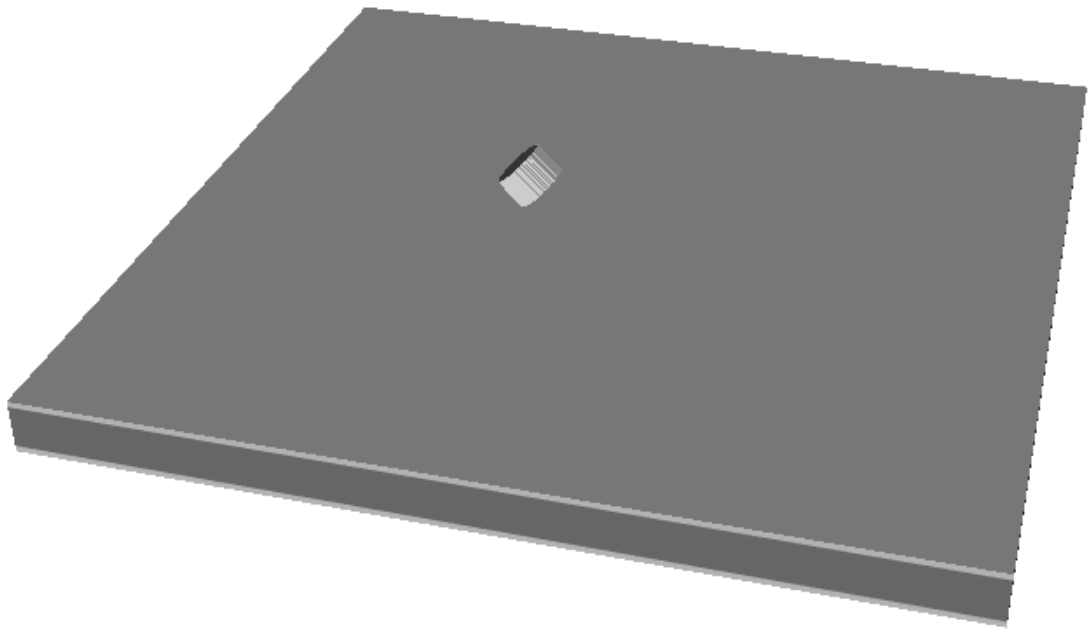
Figure 4.1: Initial configuration, disc impact simulation.
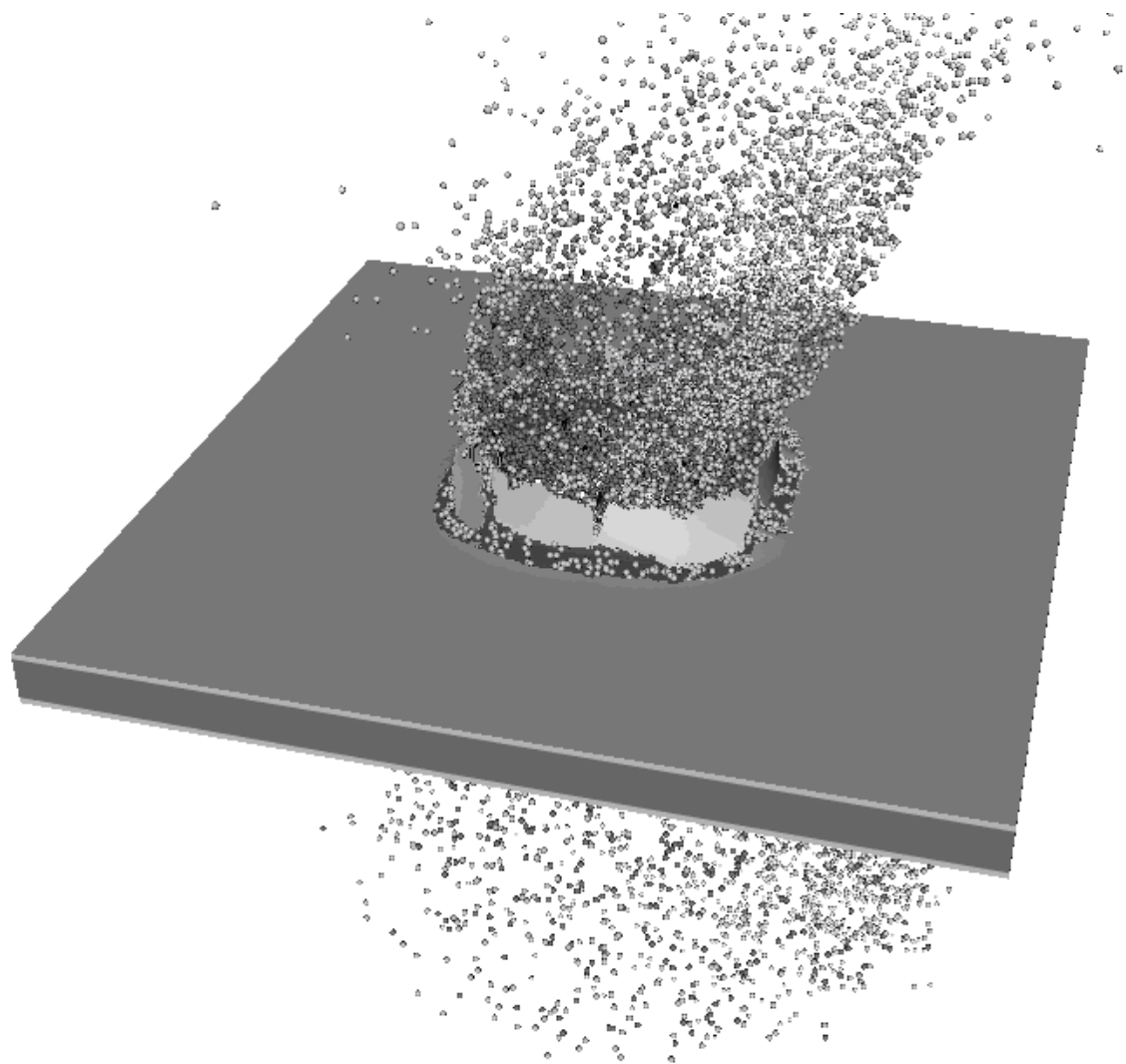
Figure 4.2: Disc impact simulation at 50 microseconds.
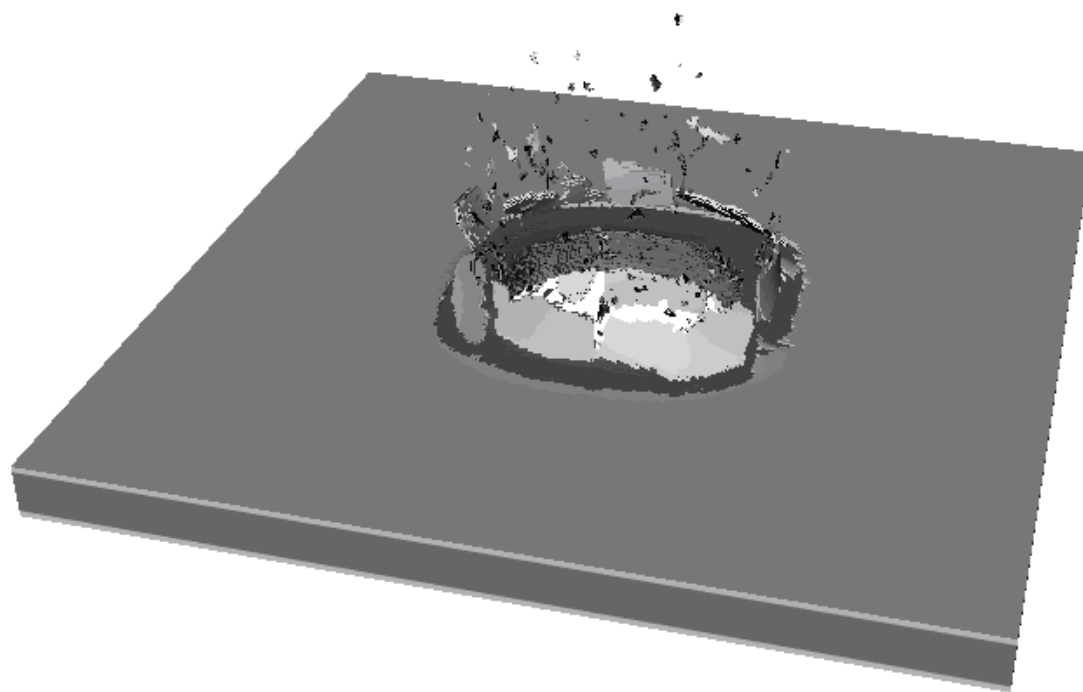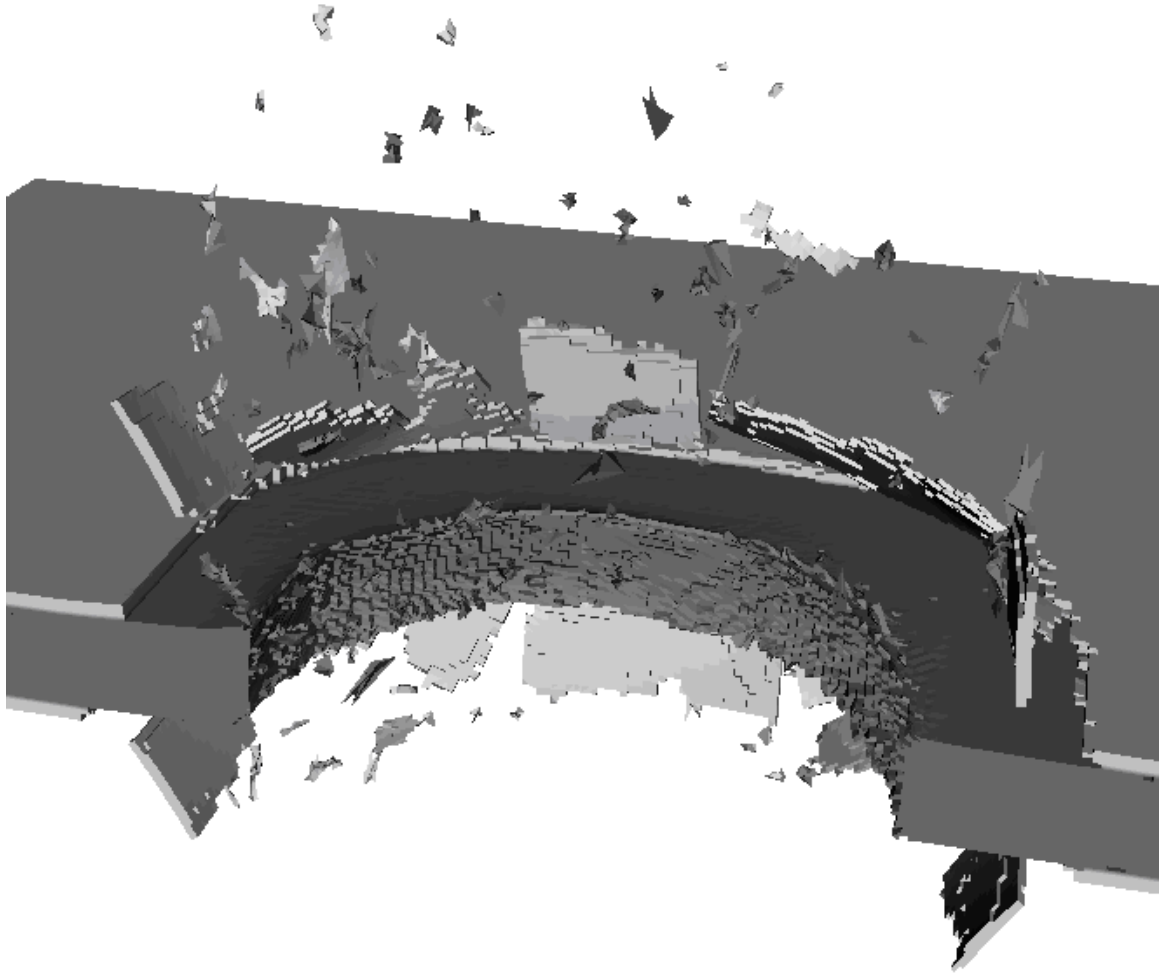
Figure 4.3: Element plot, disc impact simulation.

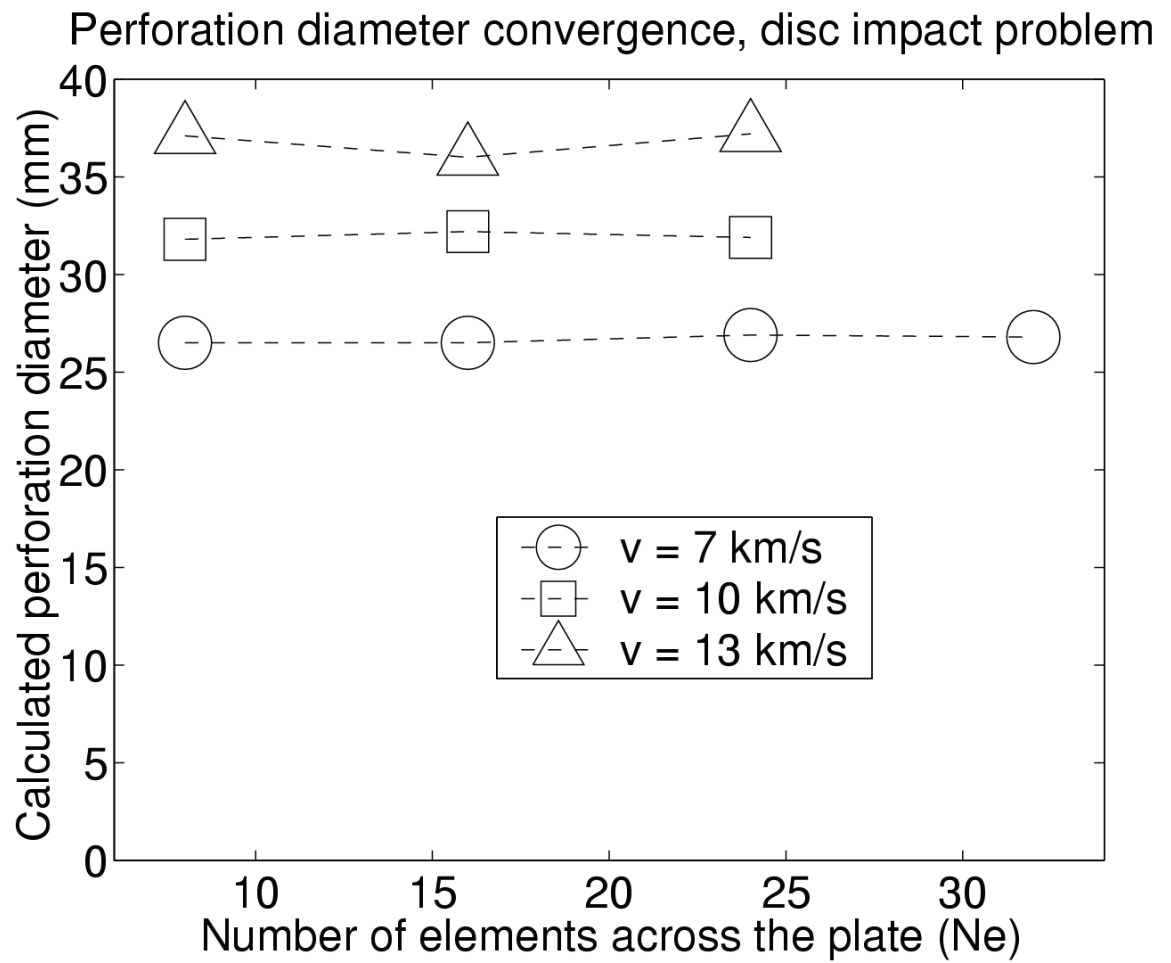Figure 4.4: Sectioned element plot, disc impact simulation.

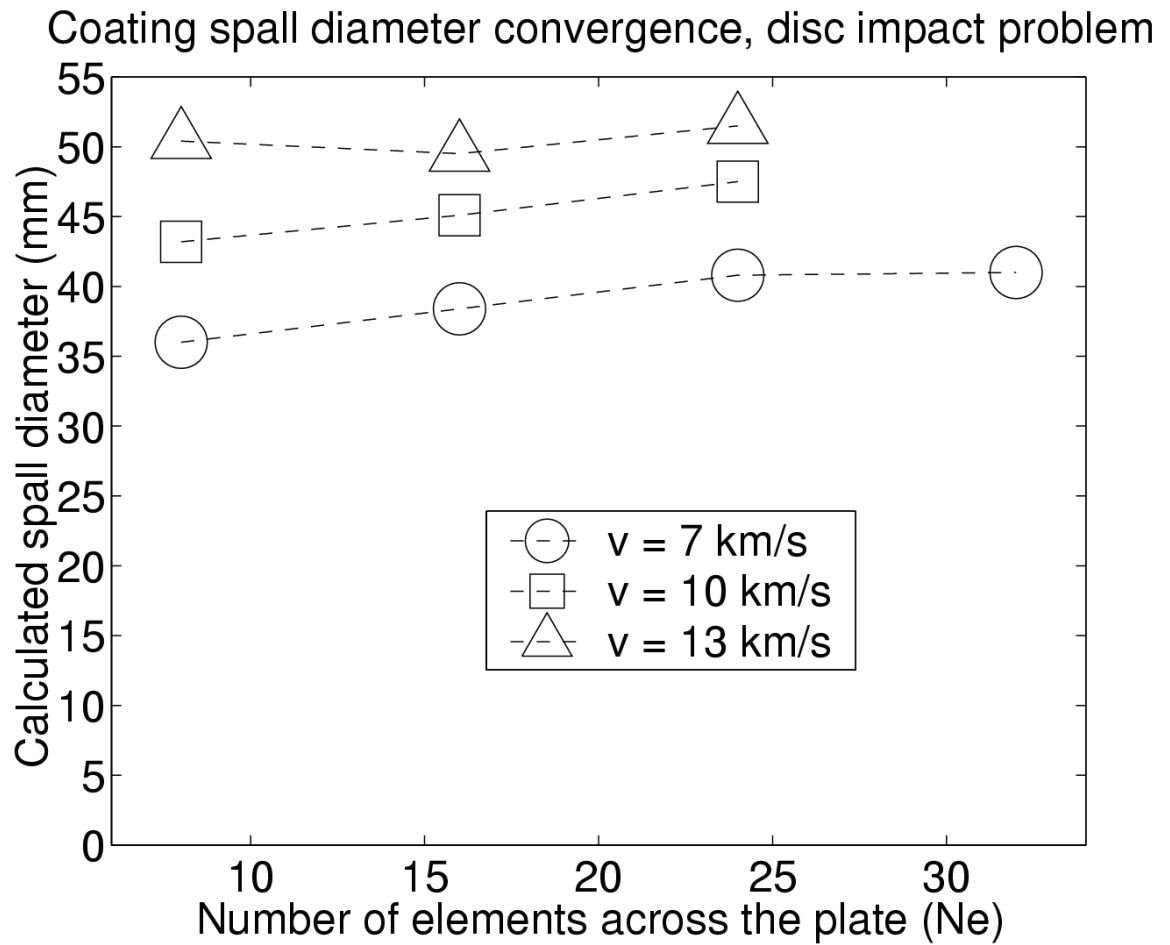Figure 4.5: Convergence data for perforation diameter.

Figure 4.6: Convergence data for coating spall diameter.
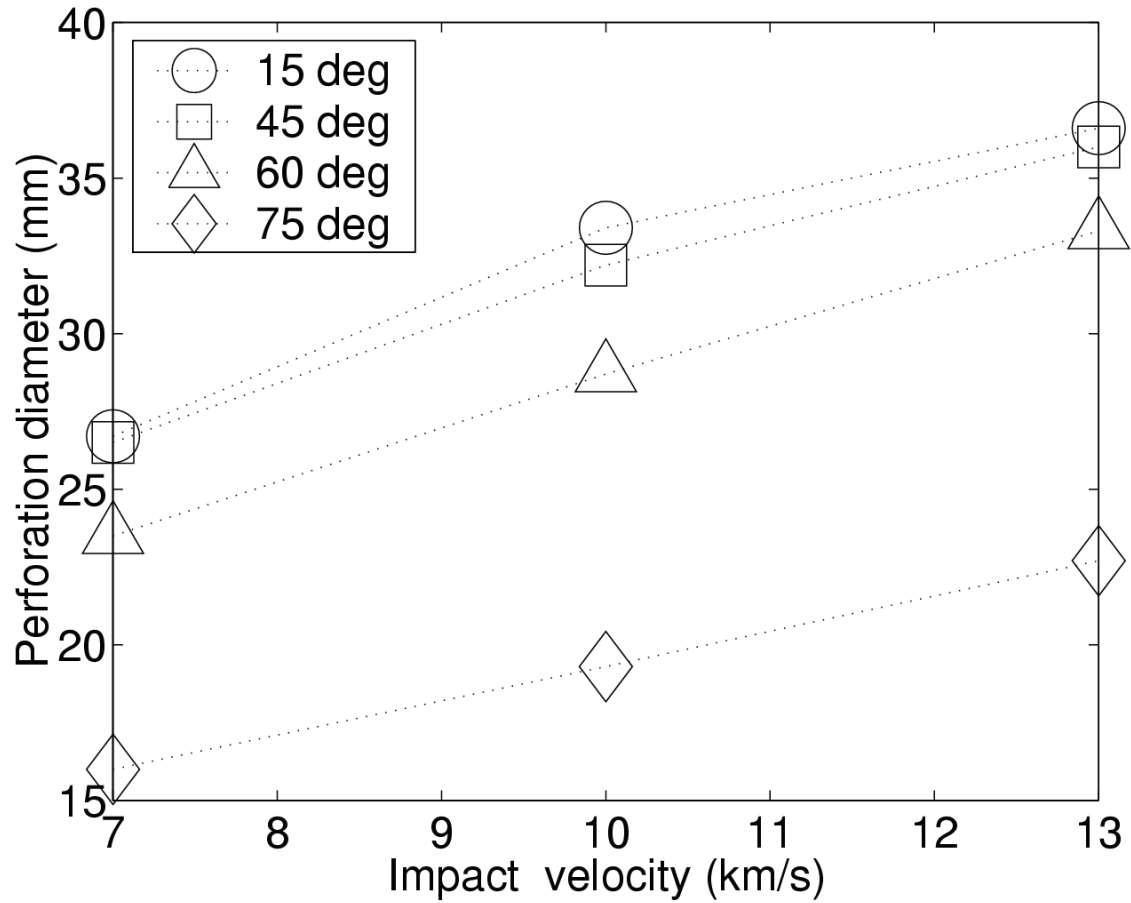
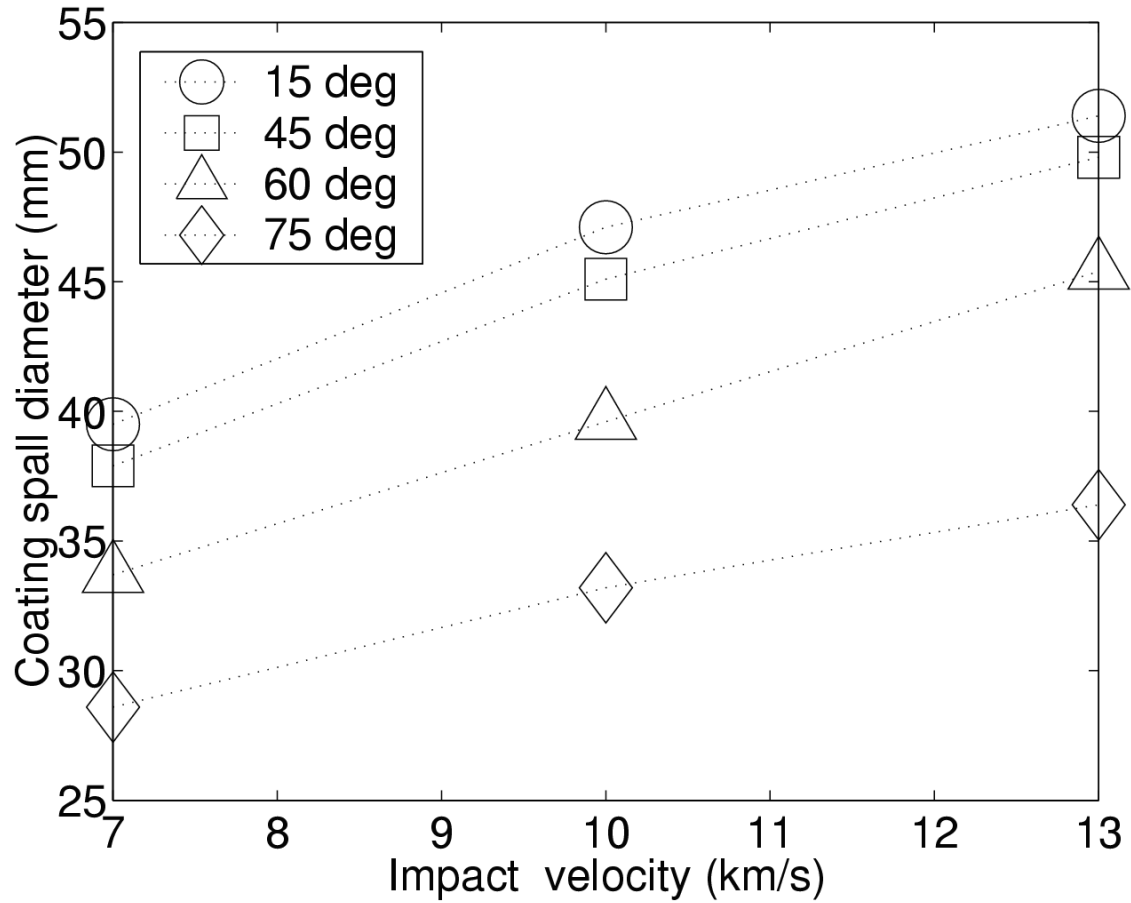Figure 4.7: Perforation diameter data, disc impact cases.

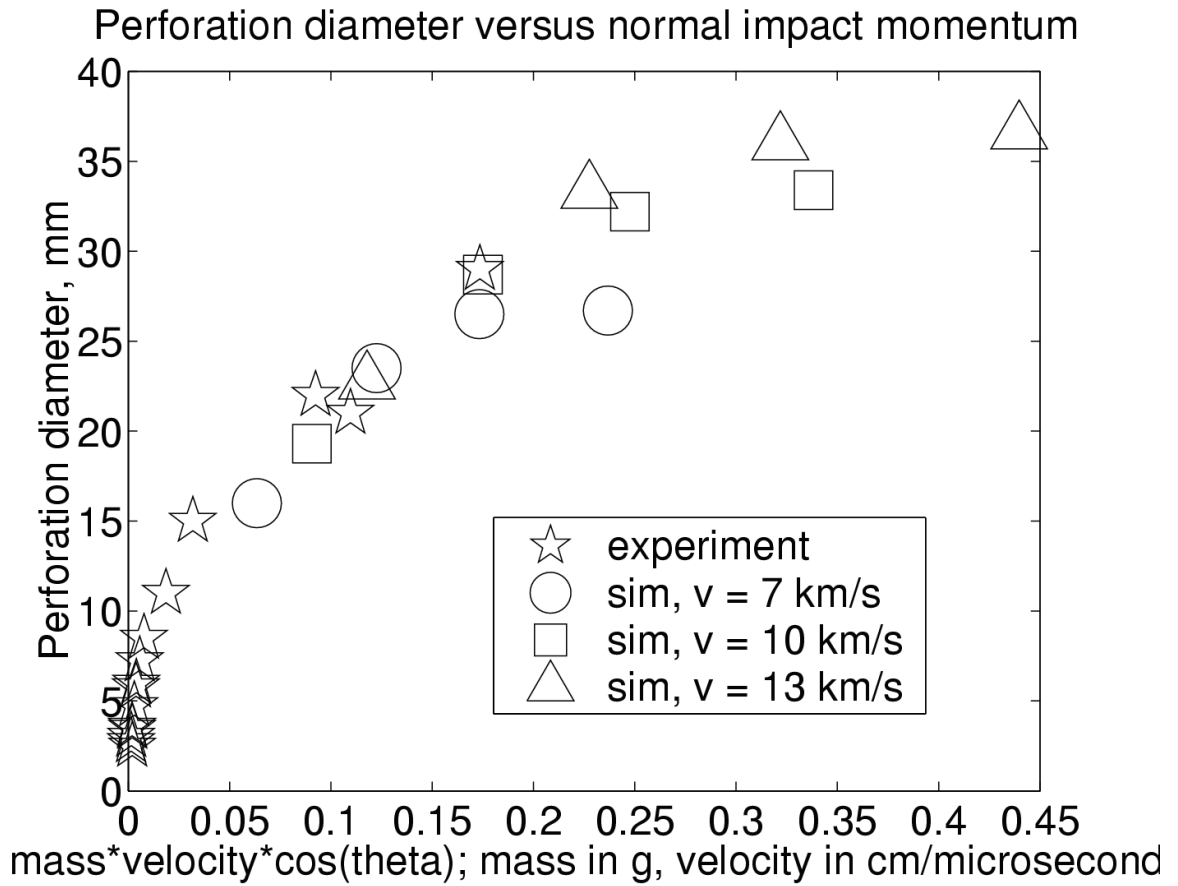Figure 4.8: Coating spall diameter data, disc impact cases.

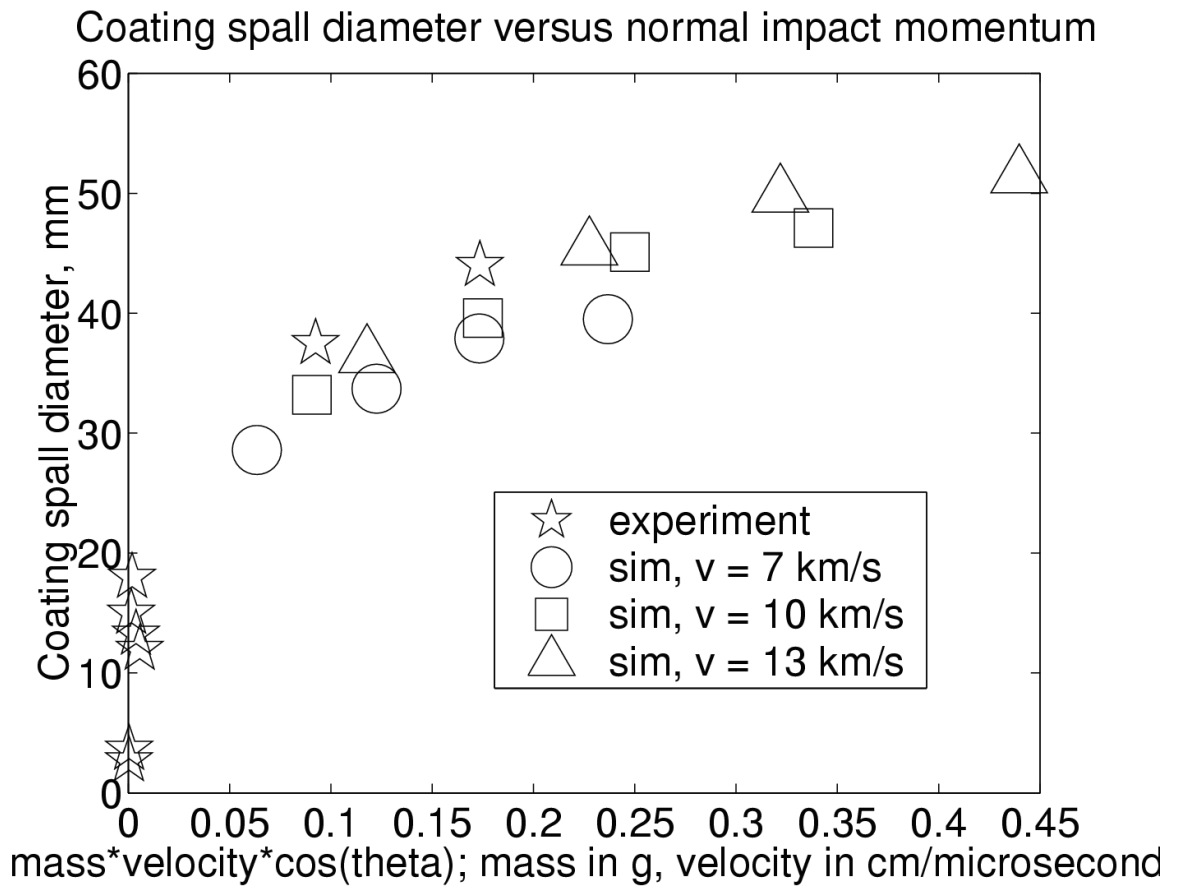Figure 4.9: Perforation diameter versus impact momentum.

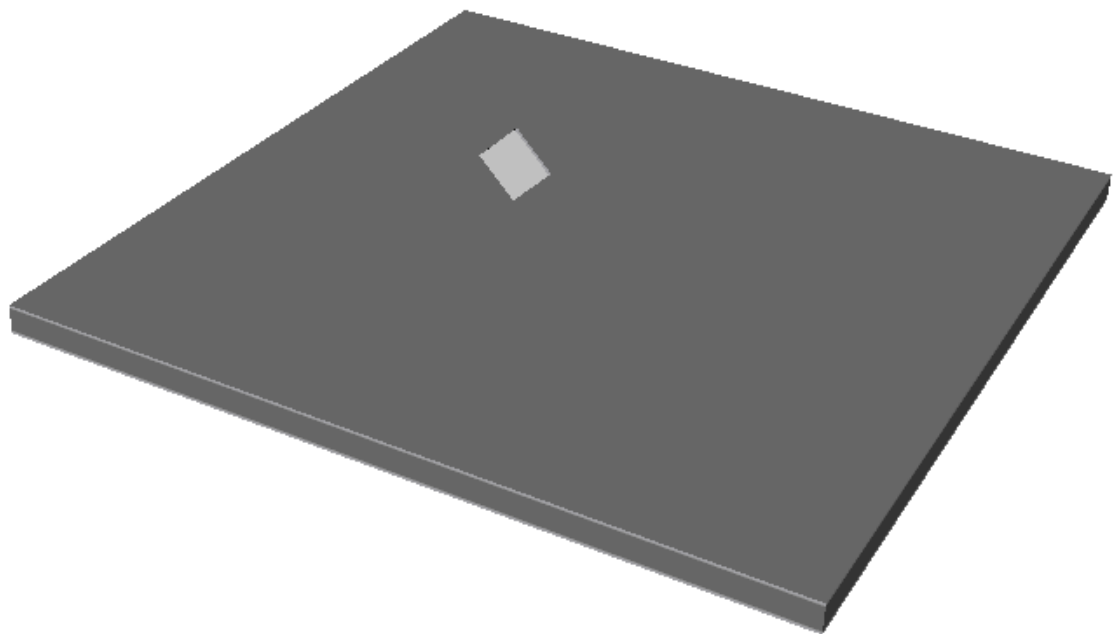Figure 4.10: Coating spall diameter versus impact momentum.

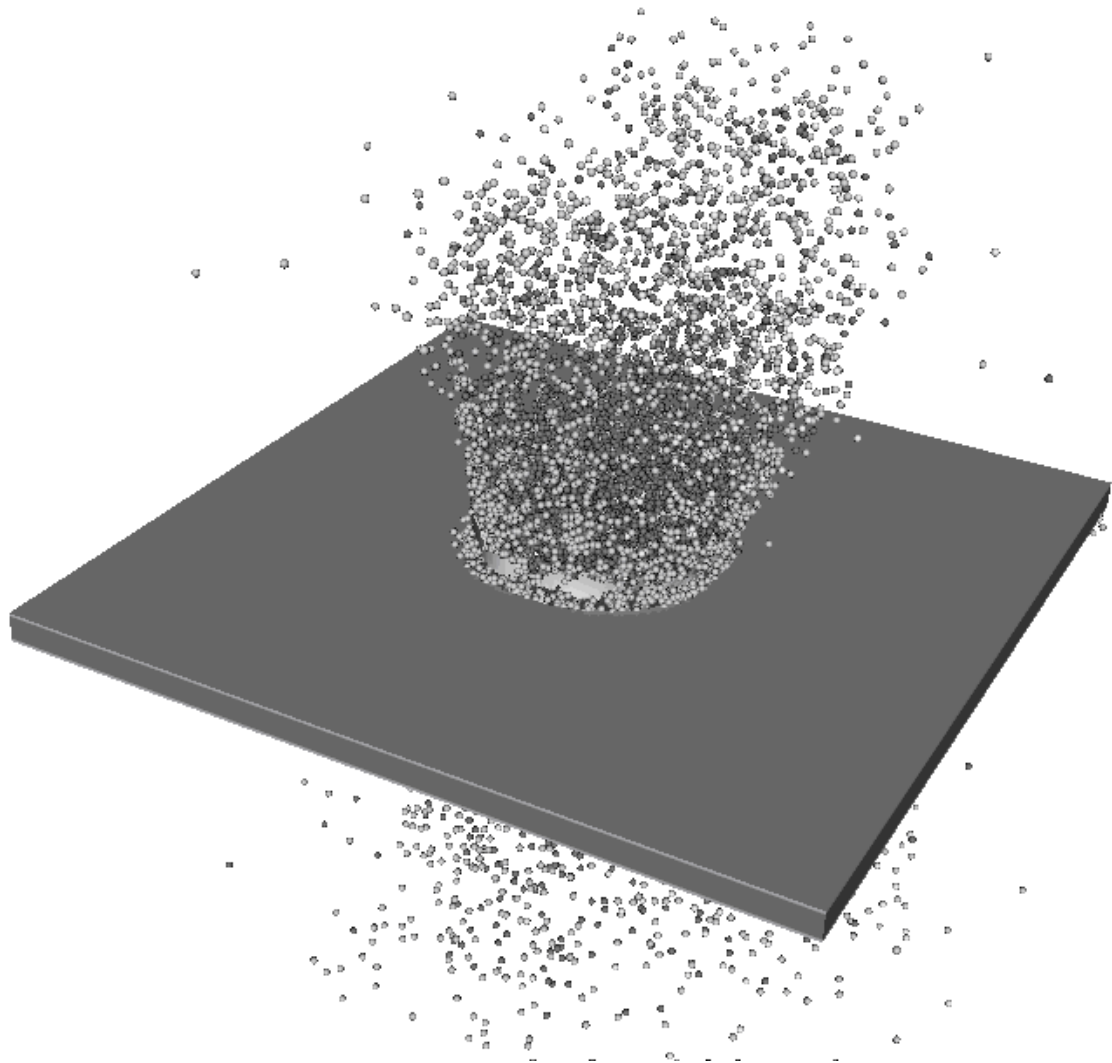Figure 4.11: Initial configuration, plate impact simulation.

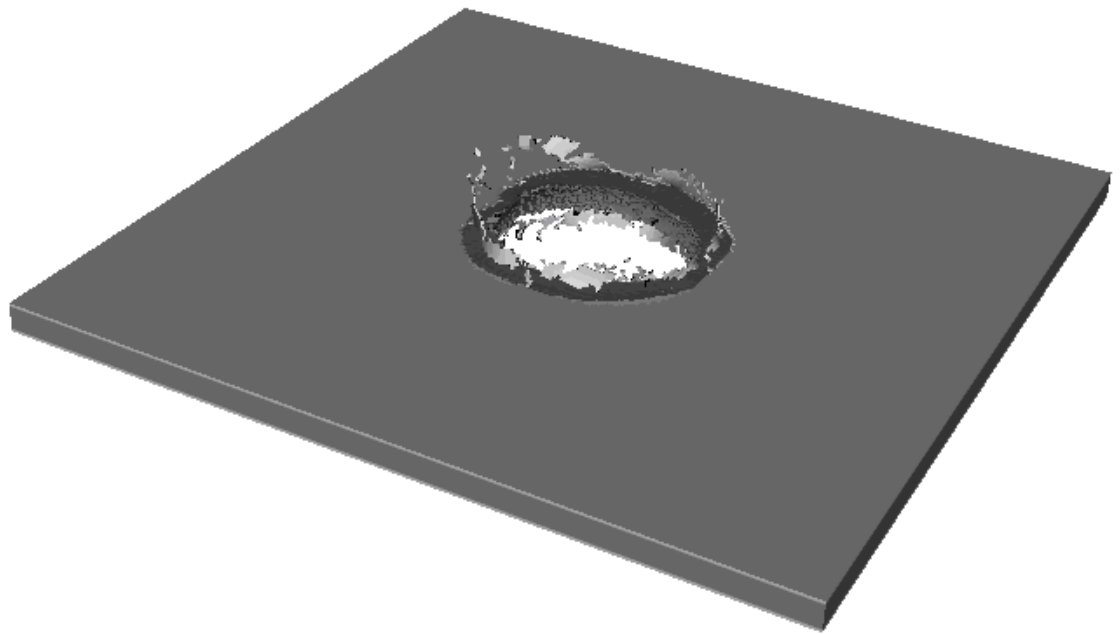Figure 4.12: Plate impact simulation at 50 microseconds.

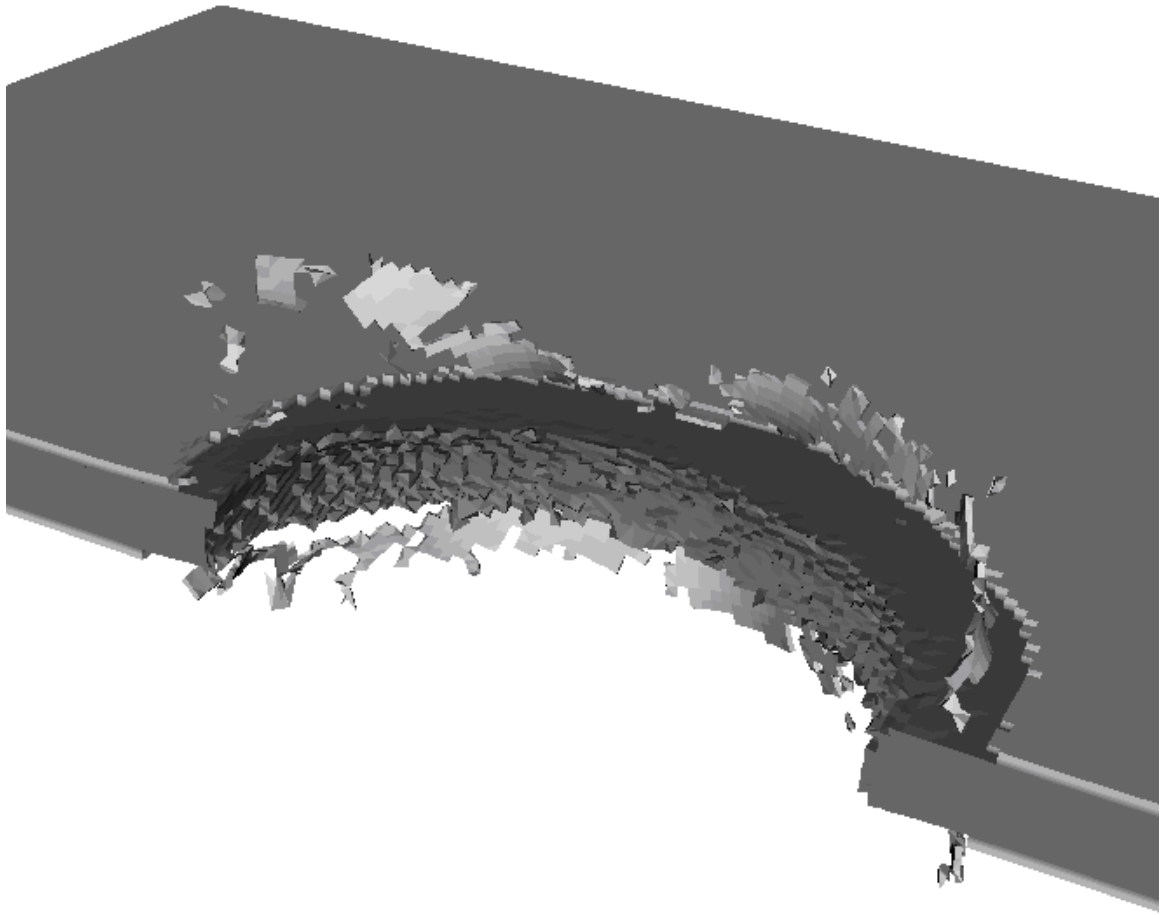Figure 4.13: Element plot, plate impact simulation.

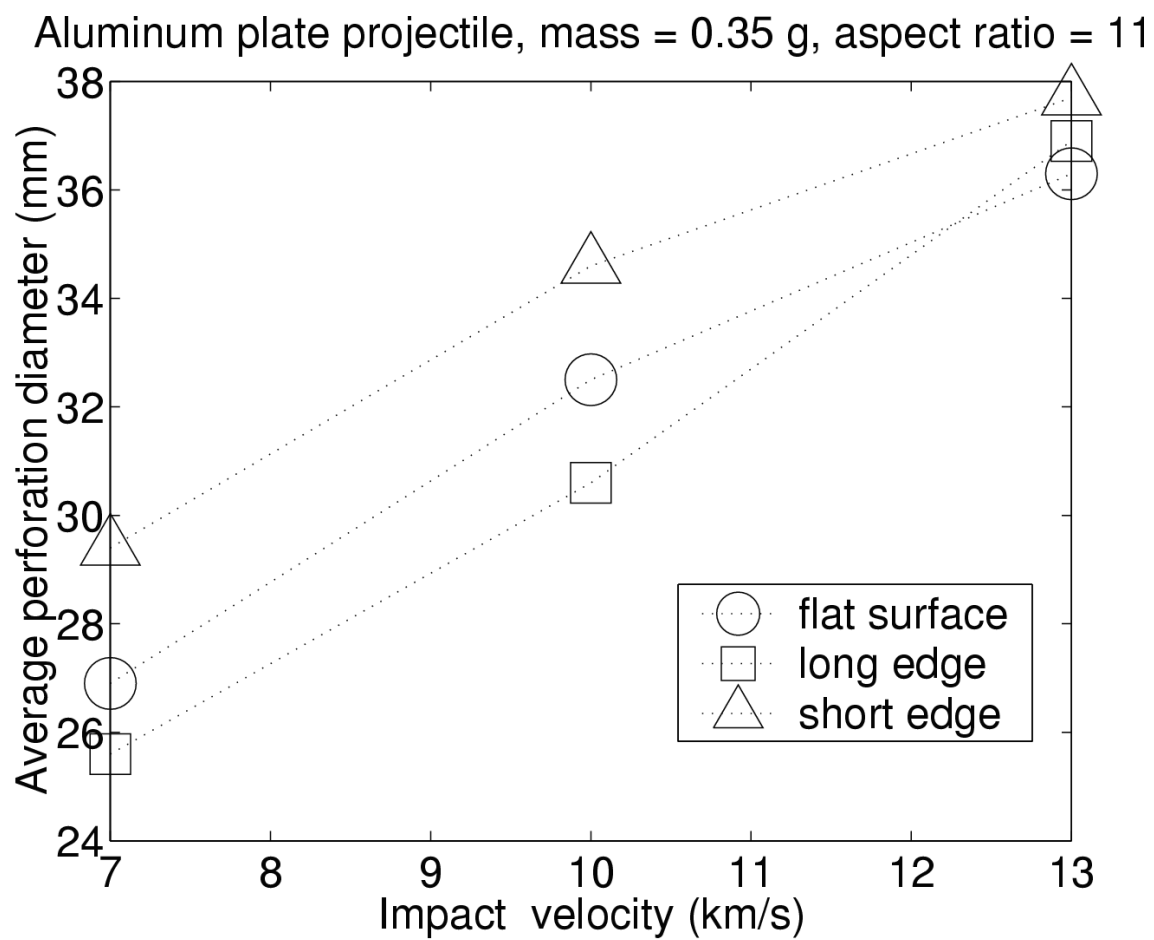Figure 4.14: Sectioned element plot, plate impact simulation.

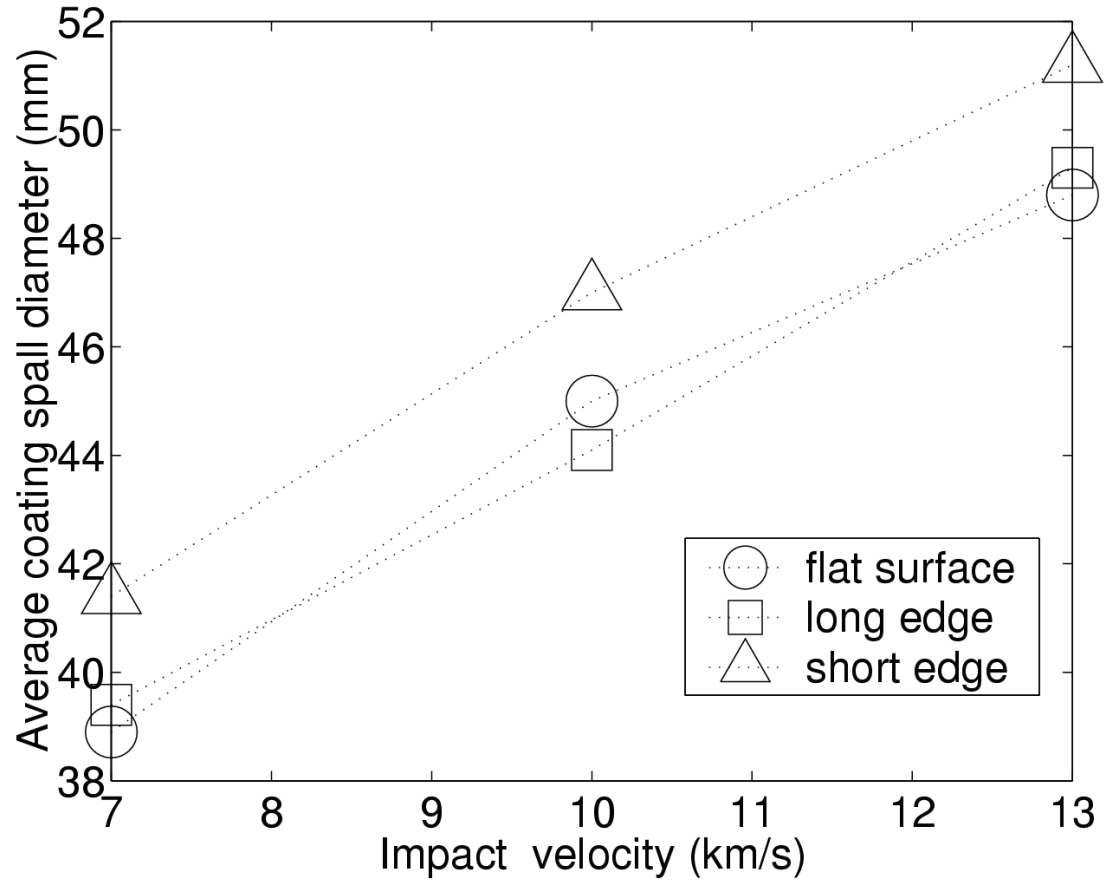Figure 4.15: Perforation diameter data, plate impact cases.

Figure 4.16: Coating spall diameter data, plate impact cases.

Chapter 5

Conclusions

This chapter summarizes the work performed in this research, and provides recommendations for future work.

This dissertation extends the hybrid particle-finite element method described in previous work, allowing for problems incorporating more complex geometries, described by a general hexahedral mesh. In order to generate the particle-element model a translation algorithm was developed. The model introduces particles only at the element vertices, in order to gain computational efficiency. The translation algorithm takes mesh information from commercial software as an input and computes the masses, aspect ratios, and orientations of the particles in the particle-element model.

A new density interpolation was developed for use with a general hexahedral mesh. Normalization of the particle separation distances is performed, by taking into account the separation distance in the reference configuration. In addition, a full neighbor set for each particle is defined by a computation in the reference configuration.

To obtain the ODE system for the particle-element model, the system stored energy functions are combined with constraint equations to obtain

thermomechanical Lagrange equations. The formulation shows good results in several validation simulations.

The improved hybrid numerical method developed in this work will make possible simulations of impacts on more complex structures, as illustrated by the generic model of spacecraft structures depicted in Figures 5.1 through 5.8. These figures depict projectile and target models broadly representative of spacecraft structures. The target is a cylindrical body (green) with an internal tank (red), whereas the projectile is a cylinder with a thick end cap (blue). The graphics in Figures 5.9 and 5.10 depict an impact sequence, at a velocity of 3.5 km/s, performed over a period of 100 microseconds. As the sequence illustrates, the modeled breakup includes large fragments, such as the back end of the target and sphere, as well as numerous small fragments (individual particles) ejected at or near the point of collision. In future work it is suggested that geometrically complex impact problems of this type be simulated and compared with experimental results.
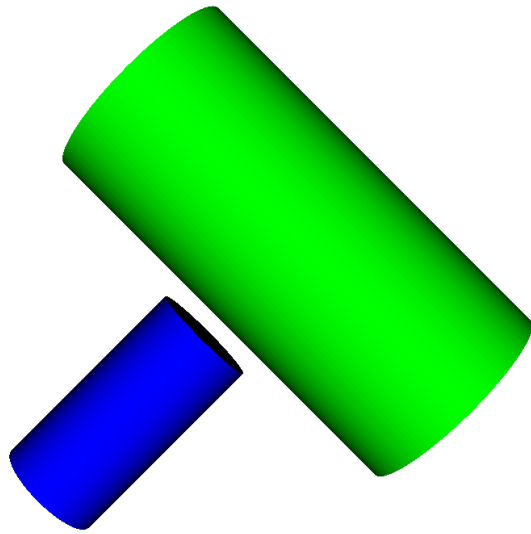
Figure 5.1: Generic model for spacecraft structures, element plot of the initial configuration.
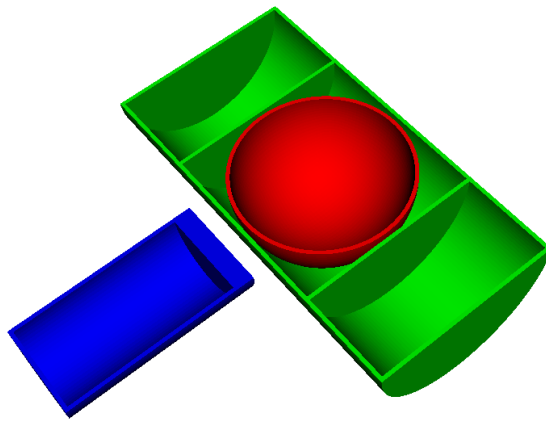
Figure 5.2: Generic model for spacecraft structures, sectioned element plot.

106

Figure 5.3: Generic model for spacecraft structures, projectile mesh.

Figure 5.4: Generic model for spacecraft structures, sectioned projectile mesh.

Figure 5.5: Generic model for spacecraft structures, target mesh (cylinder).

Figure 5.6: Generic model for spacecfraft structures, sectioned target mesh (cylinder).

Figure 5.7: Generic model for spacecraft structures, target mesh (sphere).

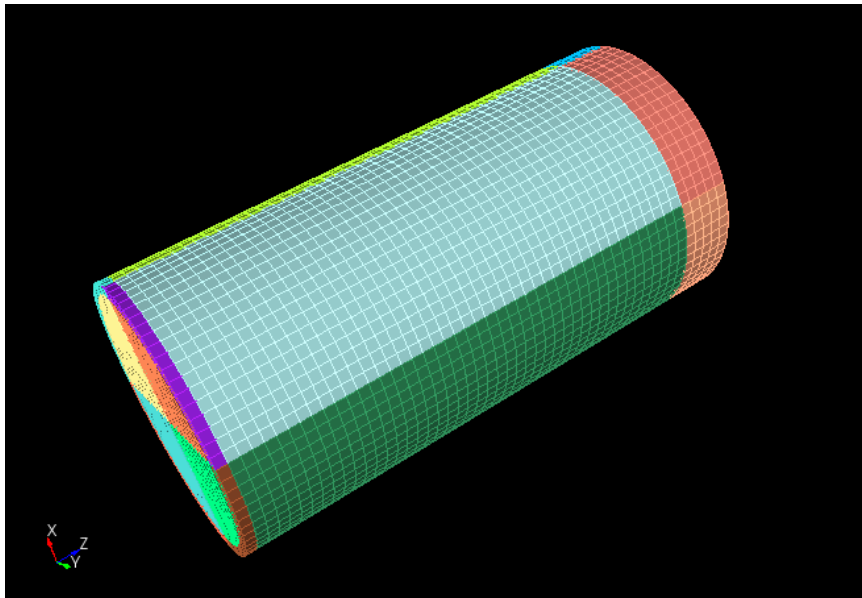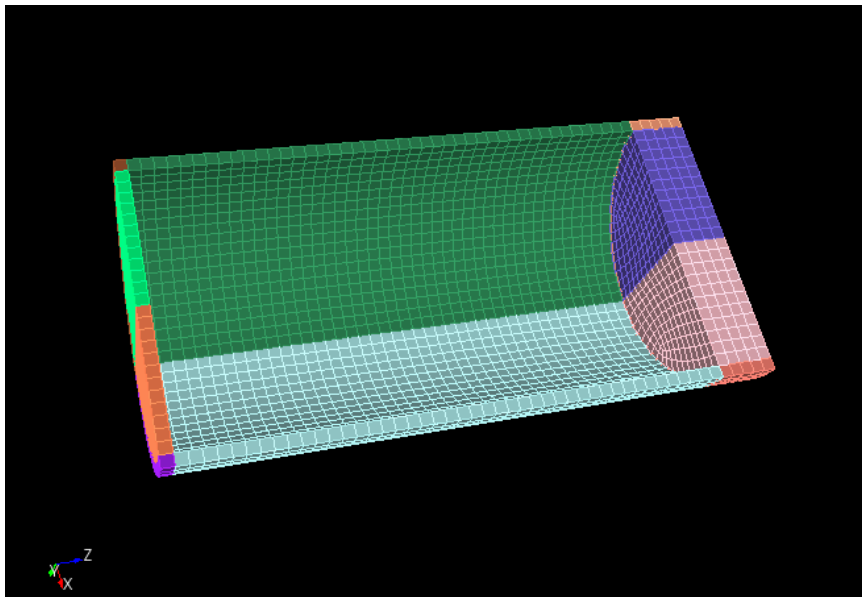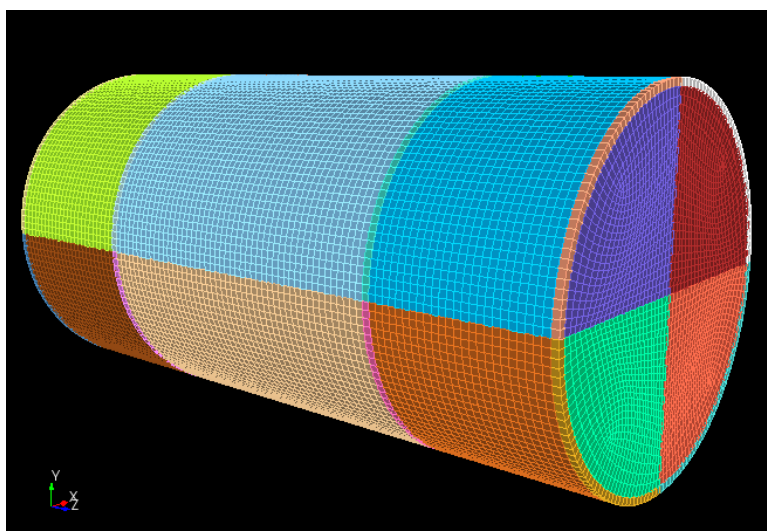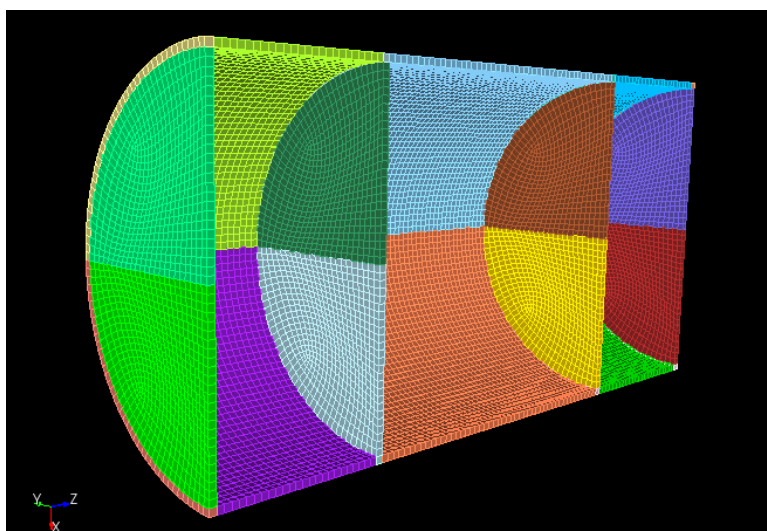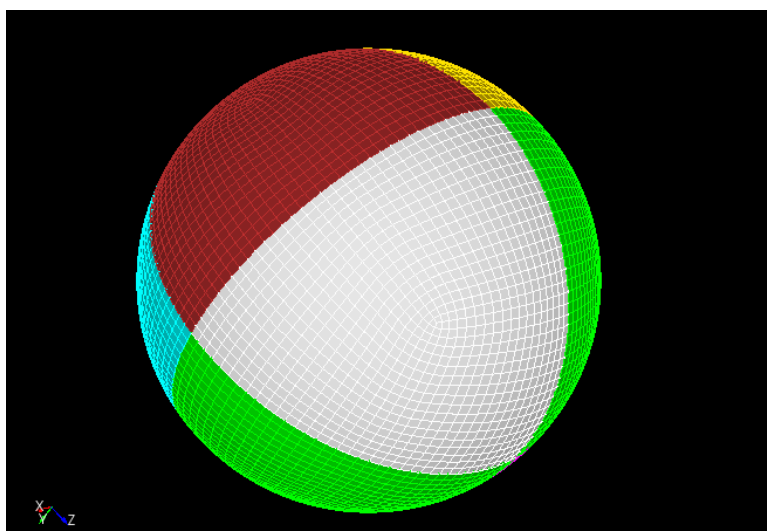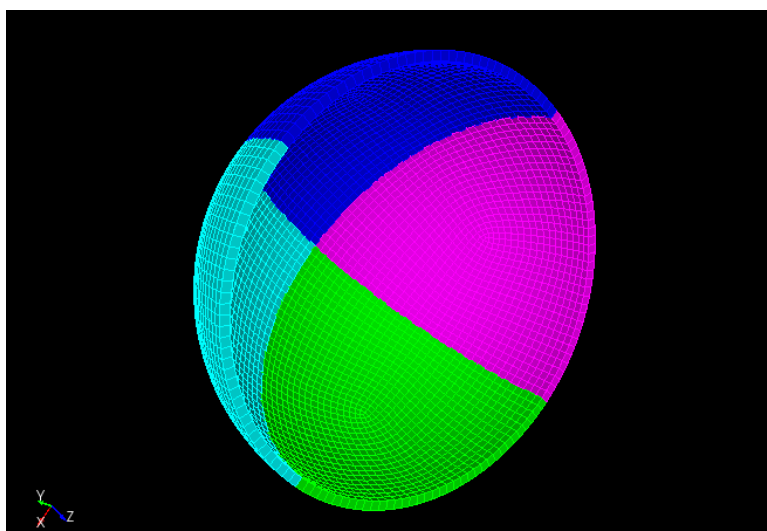Figure 5.8: Generic model for spacecraft structures, sectioned target mesh (sphere).
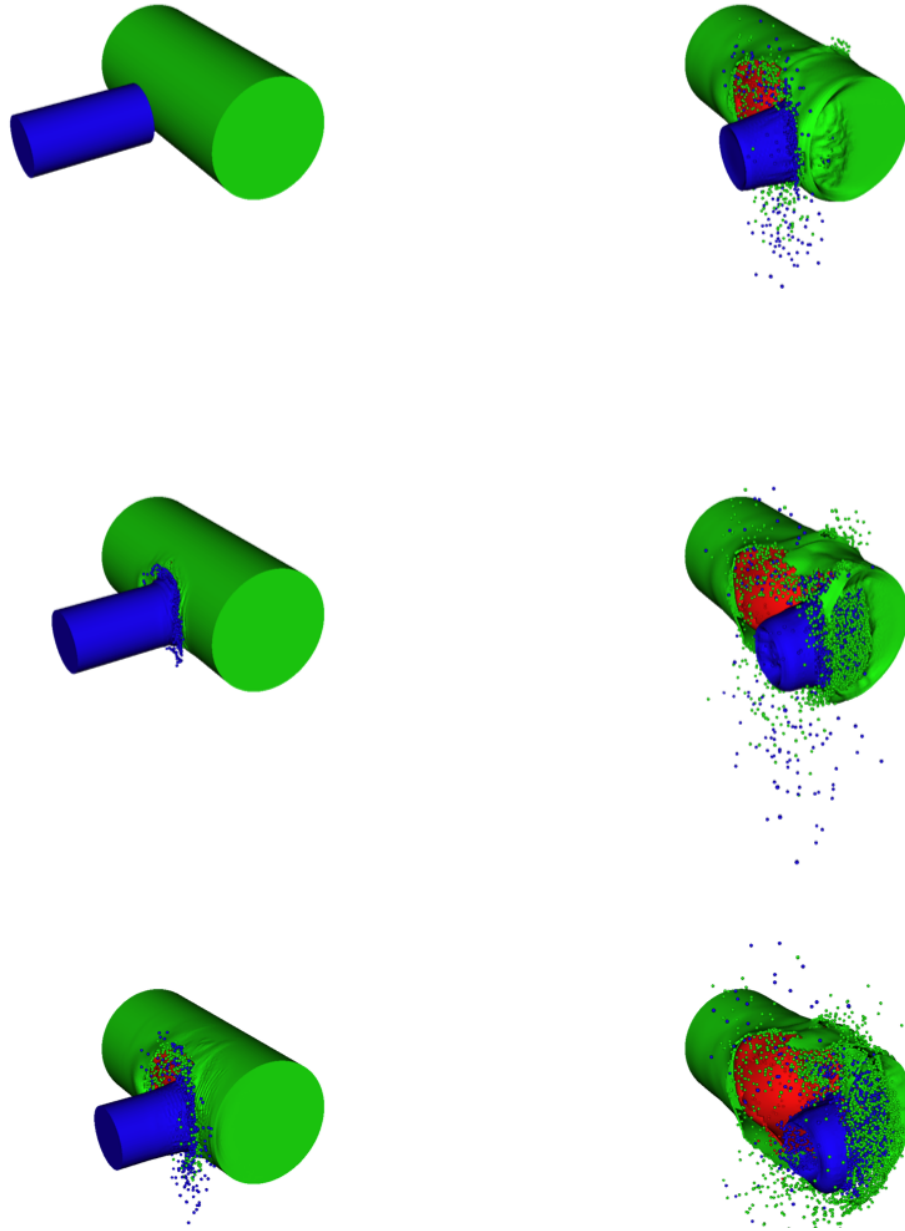
Figure 5.9: Generic model for spacecraft structures, initial impact sequence.
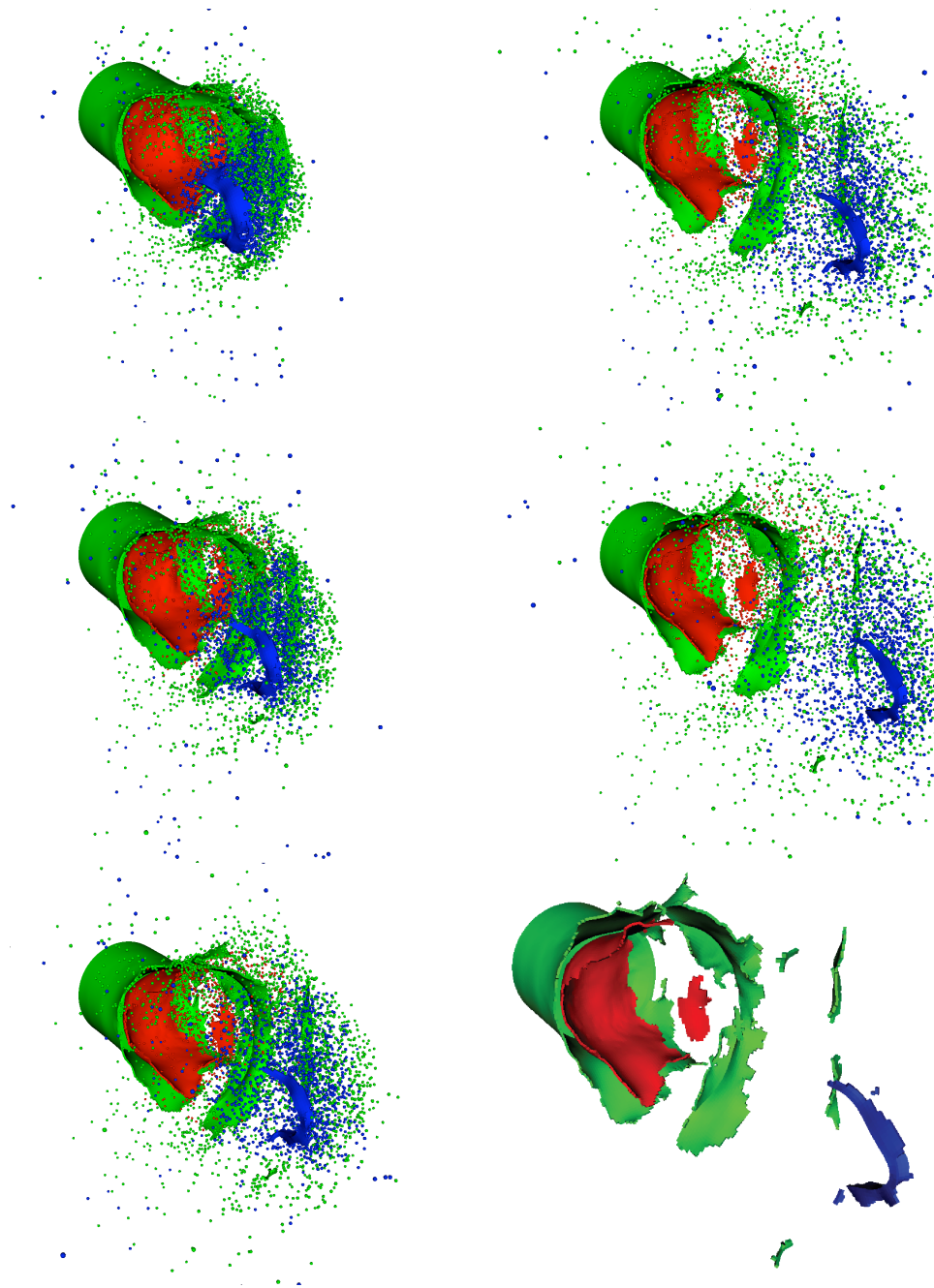
Figure 5.10: Generic model for spacecraft structures, final impact sequence.

Bibliography

[1] C.E. Anderson, P.A. Cox, G.R. Johnson, P.J. Maudlin. A constitutive formulation for anisotropic materials suitable for wave propagation computer programs - II. *Computational Mechanics*, **15**: 201-223, 1994.

[2] H. Baruh.*Analytical Dynamics*, McGraw Hill, New York, 1999.

[3] K.J. Bathe. *Finite Element Procedures*, Prentice Hall, Englewood Cliffs, New Jersey, 1996.

[4] E.E. Becker, G.F. Carey, J.T. Oden. *Finite elements: An introduction*, Prentice Hall, Englewood Cliffs, New Jersey, 1983.

[5] S.R. Beissel, C.A. Gerlach, G.R. Johnson. A quantitative analysis of computed hypervelocity debris clouds. *International Journal of Impact Engineering*, **35**: 1410-1418, 2008.

[6] T. Belytschko, Y. Krongauz, D. Organ, M. Fleming, P. Krysl. Meshless methods: An overview and recent developments. *Computer Methods in Applied Mechanics and Engineering*, **139**: 3-47, 1996.

[7] D.J. Benson. Computational methods in Lagrangian and Eulerian hydrocodes. *Computer Methods in Applied Mechanics and Engineering*, **99**: 235-394, 1992.

[8] R.M. Bowen. *Introduction to Continuum Mechanics for Engineers*, Plenum Press, New York, 1989.

[9] J.D. Buckley and D.D. Edie. *Carbon-carbon materials and composites*, Noyes Publications, New Jersey, 1993.

[10] R.R. Burt and E.L. Christiansen. *International Journal of Impact Engineering*, **29**: 153-166, 2003.

[11] R. Chandra, L. Dagum, D. Kohr, D. Maydan, J. McDonald, R. Menon. *Parallel Programming in OpenMP*, Academic Press, London, 2001.

[12] L.C. Chhabildas, L.N. Kmetyk, W.D. Reinhart, C.A. Hall. Enhanced hypervelocity launcher - capabilities to 16 km/s. *International Journal of Impact Engineering*, **17**: 183-194, 1995.

[13] E.L. Christiansen and L. Friesen. Penetration equations for thermal protection materials. *International Journal of Impact Engineering*, **20**: 153-164, 1997.

[14] E.L. Christiansen and J.H. Kerr. Projectile shape effects on shielding performance at 7 km/s and 11km/s. *International Journal of Impact Engineering*, **20**: 165-172, 1997.

[15] D.M. Curry, V.T. Pham, I. Norman, D.C. Chao. Oxidation of reinforced carbon-carbon subjected to hypervelocity impact. NASA/TP-2000-209760, NASA Johnson Space Center, March 2000.

[16] R. Destefanis and M. Faraud. Testing of advanced materials for high resistance debris shielding. *International Journal of Impact Engineering*, **20**: 209-222, 1997.

[17] C.T. Dyka and R.P. Ingel. An approach for tension instability in smoothed particle hydrodynamics. *Computers and Structures*, **57**: 573-580, 1995.

[18] E.P. Fahrenthold. USER'S GUIDE FOR EXOS, University of Texas, Austin, 2008.

[19] E.P. Fahrenthold. Oblique hypervelocity impact simulations for Whipple shield-protected structures. *International Journal of Impact Engineering*, **17**: 291-302, 1995.

[20] E.P. Fahrenthold and R.J. Hernandez. Simulation of orbital debris impact on the Space Shuttle wing leading edge. *International Journal of Impact Engineering*, **33**: 231-243, 2006.

[21] E.P. Fahrenthold and B.A. Horban. Thermodynamics of continuum damage and fragmentation models for hypervelocity impact. *International Journal of Impact Engineering*, **20**: 241-252, 1997.

[22] E.P. Fahrenthold and J.C. Koo. Energy based particle hydrodynamics for hypervelocity impact simulation. *International Journal of Impact Engineering*, **20**: 253-264, 1997.

[23] E.P. Fahrenthold and R. Shivarama. Extension and validation of a hybrid particle-element method for hypervelocity impact simulation. *International Journal of Impact Engineering*, **29**: 237-246, 2003.

[24] E.P. Fahrenthold and C.H. Yew. Hydrocode simulation of hypervelocity impact fragmentation. *International Journal of Impact Engineering*, **17**: 303-310, 1995.

[25] J.H. Ginsberg. *Advanced Engineering Dynamics*, Harper & Row, 1988.

[26] D.E. Grady and N.A. Winfree. Impact fragmentation of high-velocity compact projectiles on thin plates: a physical and statistical characterization of fragment debris. *International Journal of Impact Engineering*, **26**: 249-262, 2001.

[27] D.T. Greeenwood. *Principles of Dynamics*, Prentice Hall, Englewood Cliffs, New Jersey, 1988.

[28] J.O. Hallquist. THEORETICAL MANUAL FOR DYNA3D, Lawrence Livermore National Laboratory, Livermore, California, 1983.

[29] C.J. Hayhurst, I.H.G. Livingstone, R.A. Clegg, R. Destefanis, M. Faraud. Ballistic limit evaluation of advanced shielding using numerical simulations. *International Journal of Impact Engineering*, **26**:309-320, 2001.

[30] E.S. Hertel. A comparison of the CTH hydrodynamics code with experimental data. Technical Report, Sandia National Laboratories, SAND92-1879, 1992.

[31] R. Hill. *The mathematical theory of plasticity*, Oxford, 1956.

[32] S.A. Hill. Determination of an empirical model for the prediction of penetration hole diameter in thin plates from hypervelocity impact. *International Journal of Impact Engineering*, **30**:303-321, 2004.

[33] B.A. Horban and E.P. Fahrenthold. Hamilton's equations for impact simulations with perforation and fragmentation. *Journal of Dynamic Systems, Measurement, and Control*, **127**: 617-622, 2005.

[34] T.J.R. Hughes. *The Finite Element Method: Linear Static and Dynamic Finite Analysis*, Dover Publishers, New York, 2000.

[35] G.R. Johnson, E.H. Petersen, R.A. Stryk. Incorporation of an SPH option into the EPIC code for a wide range of high velocity impact computations. *International Journal of Impact Engineering*, **14**: 385-394, 1993.

[36] G.R. Johnson and R.A. Stryk. Conversion of 3D distorted elements into meshless particles during dynamic deformation. *International Journal of Impact Engineering*, **28**: 947-966, 2003.

[37] C.E. Anderson Jr, J.D. Walker, S.J. Bless, T.R. Sharron. On the velocity dependence of the L/D effect for long-rod penetrators. *International Journal of Impact Engineering*, **17**: 13-24, 1995.

[38] P.I. Kattan.*MATLAB Guide to Finite Elements: An Interactive Approach*, Springer, Berlin, New York, 2007.

[39] L. Lyons, E.L. Christiansen, J.H. Kerr. Hypervelocity impact testing of reinforced carbon-carbon composites, Report JSC 23898, NASA Johnson Space Center, 1998.

[40] W.Y. Lu, B.R. Antoun, J.S. Korellis, S. Scheffel, M.Y. Lee, R.D. Hardy, L.S. Costin. Material characterization of shuttle thermal protection system for impact analyses.*AIAA-2004-0945, presented at the 2004 AIAA Aerospace Sciences Meeting*, Reno, Nevada, January 5-8, 2004.

[41] J. Lubliner. *Plasticity theory*, Macmillan, New York, 1990.

[42] E. Madenci and I. Guven.*The Finite Element Method and Applications in Engineering Using Ansys*, Springer, New York, 2006.

[43] L.E. Malvern.*Introduction to the Mechanics of a Continuous Medium*, Prentice Hall, Englewood Cliffs, New Jersey, 1969.

[44] G.T. Mase and G.E. Mase.*Continuum mechanics for engineers*, CRC Press, Boca Raton, Florida, 1999.

[45] J.M. McGlaun, S.L. Thompson, M.G. Elrick. CTH: A three dimensional shock wave physics code. *International Journal of Impact Engineering*, **10**: 351-360, 1990.

[46] Y.V. Milman, S.I. Chugonova, I.V. Goncharova, V.A. Goncharuk, N.A. Yefimov. *International Journal of Impact Engineering*, **33**: 452-462, 2006.

[47] S. Moaveni.*Finite element analysis: theory and applications with Ansys*, Pearson Prentice Hall, Upper Saddle River, New Jersey, 2008.

[48] P.S. Pacheco. *Parallel Programming with MPI*, Morgan Kaufmann Publishers, San Francisco, 1997.

[49] Y.K. Park. Hybrid particle-finite element simulation of large deformation dynamics in composite materials. PhD dissertation, University of Texas at Austin, December, 2004.

[50] Y.K. Park and E.P. Fahrenthold. A kernel-free particle-finite element method for hypervelocity impact simulation. *International Journal for Numerical Methods in Engineering*, **63**: 737-759, 2005.

[51] Y.K. Park and E.P. Fahrenthold. Simulation of hypervelocity impact effects on reinforced carbon-carbon. *AIAA Journal of Spacecraft and Rockets*, **43**: 200-206, 2006.

[52] A.J. Piekutowski. Formation and description of debris clouds produced by hypervelocity impact. NASA CR-4707, 1996.

[53] A.J. Piekutowski. Holes produced in thin aluminum sheets by the hypervelocity impact of aluminum spheres. *International Journal of Impact Engineering*, **35**: 1716-1722, 2008.

[54] A.J. Piekutowski and K.L. Poormon. Impact of thin aluminum sheets with aluminum spheres up to 9 km/s. *International Journal of Impact Engineering*, **10**: 351-360, 1990.

[55] Report of the Columbia Accident Investigation Board, Volume 1, Government Printing Office, Washington, DC, August, 2003.

[56] R. Shivarama and E.P. Fahrenthold. An ellipsoidal particle-finite element method for hypervelocity impact simulation. *International Journal for Numerical Methods in Engineering*, **59**: 737-753, 2004.

[57] W.P. Schonberg. An investigation of oblique hypervelocity impact. NGT-01-008-02, NASA/MSFC, August 1987.

[58] W.P. Schonberg, R.A. Taylor, J.R. Horn. An analysis of penetration and ricochet phenomena in oblique hypervelocity impact. TM-100319, NASA/MSFC, February 1988.

[59] B.R. Sorensen, K.D. Kimsey, B.M. Love. High-velocity impact of low-density projectiles on structural aluminum armor. *International Journal of Impact Engineering*, **35**: 1808-1815, 2008.

[60] D.J. Steinberg. Equation of state and strength properties of selected materials. Technical Report, Lawrence Livermore National Laboratory, UCRL-MA-106439, 1996.

[61] R.F. Stellingwerf and C.A. Wingate. Impact modeling with smooth particle hydrodynamics. *International Journal of Impact Engineering*, **14**: 707-718, 1993.

[62] J.D. Walker, D.J. Grosch, S.A. Mullin. Experimental impacts above 10 km/s. *International Journal of Impact Engineering*, **17**: 903-914, 1995.

[63] H.B. Wilson, L.H. Turcotte, D. Halpern. *Advanced Mathematics and Mechanics Applications Using Matlab*, Chapman & Hall/CRC, Boca Raton, 2003.

[64] Q. Zhang, Y. Chen, F. Huang, R. Long. Experimental study on expansion characteristics of debris clouds produced by oblique hypervelocity impact of LY12 aluminum projectiles with thin LY12 aluminum plates. *International Journal of Impact Engineering*, **35**: 1884-1891, 2008.

[65] J.A. Zukas, T. Nicholas, H. Swift, L.B. Greszczuk, D.R. Curran. *Impact Dynamics*, John Wyley and Sons Ltd., 1982.

Vita

Roque Julio Hernandez was born in Barranquilla, Colombia on 6 May 1972, the son of Roque Hernandez Medina and Nancy Donado de Hernandez. He graduated from Colegio Colon in Barranquilla, Colombia in 1988. He received the Bachelor of Science degree in Mechanical Engineering from the Universidad del Norte in 1994. He worked in a coal mine until 1995 and after that entered the Graduate School of Universidad de los Andes in Bogota, Colombia and earned a Master of Science in Mechanical Engineering in 1998. He Joined the Mechanical Engineering Department of Universidad del Norte and in 2001 he applied to the University of Texas at Austin for enrollment in their Mechanical Engineering Doctoral Program.

Permanent address: Cra 38A No 76-22
Barranquilla, Colombia

This dissertation was typeset with LaTeX[†] by the author.

[†]LaTeX is a document preparation system developed by Leslie Lamport as a special version of Donald Knuth's TeX Program.